THREE-DIMENSIONAL MODELING OF ACID TRANSPORT AND ETCHING IN A FRACTURE

A Dissertation

by

CASSANDRA VONNE OETH

Submitted to the Office of Graduate and Professional Studies of
Texas A&M University
in partial fulfillment of the requirements for the degree of

DOCTOR OF PHILOSOPHY

Chair of Committee,	Alfred Daniel Hill
Committee Members,	Ding Zhu
	Robert Handler
	Eduardo Gildin
Head of Department,	Alfred Daniel Hill

December 2013

Major Subject: Petroleum Engineering

ABSTRACT

Acid fracture stimulation generates higher well production but requires engineering design for treatment optimization. To quantify the cost and benefit of a particular acid fracture treatment an engineer must predict the resulting fracture's conductivity, which is based on the etched width created by the injected acid. Etching occurs along the fracture surface but is based on acid flowing through the fracture, so an evaluation tool should describe three-dimensional physics and chemistry. Current practice is to estimate conductivity utilizing two-dimensional models. Unfortunately, these models necessarily assume how acid is distributed in the fracture and often misrepresent the amount of acid etching upon which the conductivity is based.

A fully three-dimensional modeling tool to evaluate and predict acid fracture performance across the wide range of carbonate field properties has been developed. The model simulates acid transport and fracture face dissolution. The acid transport model includes the solution of the three-dimensional velocity and pressure fields, the non-Newtonian characteristics of most acid fracturing fluids, and diffusion of acid toward the fracture surface. The model numerically solves the equations describing the three-dimensional acid transport and reaction within a fracture to yield the etched width created by acid along the fracture. The conductivity is calculated with the simulator derived acid-etched width, using correlations recently developed that reflect the small scale heterogeneity of carbonate rock as it creates etching along the fracture surface.

The performance of an acid fracture treatment is quantified with conductivity, which is strongly dependent on the etched width created by the acid. This robust new tool more accurately models the impact of design decisions on the acid-etched width and provides a rational path for treatment optimization. Cases typical of industry practice are presented that demonstrate the model capabilities.

DEDICATION

"Throughout history, poverty is the normal condition of man. Advances which permit this norm to be exceeded — here and there, now and then — are the work of an extremely small minority, frequently despised, often condemned, and almost always opposed by all right-thinking people. Whenever this tiny minority is kept from creating, or (as sometimes happens) is driven out of a society, the people then slip back into abject poverty. This is known as 'bad luck.'" - Robert Heinlein

This dissertation is dedicated to that small minority.

ACKNOWLEDGEMENTS

Thank you to my advisers, Dr. Hill and Dr. Zhu, for their patience, encouragement, and technical support of this work. They adopted me into this industry and have provided everything I needed to flourish. My gratitude is also due to Dr. Handler who provided numerous conversations regarding fundamental fluid mechanics, which gave early support of the modeling work. Before even starting on this project, though, Dr. Gildin taught me about numerical methods and I am grateful for his teaching of those skills.

Jianye Mou’s work is to be commended for providing the basis of this research project. His achievements with programming are to be admired and are much appreciated. I acknowledge Mehrnoosh Saneifar for constructing variograms to aid in the geostatistical analysis of the case study well. A general thanks to my other colleagues in the research group and department overall is extended for assistance on this project.

I also want to extend my gratitude to the Acid Fracture Joint Industry Project and Crisman Institute for consistent financial support of this work.

Lastly and most importantly, thank you to my loyal, funny, and wise husband, Larry Oeth, for keeping my spirits high despite my doubts.

NOMENCLATURE

A	Elemental area
A_C	Fracture local cross-sectional area
b	Fracture width
C	Acid concentration
C_B	Acid boundary concentration
C_{eqm}	Acid equilibrium concentration, accounting for reverse reaction
C_i	Acid injection or maximum concentration
$\overline{C}$	Average acid concentration
D_{eff}	Effective acid diffusion
d_{ij}	Rate of strain tensor
E	Young's modulus, 10^6 psi or MMpsi
f_i	Body force in the *i*-direction
f_r	Fraction of acid to react before leaking off
H	Fracture height
J	Jacobian, ratio of physical volume to computational volume
k	Reaction rate coefficient
K	Consistency index for power law fluid

K_g	Apparent mass transfer coefficient of acid across fracture width
L	Fracture length
MW_{acid}	Molecular weight of the acid
n	Power law fluid exponent or index
n'	Reaction order
N_{Pe}	Peclet number
N_{Re}	Reynolds number
p	Pressure
PV_{bt}	Pore volumes to wormhole breakthrough
q_{inj}	Injection flow rate to one wing of the fracture
q_L	Leakoff volumetric flow rate
RES	Rock embedment strength, psi
t	Time
$\bar{v}$	Average velocity
v_i, v_j	Velocity components in the *i*- and *j*-direction
v_L	Leakoff velocity at fracture surface
v_x, u	*x*-direction velocity component
v_y, v	*y*-direction velocity component

v_z, w	z-direction velocity component
x	Direction parallel to fracture length
x_i, x_j	i- and j-direction lengths
y	Direction parallel to fracture width
z	Direction parallel to fracture height
w_i	Acid-etched width, in
wk_f	Conductivity, md-ft

β	Gravimetric dissolving power
ξ, η, ζ	Computational dimensions
II_d	Second invariant of the rate of strain tensor
$\lambda_{D,x}$	Dimensionless horizontal correlation length
$\lambda_{D,z}$	Dimensionless vertical correlation length
ϕ	Formation porosity
ρ	Density
σ_c	Closure stress, psi
σ_D	Dimensionless standard deviation of permeability
σ_{ij}	Stress tensor

μ	Viscosity
μ_{app}	Apparent viscosity, power law fluid viscosity
υ	Kinematic viscosity

TABLE OF CONTENTS

Page

LIST OF FIGURES

Page

LIST OF TABLES

CHAPTER I

INTRODUCTION

1.1 Acid Fracture Stimulation and Treatment Design

Acid fracturing is a well stimulation technology for carbonate reservoirs. The first step of an acid fracture treatment is to create a fracture with hydraulic pressure by injecting a nonreactive slug of fluid termed a pad. The pad produces the initial crack geometry, which increases the contact of the well with the reservoir. Acid is injected next to dissolve the rock along the faces of the fracture. A treatment may involve multiple stages of the pad and acid fluids to keep the fracture open while also generating etched width along the fracture. The last of the acid is flushed from the wellbore after a sufficient volume of rock has been removed from the fracture faces. The pressure is released and the fracture is allowed to close by the earth stresses in the formation, but it does not close completely due to the removal of rock at the fracture surface (Fig. 1.1). The removal of this rock creates a conductive void space termed the acid-etched width, which improves the hydraulic connection of the well to the reservoir.

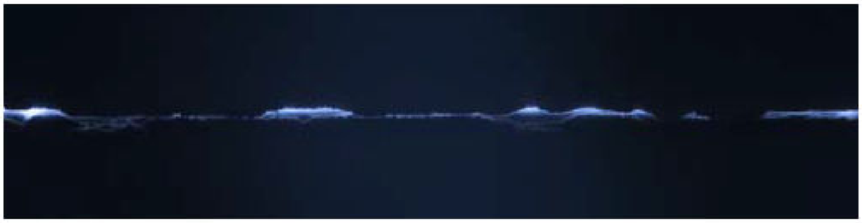

Fig. 1.1—Backlit acid-etched width from a laboratory sample (Kalfayan, 2007).

Efficient use of this technique depends upon predicting the resulting acid fracture conductivity for a particular treatment design. The goal in any fracture treatment is to optimize conductivity, which is a measure of the flow improvement of hydrocarbons to the well. The acid-etched width is the basis for conductivity in an acid fracture treatment. Numerical models of conductivity all depend strongly on the amount of acid-etched width created during an acid fracture treatment (Nierode and Kruk, 1973; Deng et al., 2012).

Some commercial software packages can estimate the ideal acid-etched width and calculate the conductivity. The ideal acid-etched width is the volume of rock dissolved by acid during a treatment divided by the fracture surface area. At best, these software packages utilize two-dimensional (2D) fluid flow solutions. This approach does not utilize gridding perpendicular to the fracture surface and fails to capture numerically the physics behind acid convection and diffusion perpendicular to the fracture plane. Assumptions regarding the acid concentration within the fracture must be made. This can misrepresent the amount of etching that physically occurs.

Researchers have investigated how to quantify the acid fracturing process with an emphasis on resolving the acid concentration profile and etched width (Williams and Nierode, 1972; Roberts and Guin, 1974; Lo and Dean, 1989; Settari, 1993; Romero et al., 2001; Settari et al., 2001). For the transport of acid in the fracture, the velocity profile is typically assumed to follow a known analytical solution (e.g., flow between parallel plates) and only varies in the length direction of the fracture. If the fluid is non-Newtonian, the apparent viscosity is based on the shear rate in one direction. The diffusion that occurs is lumped into an overall mass transfer coefficient that also reflects the transport of acid to the fracture surface by fluid leakoff. The acid concentration in the fracture is resolved into a 2D, semi-analytical profile with assumptions made for transfer in the direction perpendicular to the fracture surfaces.

A model that numerically and rigorously resolves the acid-etched width for a given acid fracture treatment is needed to implement published acid fracture conductivity correlations and improve the design of acid fracture treatments. The basis of a general, portable, three-dimensional (3D) model of acid transport and dissolution in the fracture is presented in this work. The model uses the fracture geometry generated by commercial fracture propagation simulators or analytical models of fracture geometry to define the simulator physical domain. Gridding is fully 3D and includes resolution of the diffusion and convection of acid to the fracture surfaces. The acid fracture simulator yields the amount of dissolution that has occurred in every fracture grid block. With this information and a description of the statistical variations of certain rock properties, the final distribution of created acid fracture conductivity is determined using new conductivity correlations (Deng et al., 2012).

1.2 Literature Overview

Research on the relationships between acid-etched width and acid fracture conductivity is ongoing, but the research to date agrees that there is a strong, power law dependence of conductivity on acid-etched width. Seminal researchers Nierode and Kruk (1973) developed the first widely popular correlation between acid-etched width and conductivity. Their work consisted of breaking in tension core plugs one inch in diameter by 2-3 inches long, flowing acid through the created fracture, and then measuring the conductivity as a function of closure stress for these 25 laboratory samples. They defined an ideal acid-etched width, w_i (*DREC* in their paper), using the measured change in sample mass, the rock density, and the core plug fracture surface area. This, along with the rock embedment strength (*RES*), which is an empirical hardness measure, correlates the fracture closure stress, σ_c, to the conductivity, wk_f. The Nierode-Kruk conductivity correlation is presented in Eqs. 1.1-1.3.

$$wk_f = C_1 \exp\left(-C_2\sigma_c\right) \quad \textbf{(1.1)}$$

$$C_1 = 1.47 \times 10^7 w_i^{2.466} \quad \textbf{(1.2)}$$

$$C_2 = \begin{cases} \left(13.9 - 1.3\ln\left(RES\right)\right) \times 10^{-3} & 0 < RES < 20000 \text{ psi} \\ \left(3.8 - 0.28\ln\left(RES\right)\right) \times 10^{-3} & 20000 \le RES \le 500000 \text{ psi} \end{cases} \quad \textbf{(1.3)}$$

Present day researchers use the same equation form with the only significant differences being in how the coefficients are calculated. The most recently developed acid fracture conductivity correlation uses geostatistical parameters in the C_1 and C_2 coefficients (Deng et al., 2012). The geostatistical parameters include the dimensionless horizontal correlation length ($\lambda_{D,x}$) and dimensionless vertical correlation length ($\lambda_{D,z}$), which are based on oriented permeability datasets and describe how the permeability of the rock is spatially arranged. The last geostatistical parameter, the dimensionless standard deviation of permeability (σ_D), quantifies the width of the permeability distribution in the formation. These geostatistical parameters ($\lambda_{D,x}, \lambda_{D,z}, \sigma_D$) incorporate the small scale mineralogical and petrophysical heterogeneity of the carbonate rock of interest, and one such correlation from this work is presented in Eqs. 1.4-1.6.

$$wk_f = C_1 \exp\left(-C_2 \sigma_c\right) \tag{1.4}$$

$$\begin{aligned} C_1 = 4.48 \times 10^9 &\left[0.1756\left(\operatorname{erf}\left(0.8\sigma_D\right)\right)^3 w_i^{2.49}\right] \times \\ &\left[1 + \left(1.82\operatorname{erf}\left(3.25\left(\lambda_{D,x} - 0.12\right)\right) - 1.31\operatorname{erf}\left(6.71\left(\lambda_{D,z} - 0.03\right)\right)\right)\sqrt{\exp\left(\sigma_D\right) - 1}\right] \times \\ &\left[0.22\left(\lambda_{D,x}\sigma_D\right)^{2.8} + 0.01\left(\left(1 - \lambda_{D,z}\right)\sigma_D\right)^{0.4}\right]^{0.52} \end{aligned} \tag{1.5}$$

$$C_2 = \left[14.9 - 3.78\ln\left(\sigma_D\right) - 6.81\ln\left(E\right)\right] \times 10^{-4} \tag{1.6}$$

The importance of the acid-etched width to the predicted conductivity is demonstrated in these correlations where the conductivity is approximately proportional to $w_i^{2.5}$. It is important therefore that the acid-etched width be accurately determined to understand the conductivity resultant from a particular treatment design.

Calculation of the acid-etched width starts with a known acid concentration profile. The practitioner must understand how acid is distributed throughout the fracture to determine what acid is reaching the surface of the fracture to create etching. Analytical solutions that resolve the steady state acid concentration between infinite parallel plates, where the separation width between the plates is orders of magnitude smaller than the plate length and height, have been developed (Nierode and Williams, 1971; Schechter, 1992). These solutions assume that all flow entering between the plates uniformly leaks out the sides of the flow channel over the entire domain length, utilizing the Berman (1953) velocity profile to resolve the acid concentration. The work by Terrill (1965) solves an almost identical problem but for heat transfer instead of the acid concentration, and the method of determining eigenvalues and eigenfunctions is similarly used in the acid profile solution. The reaction is assumed to be infinite at the fracture surfaces, so the acid concentration is zero there. The solutions for the acid profile and acid-etched width are presented in Figures 1.2 and 1.3.

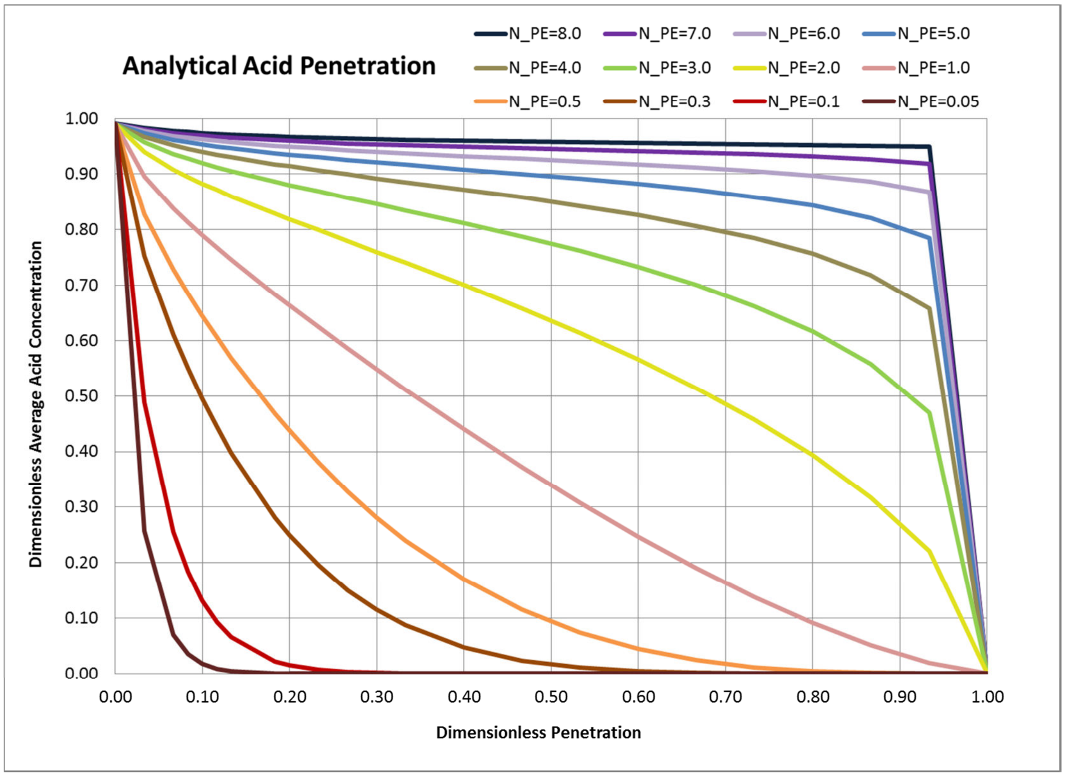

Fig. 1.2—Analytical type curves for the average acid concentration between parallel plates versus domain length (Schechter, 1992).

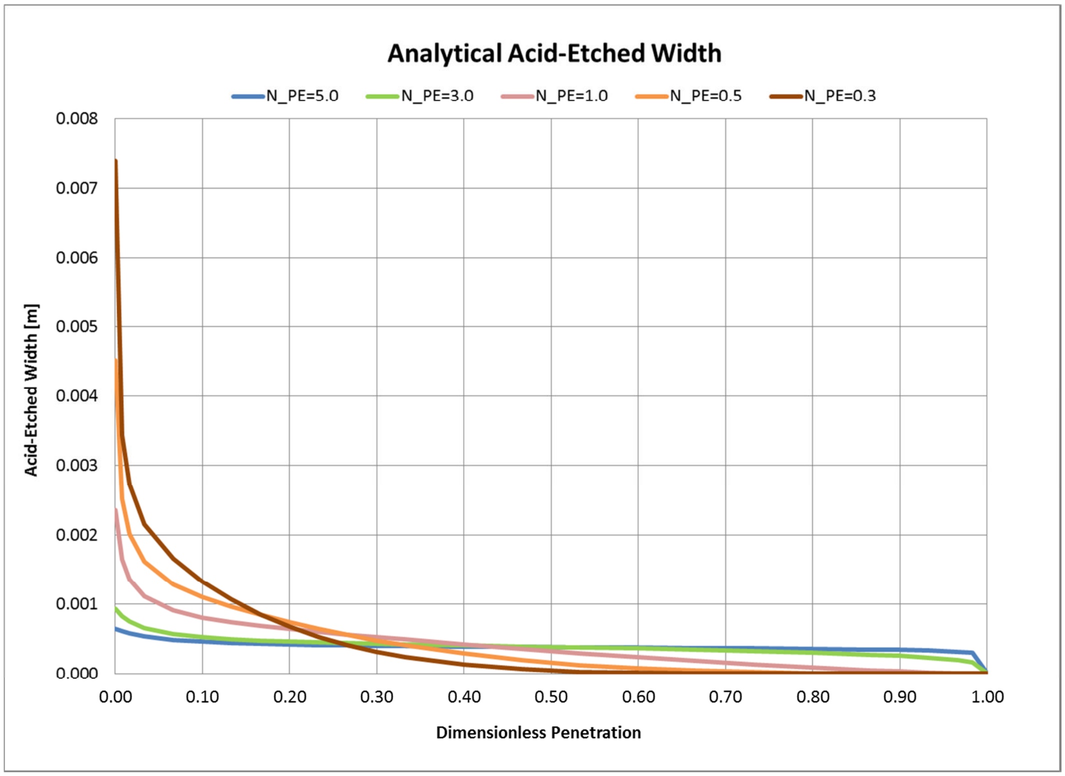

Fig. 1.3—Analytical acid-etched width curves versus length (Schechter, 1992).

Note that these figures use the Peclet number, N_{Pe}, to identify each analytical curve. The Peclet number is defined by Eq. 1.7.

$$N_{Pe} = \frac{\bar{v}_L b}{2D_{eff}} \quad \textbf{(1.7)}$$

Early design practice utilized the analytical solutions to determine the distance that the acid can penetrate the fracture by anticipating the average leakoff velocity, $\bar{v}_L$, fracture width, b, and effective diffusion, D_{eff}, for a particular acid fluid (Williams and Nierode, 1972). The amount of etching required for effective, economic stimulation defines the acid fracture fluid volume to be injected during the treatment.

Two-dimensional finite difference schemes were the next approach for describing the acid concentration profile during an acid fracture treatment. Researchers discretized the following partial differential equation to define the concentration of acid, C, through the fracture (Eq. 1.8).

$$u\frac{\partial C}{\partial x}+v\frac{\partial C}{\partial y}=D_{eff}\frac{\partial^2 C}{\partial y^2} \qquad \textbf{(1.8)}$$

This approach considers convection along the fracture length (*x*-direction velocity, u) with convection and diffusion occurring across the fracture width (*y*-direction velocity, v, and effective diffusion, D_{eff}). Any changes along the fracture height, leakoff variations along the fracture length, transient effects, and non-Newtonian fluid behavior are not included. The model domain is depicted in Figure 1.4.

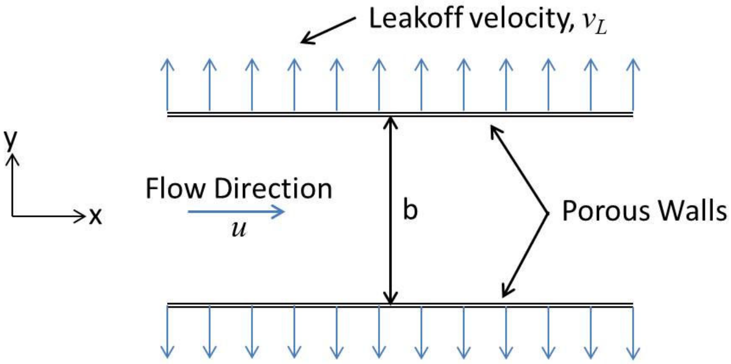

Fig. 1.4—Typical 2D domain envisioned by early acid fracture modelers.

The goal of Roberts and Guin (1974) in using the finite difference method to solve the 2D convection-diffusion equation was to introduce a finite reaction at the fracture surfaces and develop acid penetration type curves as was done by Nierode and Williams (1971) for an infinite reaction rate. These type curves determine the acid penetration for slower reacting mineral/acid systems (i.e., dolomite and weak acids). Roberts and Guin (1974) introduce a reaction balance at the fracture surfaces as shown in Eq. 1.9.

$$-D_{eff}\frac{\partial C}{\partial y}=kC_i^{n'}(1-\phi) \quad \textbf{(1.9)}$$

Similar type curves for acids of different reaction orders, n', and reaction rate coefficients, k, are then developed to predict acid penetration distances and follow the established design procedure.

Other researchers neglect and include terms for the 2D system as they see fit. Lo and Dean (1989) assume an infinite reaction rate at the fracture surfaces but give special attention to the problem of the acid fluid displacing the nonreactive pad fluid for a PKN (Perkins-Kern-Nordgren) geometry fracture, changing the fracture length with respect to time. Settari (1993) creates an acid transport module to be used with his overall fracture simulation software, FRACANAL. The new ACID model includes temperature effects (fracture temperature gradient along length and height, heat of reaction from acid) in the reaction of the acid on the fracture surfaces. The underlying problem with these approaches, however, is that some representative average acid concentration across the fracture width must be assumed even though this is exactly the feature we are trying to resolve. Acknowledging this, Settari et al. (2001) continued 2D work to model rigorously the acid concentration across the fracture width instead of lumping it into some average with an effective mass transfer coefficient (Fig. 1.5).

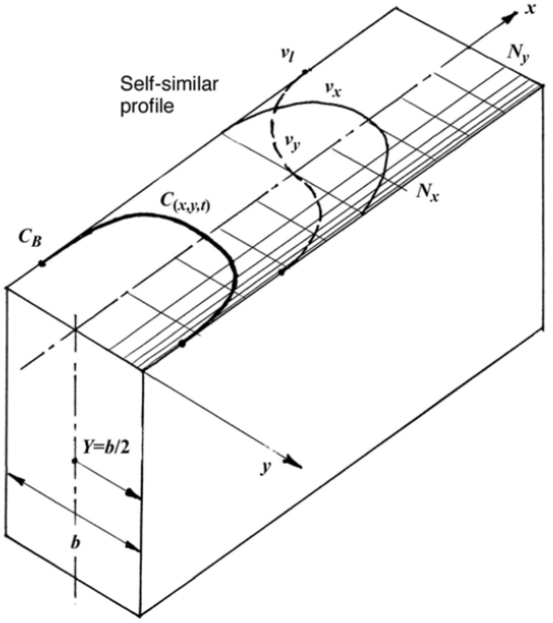

Fig. 1.5—Discretized *x*- and *y*-direction system used by Settari et al. (2001).

The Settari et al. (2001) model domain is one half of the fracture width but does not include any modeling along the fracture height. Romero et al. (2001), realizing the need for 3D simulation, expanded the model to include changes along the fracture height. However, both the more advanced Settari et al. (2001) and Romero et al. (2001) models use analytical velocity profiles in the solution of the acid convection and diffusion, failing to couple fundamentally these processes.

Settari et al. (2001) and Romero et al. (2001) include comparisons of their multidimensional models to earlier models of acid fracturing. Settari et al. (2001) model laboratory experiments and one field case with one- and two-dimensional (gridding across the fracture width and length) simulations. The one-dimensional (1D) model consistently under predicts the etched width across the fracture length for both the laboratory studies and the one field example. Romero et al. (2001) also compare their 3D model to a previous 1D model developed within that research group, similar to Settari et al. (2001), but Romero et al. (2001) use realistic field cases instead of laboratory scale simulations. Interestingly, the 1D model over predicts the acid-etched width for the first presented case study and under predicts the acid-etched width for the second presented case study (as compared to the 3D model output). Romero et al. (2001) do not conclude that the 1D method is consistently over or under predicting the acid-etched width, stating only that a “3D acid-distribution profile can have a significant impact on the spatial etched-width profiles and hence, the etched-fracture conductivities.”

Various commercial software packages are available to calculate the ideal acid-etched width and Nierode-Kruk conductivity from an acid fracture treatment. These simulators prioritize solving the geomechanical propagation of the fracture, which depends on the internal fluid pressure. The pressure does not change significantly across the fracture width, however, so the commercial grid schemes do not include gridding across the fracture width. Run time is also a priority in these commercial models. Assumptions regarding the acid concentration profile and resultant etching are convenient. Different approaches are used by each program, depending on how the fluid transport within the fracture is calculated. None are so rigorous as to calculate the acid convection along and across the fracture, couple this to the diffusion, and determine the acid-etched width from a computed acid concentration profile.

Given the improvements in computational speed and memory, it is now practicable to have a model that numerically resolves the velocity, apparent viscosity, pressure, acid concentration, and resultant etched width during an acid fracture treatment. Gridding should be fully 3D to compute the diffusion and convection of acid to the fracture surfaces. No assumptions need to be made about the velocity profile or distribution of acid within the fracture. This information can be calculated directly from first principles based on fluid mechanics and chemistry. The etching and movement of the fracture surfaces can also be tracked using a non-uniform grid in the fracture width direction. The leakoff experienced by each grid may change and be updated with respect to time. The final output for such a simulation is the acid-etched width and conductivity per grid block, so that the overall distribution of conductivity can be observed by the engineer for a given acid fracture treatment design.

1.3 Objectives of Research

The overall purpose of this research is to develop a general, portable, three-dimensional model of acid transport and dissolution in a fracture. The model must have the following functions:

1. Read any typical fracture geometry as input for the simulation domain.

The model is constructed so that it can use the fracture geometry generated by commercial hydraulic fracture simulators. Analytical solutions may also provide the input fracture geometry, consisting of radial, PKN (Perkins-Kern-Nordgren), or KGD (Khristianovitch-Geertsma-de Klerk) fractures. This input geometry is the basis for fluid transport calculations in the fracture.

2. Calculate the 3D velocity field in the fracture.

The acid convection model considers different numerical techniques for determining the velocity throughout the fracture. These discretize and solve the Navier-Stokes equations, which quantify the velocity fields and pressure in the fracture. The option is also provided for the fluid to be non-Newtonian with power law, apparent viscosity. This affects the convergence of the numerical method used to calculate the velocity fields.

3. Resolve the acid concentration profile throughout the fracture.

The acid profile must be defined throughout the fracture to quantify the acid that reaches the fracture surface to create etching. The model must have fine enough gridding in the fracture to calculate both the diffusive and the convective fluxes of acid to the fracture walls accurately. The model output is compared to analytical solutions to understand what gridding is appropriate for most real world scenarios.

4. Calculate the acid-etched width and conductivity.

The resolved acid concentration profile is used to calculate the acid-etched width, which is based on acid that diffuses toward and leaks off into the fracture surface. The acid-etched width, input geostatistical and rock mechanical properties are used to calculate the Mou-Deng conductivity (Deng et al., 2012). The model yields the amount of dissolution that has occurred in every fracture grid block and the final distribution of created acid fracture conductivity.

5. Conduct a parametric study and evaluate practicality with field data.

The model is tested for a range of parameters representative of actual acid fracture treatments. This includes running different input effective diffusion coefficients, apparent viscosity data, mineralogy, temperature, acid concentration, acid volume, fracture geometry, geologic layering, completion effects and acid types. A case study with industry supplied data demonstrates the model workflow and practicality.

CHAPTER II

MODEL DEVELOPMENT

Conductivity describes the performance of a particular acid fracture treatment. The acid-etched width is a critical factor in estimating the conductivity resultant from a treatment and depends on the movement of acid within the fracture. The acid that reaches the faces of the fractures is what generates acid-etched width. The acid reaches the fracture surfaces either by convection or by diffusion because of a chemical gradient. The first step in resolving the acid concentration profile in the fracture to calculate the acid-etched width and conductivity is to determine the movement of fluid and acid through the fracture.

The importance of the fluid flow solution to the acid concentration profile is demonstrated by the convection-diffusion equation for acid in the fracture (Eq. 2.1).

$$\frac{\partial C}{\partial t}+\frac{\partial (Cv_x)}{\partial x}+\frac{\partial (Cv_y)}{\partial y}+\frac{\partial (Cv_z)}{\partial z}=\frac{\partial}{\partial y}\left(D_{eff}\frac{\partial C}{\partial y}\right) \quad \textbf{(2.1)}$$

In this equation, the acid concentration, C, changes with time along the length (*x*-direction), width (*y*-direction), and height (*z*-direction) in the fracture. The three convection terms are related to the effective diffusion in the fracture, D_{eff}, which is only considered in the width direction in the above expression. Diffusion occurs in any direction in which a concentration gradient is present. However, in acid fracturing, the largest concentration gradient occurs across the fracture width. The acid concentration may be close to zero at the fracture walls, but it can be near the pumped concentration at the center of the fracture despite fracture widths that are usually fractions of an inch. For this reason, the diffusion along the fracture height and length are typically neglected.

The convection-diffusion equation for the acid concentration in a fracture depends on the three-dimensional velocity profile of the injected fluid. Each velocity component (v_x, v_y, v_z) is used in the discretized convection-diffusion equation to calculate the concentration of acid everywhere in the fracture. It is important that the velocity field be resolved accurately to avoid carrying errors or unphysical assumptions into the acid concentration solution.

2.1 Previous Approaches to the Acid Fracture Fluid Velocity Profile

Different approaches have been tried with respect to quantifying the flow of acid throughout a fracture. Simple plug flow models were the first attempt by the industry to understand fluid movement through a fracture for acid fracture treatment design (Coulter et al., 1974; Novotny, 1977). More recent models of acid fracture treatments rely upon analytical velocity profiles or velocity profiles that have been integrated across one or two dimensions (Settari, 1993; Settari et al., 2001; Romero et al., 2001).

Settari (1993) used an integrated velocity profile over the fracture width and height to determine the acid concentration throughout a fracture (Eq. 2.2).

$$-\frac{\partial\left(\bar{v}A_C\overline{C}\right)}{\partial x} = \frac{\partial A_C\overline{C}}{\partial t} + 2\left[q_L C_B + HK_g\left(\overline{C} - C_B\right)\right] - q_{inj}C_i \quad \textbf{(2.2)}$$

The superscript bar over the velocity, v, and the acid concentration, C , denotes an average integrated over the fracture height and width (A_C is the fracture cross-sectional area, q_L is the fluid leakoff volumetric rate, C_B is the acid concentration at the fracture surface, H is the fracture height, K_g is an effective mass transfer coefficient across the fracture width, and $q_{inj}C_i$ is the mass of acid entering the fracture). The use of an average acid concentration across the fracture width necessitated an effective mass transfer coefficient, K_g, to quantify all transport of acid from the bulk fluid in the fracture to the faces of the fracture. This approach lumps the acid diffusion and convection into one static term that is supplied by the practitioner, and this term largely defines the etching over the fracture surface that is to occur. Only the average velocity in the *x*-direction of the fracture is calculated, which is based on the inlet flow rate.

Recognizing the inadequacy of the K_g coefficient to predict etching accurately, Settari et al. (2001) continued research to include modeling of the fluid flow across the fracture width as well as the acid concentration across this dimension (Eq. 2.3).

$$-\frac{\partial (Cv_x)}{\partial x}-\frac{\partial (Cv_y)}{\partial y}+\frac{\partial}{\partial y}\left(D_{eff}\frac{\partial C}{\partial y}\right)=\frac{\partial C}{\partial t}-q_{inj}C_i \qquad \textbf{(2.3)}$$

They use the following equations to characterize the laminar velocity profile for a Newtonian fluid and a non-Newtonian, power law fluid, respectively (Eqs. 2.4-2.5):

$$v_x(y)=v_x(0)\left[1-\left(\frac{y}{b/2}\right)^2\right] \qquad \textbf{(2.4)}$$

$$v_x(y)=v_x(0)\left[1-\left(\frac{y}{b/2}\right)^{(1+n)/n}\right] \qquad \textbf{(2.5)}$$

The above equations are for the laminar, *x*-direction velocity profile between infinite, impermeable parallel plates. The n term is the non-Newtonian power law exponent in Eq. 2.5. The maximum or fracture centerline velocity, $v_x(0)$, determines the magnitude of the velocity profile. This approach, however, does not couple the *y*-direction velocity component of the fluid with the *x*-direction velocity component. The leakoff flow must be known a priori and then subtracted from the flow rate in the fracture. The change in flow rate is used to determine the average *x*-direction velocity by Eq. 2.6, and then the two-dimensional continuity equation is used to resolve the *y*-direction velocity components (Eq. 2.7).

$$\bar{v}_x b = Q_i - v_L \Delta x_L H - \Delta Q_{acc} \quad \textbf{(2.6)}$$

$$\frac{\partial v_x}{\partial x} + \frac{\partial v_y}{\partial y} = \frac{\partial A}{\partial t} - q_{inj} \quad \textbf{(2.7)}$$

The fracture width is b, the volume of fluid lost to leakoff is $v_L \Delta x_L H$ (the leakoff velocity multiplied by the fracture length and height to a point within the fracture), and the fluid filling the fracture interior to a point within the fracture is ΔQ_{acc}. The change in the fracture volume as etched width is created is quantified with $\partial A/\partial t$, and the injection rate to one fracture wing is q_{inj}. This approach allows discretization of the fracture width and length, but the acid concentration is assumed to be unchanging along the fracture height (*z*-direction).

There remained a need to couple the physics and chemistry of acid transport across all three dimensions in the fracture. Romero et al. (2001) conducted simultaneous research to include the effects of changing acid concentration along the fracture height. The *z*-direction velocity is calculated with an equation that is identical in form to the *x*-direction analytical profile used by Settari et al. (2001), since it is based on the average velocity along the fracture height. All three velocity components are used in the three-dimensional acid convection and diffusion equation. This work was largely replicated by Guo et al. (2004) whose main contribution was to include the effective diffusion in the vertical direction along the fracture height.

Commercial fracture analysis packages prioritize calculation of the internal fracture pressure, which does not change much across the fracture width but may vary significantly along the fracture length and height. Fluid flow solutions therefore may be two-dimensional along the fracture length and height (Barree, 1983; Meyer, 1989; Smith, 2010) but are also one-dimensional (Settari and Cleary, 1984). These approaches are based on an influent flow rate with known leakoff subtracted along the fracture length and height. There is no gridding across the fracture width. Some concentration profile is assumed by these programs, and the acid-etched width is calculated with this profile to determine the acid fracture conductivity.

A researcher studying acid fracture treatment design has yet to calculate the velocity field from first principles and couple it with the diffusion, reaction, and leakoff of acid during an acid fracture treatment. Recent efforts by Mou et al. (2010) are the most rigorous to date with calculation of the three-dimensional flow field through a section of an acid fracture. This model was developed for a ten foot by ten foot section of a fracture and used to create the zero stress conductivity correlations presented in

Deng et al. (2012). The original source code and approach presented in Mou (2009) is extended to model an entire acid fracture during any stage of acid fluid injection.

2.2 Fundamental Flow Equations and Apparent Viscosity

The solution of the fluid velocity components starts with the Navier Stokes equations (Eqs. 2.8-2.9) (Tanner, 1988). The subscripts in this section follow the Einstein notation and summation convention, whereby repeated subscript letters in a term indicate summation of the three directional components.

$$\frac{\partial \sigma_{ij}}{\partial x_j} + \rho f_i = \rho \left\{ \frac{\partial v_i}{\partial t} + v_j \frac{\partial v_i}{\partial x_j} \right\} \quad \text{......} \quad \textbf{(2.8)}$$

$$\sigma_{ij} = -p\delta_{ij} + 2\mu d_{ij} \quad \text{......} \quad \textbf{(2.9)}$$

The stress tensor (σ_{ij}) and body forces (f_i) are related to the unsteady movement of the fluid in the fracture with mass being conserved. In the solution of the equations, all body forces (including gravity) are neglected. The stress tensor is equal to the pressure gradient and the rate of deformation tensor (d_{ij}) multiplied by the fluid viscosity (μ). The rate of deformation tensor depends on the velocity field as shown in Eq. 2.10.

$$d_{ij} = \frac{1}{2}\left(\frac{\partial v_i}{\partial x_j} + \frac{\partial v_j}{\partial x_i} \right) \quad \text{......} \quad \textbf{(2.10)}$$

A Newtonian fluid has constant viscosity, so that the Navier Stokes equations simplify to Eq. 2.11 (neglecting body forces and applying conservation of mass).

$$-\frac{\partial p}{\partial x_i} + \mu \frac{\partial^2 v_i}{\partial x_j^2} = \rho \left\{ \frac{\partial v_i}{\partial t} + v_j \frac{\partial v_i}{\partial x_j} \right\} \quad \textbf{(2.11)}$$

Equation 2.11 is the equation typically resolved into three dimensions when the Cartesian, Newtonian Navier Stokes equations are presented.

The Navier Stokes equations appear differently when the viscosity is not constant. This is the case for non-Newtonian fluids in which the apparent fluid viscosity depends on the velocity field of the fluid. Many completion fluids are non-Newtonian (API, 2004). Despite fracture gels having viscoelastic properties, the apparent fracture fluid viscosity is typically modeled by the petroleum engineering industry as having power law fluid properties (Cameron and Prud'homme, 1989; Shah and Lord, 1992; Goel and Shah, 2001). The expression for the apparent power law fluid viscosity is presented in Eq. 2.12 (Bird et al., 1987).

$$\mu_{app} = K\left(\sqrt{2II_d}\right)^{n-1} \quad \textbf{(2.12)}$$

In the above expression, K is the power law fluid consistency index and n is the power law exponent. The II_d term is the second invariant of the rate of deformation tensor. This is calculated with Eq. 2.13.

$$II_d = d_{ij} d_{ji} \quad \textbf{(2.13)}$$

The apparent viscosity is therefore dependent on the velocity field, but the Navier Stokes equations include the apparent viscosity in the resolution of each velocity component.

The Navier Stokes equations may be presented with the inclusion of the apparent power law fluid viscosity. There are two terms that result from this inclusion due to the chain rule: the original fluid diffusion term with the apparent viscosity as the coefficient, and a second term that involves the gradient of the apparent viscosity. This is described by Eq. 2.14.

$$-\frac{\partial p}{\partial x_i} + \mu_{app}\frac{\partial^2 v_i}{\partial x_j^2} + 2d_{ij}\frac{\partial \mu_{app}}{\partial x_j} = \rho\left\{\frac{\partial v_i}{\partial t} + v_j\frac{\partial v_i}{\partial x_j}\right\} \quad \textbf{(2.14)}$$

The new apparent fluid viscosity model and the additional term must be included in the standard numerical approach used to solve the Newtonian Navier Stokes equations. The inclusion of these terms to the Newtonian model developed by Mou (2009) is presented in Appendix A.

2.3 Numerical Method for Solution of the Acid Flow Field

Various numerical schemes exist for the calculation of the three-dimensional velocity fields from the Navier Stokes equations. For incompressible flows, there are three momentum equations and the continuity equation to resolve four variables: the three components of the velocity field and the pressure in the fracture. The pressure only appears in the three momentum equations. Two philosophies are used by researchers to solve these equations; one relies heavily on iteration and the other is more precise.

The iterative approach uses the standard Taylor series discretization to solve the Navier Stokes equations. The most common algorithm is the semi-implicit method for pressure-linked equations algorithm, which is termed SIMPLE (Patankar, 1980). The premise of this approach is to start with a guessed velocity field, calculate the coefficients for a large pressure coefficient matrix based on the momentum and continuity equations, resolve the pressure by inverting this matrix, and then use the pressure in the momentum equations to calculate the velocity components. If the velocity components are converged and unchanged from before the pressure coefficient matrix inversion step, then the algorithm terminates as the converged velocity and pressure fields have been calculated. Otherwise, the algorithm starts again with the new velocity components and iterates until the convergence criterion is reached (Fig. 2.1).

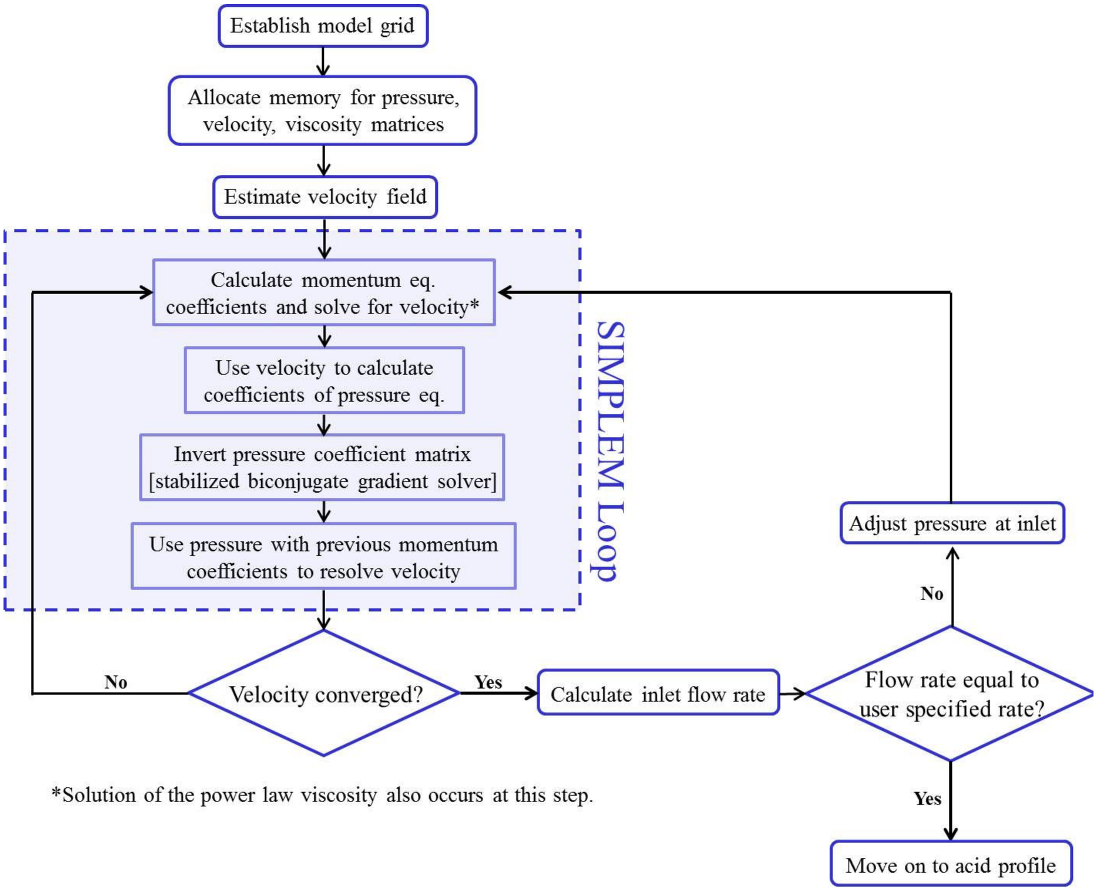

Fig. 2.1—SIMPLEM algorithm as used in Mou (2009) and present model.

Mou (2009) used this iterative approach to resolve the velocity components throughout a fracture with the added complication that irregular grids occur in the fracture width direction (Acharya and Moukalled, 1989). Pressure implicit with splitting of operators (PISO) is another common iterative algorithm. A predictor step with guessed pressure is used to calculate the velocity field implicitly with the momentum equation, the new velocity field is used to calculate the pressure with the divergence of the momentum equation, and this procedure is repeated until the flow has converged (Issa, 1985). There are also other versions of the SIMPLE method (such as SIMPLE modified, which is the approach in Mou (2009)), but all the approaches discussed are essentially iterative, utilizing velocity or pressure corrections to update the pressure or velocity, respectively, until all the fields converge in the Navier Stokes equations. These are the algorithms in commercial computational fluid dynamics software packages such as FLUENT (ANSYS, 2010). The SIMPLE modified (SIMPLEM) method addresses the velocity correction step differently than the traditional SIMPLE algorithm but follows essentially the same approach.

The other approach also uses an infinitely differentiable function for the discretization of the Navier Stokes equations and is termed a spectral method (Canuto et al., 1988). The spectral method typically involves the fast Fourier transform algorithm and/or Chebyshev polynomials to represent the velocity and assign a weight to each grid node in the model domain. This method is best suited for idealized geometries for the solution of the velocity and pressure fields. Spectral methods are very accurate but require additional artificial body forces to be imposed to simulate irregular geometries that deviate from ideal channel or parallel plate flow. Incorporating leaky walls is also challenging with a spectral method. For these reasons, despite the accuracy of more advanced mathematical algorithms for solution of the Navier Stokes equations, the SIMPLEM computational fluid dynamics algorithm is preserved in the original Mou (2009) code to resolve the velocity and pressure fields in an acid fracture.

The same model domain as was developed in the Mou (2009) source code is used, but inactive cells are permitted in the new fracture model. The grid blocks in the *x*- and *z*-directions are regular so that coupling with the fracture geometry models is possible. The code accepts width arrays across the fracture length and height to define the physical model domain with irregular width permitted throughout the fracture. This is the same approach used in Mou (2009), but the new model also accepts locations of zero width in the fracture. This defines the real world, irregular fracture shape. The zero width cells are then deemed inactive cells and only the cells with actual width are used to resolve the velocity, pressure, apparent viscosity, acid concentration and acid-etched width.

2.4 Acid Concentration Profile

Despite the computational effort dedicated to understanding the flow in the fracture, the primary goal of this research is to define the acid concentration everywhere in the fracture. The three-dimensional, convection-diffusion equation is discretized to resolve the acid profile. The converged velocity field for each time step provides the input velocity for the convection terms in the partial differential convection-diffusion equation. The effective diffusion is supplied by the user in an input data file. A large coefficient matrix is created. This matrix is populated with these terms and inverted to determine the acid concentration everywhere. The same stabilized biconjugate gradient solver used for the implicit pressure step in the SIMPLEM algorithm is used to calculate the acid concentration in the fracture (National Institute of Standards and Technology, 2004).

The first order upwinding scheme is classically used to solve convective problems (Patankar, 1980). This approach avoids oscillations that occur when centered finite differences are used, but it suffers from inaccuracies introduced by first order differences (forward or backward finite differences). Mou (2009) used the first order upwinding numerical approach in all three dimensions for solution of the acid concentration profile. Higher order upwinding solutions can be used to offset numerical dispersion produced by the leading error term in the Taylor series approximation. The acid concentration profile will be compared to the analytical solutions derived by previous researchers (Nierode and Williams, 1971; Schechter, 1992) to determine if this is necessary. Otherwise, the discretized convection-diffusion equation created by Mou (2009) will be retained for solution of the acid profile.

2.5 Model Boundary and Initial Conditions

The fluid flow boundary conditions are presented in the following equations. The velocity boundary conditions at the bottom ($z = 0$) and top ($z = H$) of the fracture include a no slip condition (Eq. 2.15).

$$u\big|_{z=0,H}=w\big|_{z=0,H}=v\big|_{z=0,H}=0 \qquad \textbf{(2.15)}$$

The velocity at the fracture tip in the *x*-direction ($x = L$) also includes a no slip condition for the *y*- and *z*-direction velocity components (Eq. 2.16), but the fracture fluid is allowed to leak out the tip of the fracture via the *x*-direction velocity component.

$$w\big|_{x=0,L}=v\big|_{x=0,L}=0 \qquad \textbf{(2.16)}$$

Similarly, flow is only allowed to enter the fracture by the *x*-direction velocity component at the fracture entrance ($x = 0$). The integrated *x*-direction velocity profile over the fracture width and height at the fracture entrance must equal the user specified flow rate (Eq. 2.17).

$$q_{inj}=\int_{0}^{H}\int_{-b/2}^{b/2}u\big|_{x=0} \qquad \textbf{(2.17)}$$

The velocity boundary conditions at the fracture surfaces are presented in Eqs. 2.18-2.19 and use the geometry as depicted in Figure 1.4.

$$u\big|_{y=-b/2,\,b/2}=w\big|_{y=-b/2,\,b/2}=0 \qquad \textbf{(2.18)}$$

$$v\big|_{y=-b/2,\,b/2}=v_L\left(x,z,t,C\right) \qquad \textbf{(2.19)}$$

The *x*- and *z*-direction velocity components are zero on the fracture surfaces (located at $-b/2$ and $b/2$). The *y*-direction velocity at the fracture surface locations is based on a leakoff criterion that changes from a standard hydraulic fracture leakoff coefficient (Penny and Conway, 1989) where the leakoff is inversely dependent on the square root of time to an acid fracture leakoff criterion (Hill et al., 1995). The acid fracture leakoff uses the pore volume to breakthrough of the formation to accelerate the leakoff and reflect the presence of wormholes created by the acid. This leakoff coefficient is also inversely dependent on the square root of time, and it is activated based on the concentration of acid at the fracture surfaces. The boundary condition for the fluid leakoff, v_L, may therefore change based on the fracture height and length locations and is updated with respect to time and the acid concentration.

The initial and boundary conditions for the acid concentration profile are presented in the following equations. The acid concentration is initially zero everywhere in the fracture (Eq. 2.20).

$$C\big|_{t=0} = 0 \qquad \textbf{(2.20)}$$

The acid concentration along the fracture tip in the height and length locations is zero during the treatment, reflecting no fracture width or acid mass at these locations (Eq. 2.21).

$$C\big|_{z=0,H} = C\big|_{x=L} = 0 \qquad \textbf{(2.21)}$$

The acid concentration at the fracture inlet is full strength and the user specified concentration for the duration of the treatment acid stage (Eq. 2.22).

$$C\big|_{x=0} = C_i \qquad \textbf{(2.22)}$$

The reaction of acid at the fracture surfaces governs the acid concentration there and is defined by Eq. 2.23, following the approach used by previous researches to model finite reacting acid/mineral systems (Roberts and Guin, 1974; Settari 1993).

$$D_{eff}\frac{\partial C}{\partial y}=k\left(C_B-C_{eqm}\right)^{n'}\left(1-\phi\right) \quad \text{.......... (2.23)}$$

The equilibrium concentration for acid, C_{eqm}, is significant for weak acids and should be nonzero for these acid/mineral systems.

2.6 Acid-Etched Width and Conductivity

The acid concentration profile defines the concentration of acid that reaches the fracture surface and reacts to create etched width. The same equations as presented in the Mou (2009) model are used to calculate this etching (Eq. 2.24).

$$\frac{\partial y}{\partial t}=\frac{\beta MW_{acid}}{\rho\left(1-\phi\right)}\left(f_r v_L C_B - D_{eff}\frac{\partial C}{\partial y}\right) \quad \text{.......... (2.24)}$$

The acid type may be changed by altering the gravimetric dissolving power, β, and the molecular weight of the acid, MW_{acid}. The fraction of acid to react before leaking off into the formation, f_r, is input by the user as is the mineralogy and its formation properties (porosity, ϕ, and density, ρ). The leakoff velocity, v_L, is indirectly specified by the user with the efficiency of the fracture input by the user.

The acid-etched width is used directly in the Mou-Deng conductivity equations (Deng et al., 2012). The initial, average leakoff velocity and mineralogy (if appropriate) are used to select the conductivity correlation and average width expression that are applied to calculate the fracture conductivity. Conductivity is calculated at every grid block across the fracture half-wing.

2.7 Model Workflow

The model starts with input data supplied by the user, which includes a geometry file with the arrays of width over the fracture height and length and a general input data file that includes all the fluid parameters (pump rate, power law characteristics, acid effective diffusion, acid concentration, etc.). These data files are automatically opened when the code is executed.

The model then runs the fluid solution portion of the code. This is based on the SIMPLEM algorithm, which must calculate the pressure and velocity fields until they meet a convergence criterion. The apparent viscosity is also calculated if the fluid is specified as being a power law fluid in the input data file. Once the pressure and velocity fields converge, the velocity at the fracture inlet is numerically integrated. If it is within ten percent of the user specified inflow rate, then the code starts on the acid concentration profile. Otherwise, the code adjusts the pressure at the entrance of the fracture and the SIMPLEM algorithm is run again. This loop continues until the user specified inflow rate is matched to within the convergence criterion of ten percent.

The acid concentration profile is resolved once the fluid velocity fields have converged. This uses the same solver as the implicit pressure portion of the SIMPLEM algorithm (stabilized biconjugate gradient). The acid concentration is determined at every grid node in the fracture, but the acid concentration near the fracture surface is what is passed to the function that calculates the acid-etched width.

The acid-etched width is calculated based on the concentration profile and used to calculate the conductivity in the fracture. The conductivity is calculated at every time step during the user specified acid injection time. The final output is then the conductivity created by the total acid-etched width generated during the acid injection stage.

The overall workflow is summarized in Figure 2.2.

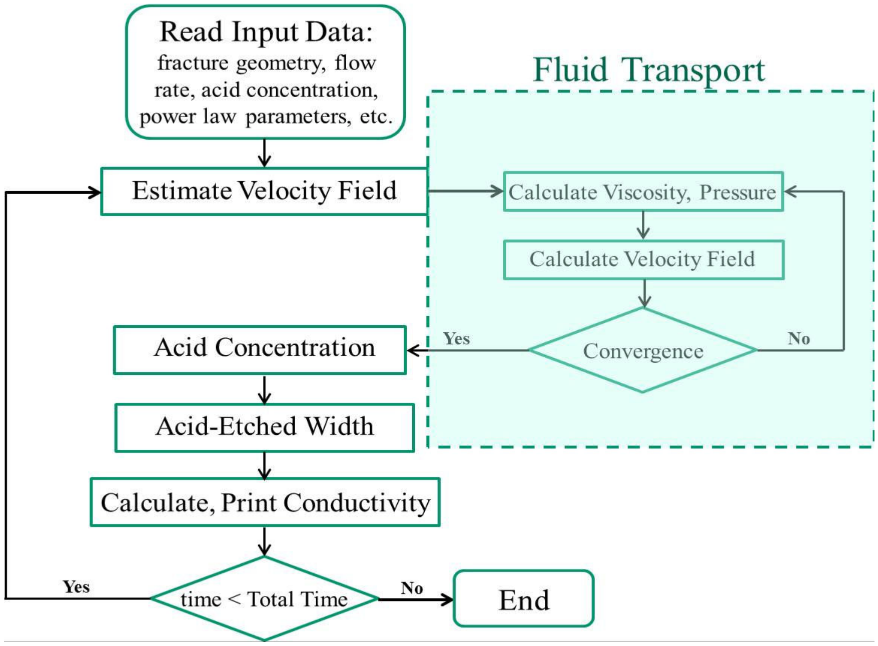

Fig. 2.2—General workflow of the acid fracture model.

2.8 Model Assumptions and Limitations

The model has the following assumptions built into the acid transport methodology:

1. The fracture geometry does not change during acid injection.

This assumption is the most limiting in the model. The acid injection follows a heavily viscosified pad fluid, which imparts fracture geometry specific to the pad fluid rheology. This assumption is the most critical in the fracture width direction, which affects how the acid is distributed in the fracture (see the definition of the Peclet number in Eq. 1.7). The width changes during acid injection, determining how the acid spends and etching is created. The objective of this work is not to develop an entirely incorporated fracture simulator but to model correctly the movement of acid within a realistic fracture. Future work may investigate how the acid transport model and fracture geomechanical models are to be coupled.

2. The temperature throughout the fracture is isothermal.

The acid injection stage during acid fracturing always follows the injection of a pad fluid to create the fracture geometry. Significant cooling typically occurs during the injection of the pad fluid and some researchers recommend designing the pad not only to create a particular geometry but for cooling purposes as well (Ben-Naceur and Economides, 1989). Reducing the temperature in the fracture slows down the diffusion in the fracture and the reaction at the fracture surfaces. Lower temperatures can also improve the fluid rheology, maintaining the apparent viscosity that props the fracture width to reduce further the diffusion of acid to the fracture surfaces. Temperature modeling in a fracture and particularly that of a reactive fluid with generation of heat at the fracture surfaces is not included in the present model. The injection of thousands of gallons of the pad fluid is assumed to cool the fracture down to some relatively uniform temperature.

3. Gravity, density segregation, and viscous fingering effects are neglected.

Acids, spent acids, and pad fluids have differing densities. Some segregation is therefore expected to occur and is thought to increase the acid diffusion as reaction products fall away from the fracture surface (Schechter, 1992). Additionally, the acid fluid is commonly heavier than the pad fluid if the same water to construct both fluids is used. The acid may therefore under run the pad fluid upon introduction to the fracture. This and any other fluid displacement effects are not considered. The acid fluid is assumed to displace the pad fluid evenly throughout the fracture. No apparent viscosity effects are considered either. This means the less viscous acid is not modeled to channel or finger through the more viscous pad fluid in the fracture. Many acid fracture researchers consider this a significant effect in acid fracture treatments, which accounts for streaks of etching along the fracture (Davies et al., 1987; Ben-Naceur and Economides, 1989; Allen, 1995). To the author's knowledge, no experimental research has been conducted to determine whether this fingering occurs for fluids with drastically different pH values.

4. Acid fluids with pH dependent apparent viscosity are not modeled.

The power law apparent viscosity model is most appropriate for gelled acid systems that do not exhibit pH apparent viscosity dependence. The power law model has also been used to describe emulsified acid fluids (Al-Mutairi et al., 2009). However, this simple apparent viscosity model is most appropriate for polymer chained gels without crosslinking agents. Viscoelastic behavior is not included in the model, so more complicated acid fluids are not presently modeled.

5. Diffusion in the *y*-direction is the only acid diffusion considered.

Diffusion occurs anywhere there is a concentration gradient. Diffusion could therefore be included in the *x*- and *z*-directions. For the effect of diffusion to be significant the concentration gradient in that direction must be large. The concentration gradient across the fracture width is the largest with the acid concentration being near zero at the fracture walls and near inlet strength acid possible at the fracture center (a distance less than half an inch). This is compared to the gradient along tens of feet in the fracture length and height directions. Dispersion is also possible in all three directions and has been considered in previous acid fracture modeling work (Settari et al., 2001). It is usually only included in cases with turbulent flow, which do not usually occur during the acid fluid injection stage.

6. The fluid in the fracture is incompressible and single phase.

The acid fluids are constituted mostly of water, so the fluid is assumed to be incompressible. Carbon dioxide is a reaction product of an acid with a carbonate, but the produced carbon dioxide does not evolve at typical fracture pressure and temperature conditions (Hendrickson et al., 1960).

CHAPTER III

ANALYTICAL VALIDATION

This chapter describes the analytical verification of the model presented in Chapter II. The grid numbers used in each direction and corresponding grid block sizes are set to typify simulations that are run using actual field data (grid block length of 21 feet, grid block height of 10 feet, and grid block width of 0.01 in). The purpose of this chapter is not to provide the best match of the analytical solutions possible with the model but to demonstrate that with realistic gridding the model provides satisfactory accuracy. The dimensions of the parallel plate domain used in all the simulations presented in this chapter are 315 ft in the *x*-direction, 150 ft in the *z*-direction, and 0.1 in in the *y*-direction.

3.1 Velocity Profile Match

3.1.1 Newtonian Fluid Between Parallel Plates

The analytical velocity solution for a Newtonian fluid between impermeable parallel plates is presented in Eq. 3.1.

$$u(y) = \frac{\left(p_{x=0} - p_{x=L}\right)\left(\frac{b}{2}\right)^2}{2\mu L}\left(1 - \left(\frac{y}{b/2}\right)^2\right) \quad \text{.......................................} \quad \mathbf{(3.1)}$$

The analytical match of the fluid model for a range of inlet flow rates is shown in Figure 3.1. The stabilized biconjugate gradient tolerance for the implicitly calculated pressure is

10^{-4} and the velocity fields must converge to within 10^{-3} dimensionless units before the SIMPLEM loop is exited. The inlet flow rate must be matched to within ten percent of that stated in the input file. This sets the inlet pressure to the parallel plate flow entrance. The average absolute relative error across the parallel plate domain is less than 0.1% for the range of flow rates investigated.

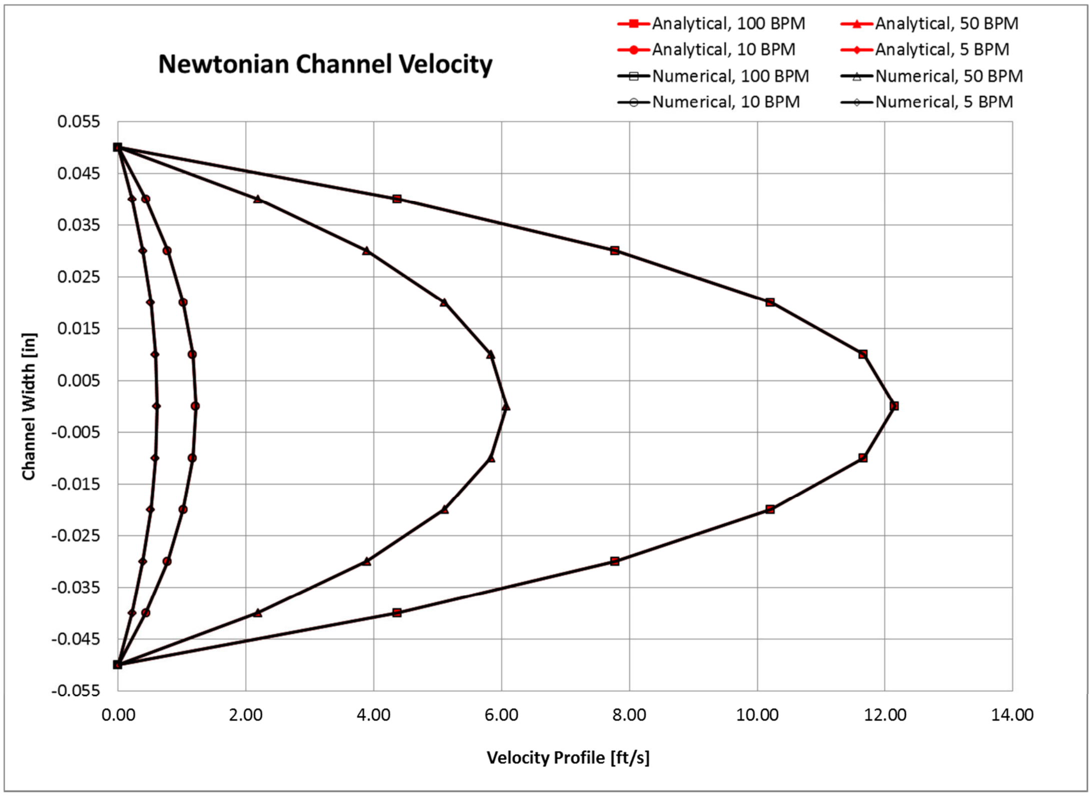

Fig. 3.1—Impermeable parallel plate analytical match for a Newtonian fluid.

The numerically resolved pressure throughout the parallel plate domain is used in the analytical expression to validate the model. The output pressure along the fracture length is presented in Figure 3.2 for an influent rate of 10 BPM.

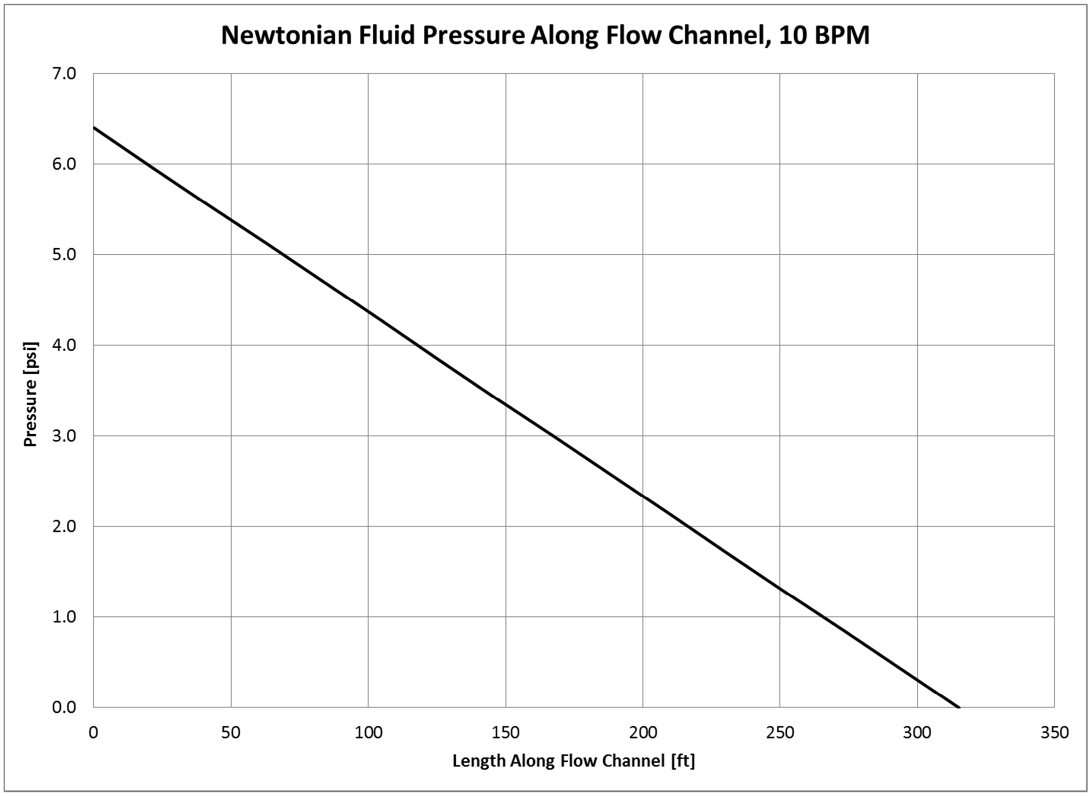

Fig. 3.2—Impermeable parallel plate pressure profile for a Newtonian fluid and 10 BPM flow rate.

The pressure change along the domain in the *x*-direction is constant, which is expected based on the analytical solution. This represents the amount of energy required to push the 1 cp fluid through the constant 0.1 inch flow channel. The constant pressure drop supports the velocity throughout the flow channel, which is constant in this case. The viscosity throughout the channel is also constant, since the fluid is Newtonian. The apparent viscosity will vary between the plates if the fluid is non-Newtonian.

3.1.2 Power Law Fluid Between Parallel Plates

The analytical velocity solution for a non-Newtonian, power law fluid between impermeable parallel plates is presented in Eq. 3.2.

$$u(y)=\frac{K}{\left(p_{x=0}-p_{x=L}\right)/L}\frac{n}{1+n}\left(\left(\frac{\left(p_{x=0}-p_{x=L}\right)}{KL}\frac{b}{2}\right)^{\frac{n+1}{n}}-\left(\frac{\left(p_{x=0}-p_{x=L}\right)}{KL}|y|\right)^{\frac{n+1}{n}}\right) \quad \text{.................} \mathbf{(3.2)}$$

The analytical match for a range of power law parameters consistent for gelled acid fluids (Nasr-El-Din et al., 2008) and an inflow rate of 10 BPM is presented in Table 3.1. A cutoff value must be used in the calculation of the apparent viscosity to avoid a divide by zero error at the center of the flow channel (the shear rate approaches zero). This value is set to an unrealistically low value for matching of the analytical profile in which no such cutoff would be used, but this cutoff will be changed to result in a maximum apparent viscosity no larger than the consistency index and a minimum apparent viscosity of 1 cp when running real cases.

The same tolerances as were used in the Newtonian, impermeable parallel plate solution are applied for the power law velocity profile matches. The code converges with the same computational effort until a power law exponent of approximately 0.65. The increased error expected for power law exponents less than 0.7 is depicted in Figure 3.3. This is due to the discontinuity of the apparent viscosity at the center of the flow channel, which introduces slight errors in the resolved apparent viscosity profile so that the numerical profile differs from the analytical expression. The average absolute relative error for a range of flow rates and $n = 0.65$ is listed in Table 3.2, and the velocity profile match for the same parameters is presented in Figure 3.4. The average absolute relative error is less than 3% for the n values that represent most gelled acid fracture fluids.

Table 3.1—Average absolute relative error compared to the impermeable parallel plate power law fluid velocity analytical solution for varying power law exponents and $q_{inj} = 10\ \text{BPM}$.

Non-Newtonian Exponent	Average Absolute Relative Error (%)
0.9	1.1
0.8	1.1
0.7	1.0
0.6	6.0

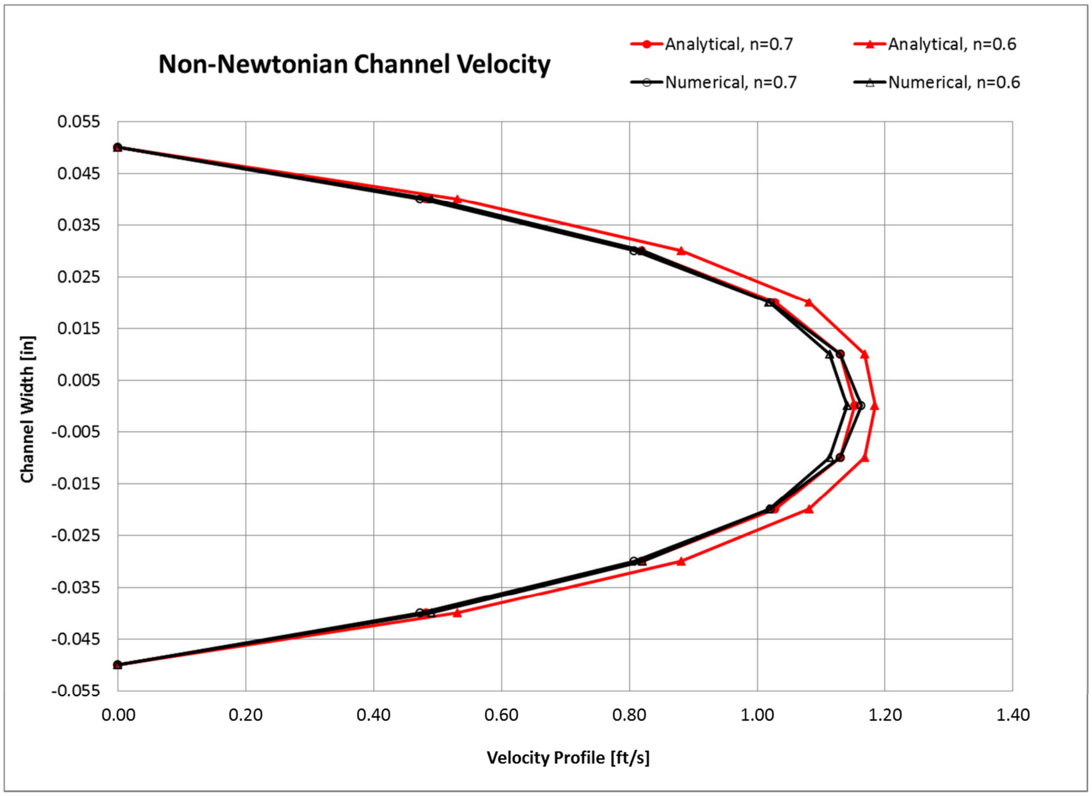

Fig. 3.3—Analytical match for the power law fluid between impermeable parallel plates for n=0.6 and n=0.7 at a flow rate of 10 BPM.

Table 3.2—Average absolute relative error compared to the impermeable parallel plate power law fluid velocity analytical solution for a range of flow rates and n=0.65.

Inflow Rate (BPM)	Average Absolute Relative Error (%)
5	2.9
10	2.9
50	2.9
100	2.9

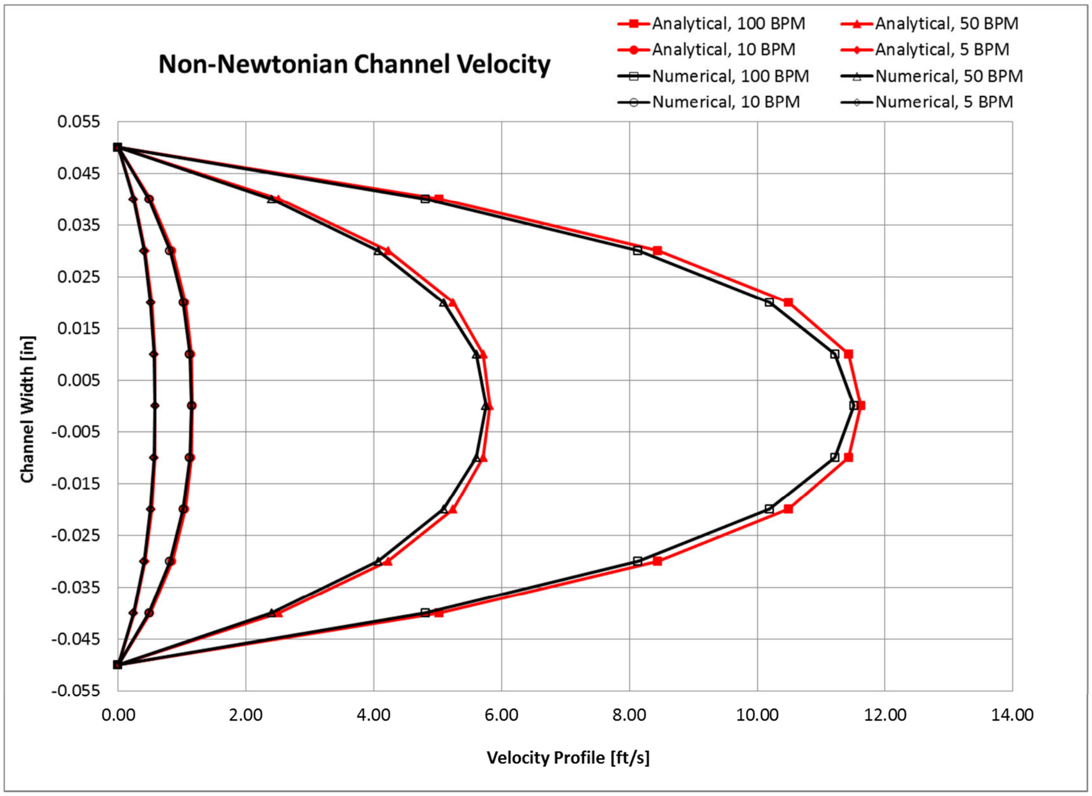

Fig. 3.4—Impermeable parallel plate analytical match for a power law fluid, n=0.65.

The pressure along the parallel plate domain appears similar to that resolved for the Newtonian fluid, but since the apparent viscosity is greater the pressure required to move the fluid is higher (Fig. 3.5).

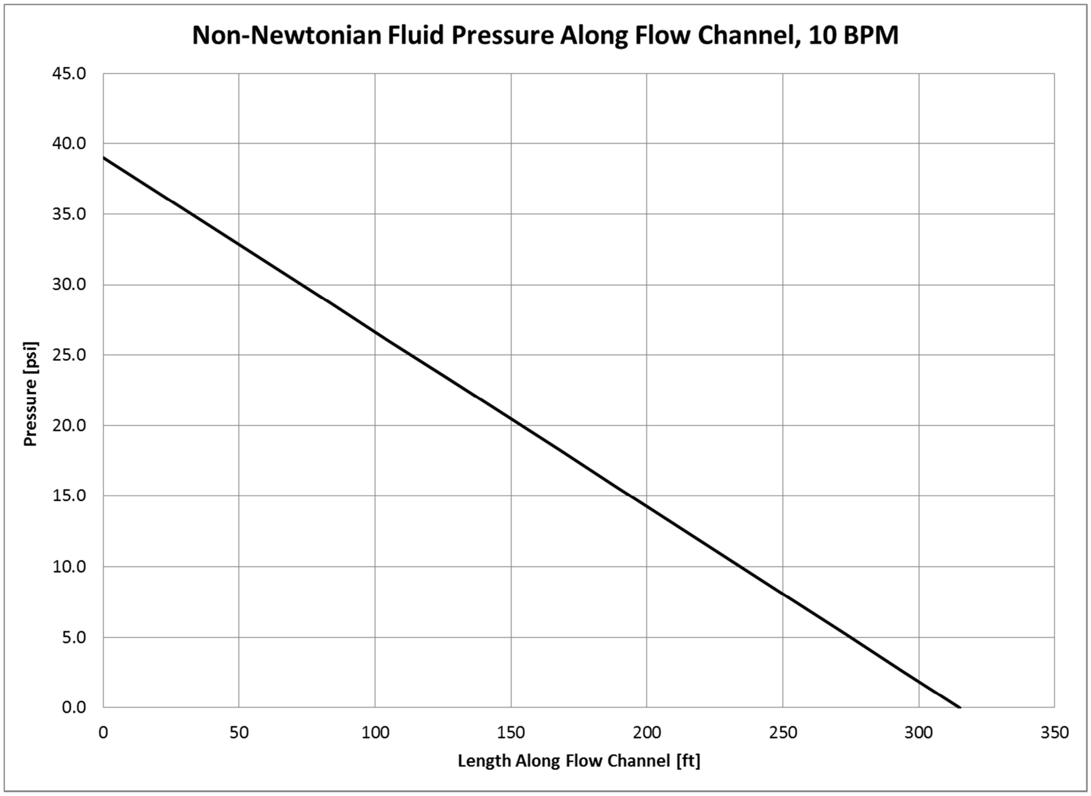

Fig. 3.5—Impermeable parallel plate pressure profile for a power law fluid, n=0.65 and 10 BPM flow rate.

The pressure drop across the domain is linear, which is what is supported based on the analytical expression. The velocity along the domain is constant and of the same magnitude as the Newtonian case, being that the same flow rate is moving between the parallel plates (Fig. 3.4). The differences between the Newtonian and power law profiles are because of the variable power law apparent viscosity. The apparent viscosity has no practical cutoff in the analytical match, so the instability near the centerline where the shear rate is essentially zero is observable in the model output (Fig. 3.6).

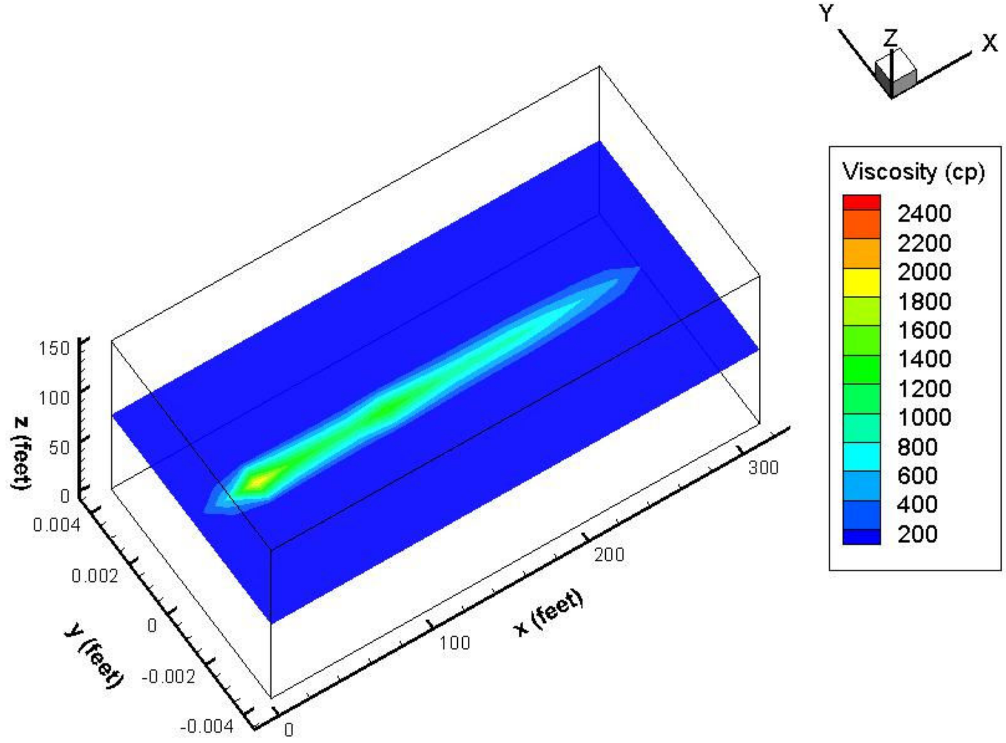

Fig. 3.6—Impermeable parallel plate apparent viscosity profile for a power law fluid, n=0.65 and 10 BPM flow rate.

Theoretically, the apparent viscosity should be constant along the parallel plate domain length. Numerical instabilities cause it to waver slightly along the domain length. These instabilities increase as the fluid becomes more non-Newtonian (the n value decreases) and the centerline apparent viscosity increases relative to the apparent viscosity in other portions of the flow domain. For actual simulations, practical apparent viscosity cutoff values will be used that remove this instability.

3.1.3 Newtonian Fluid Between Leaky Parallel Plates

The analytical velocity solution for a Newtonian fluid between parallel plates with uniformly leaky walls is presented in Eqs. 3.3-3.4 and was derived by Berman (1953).

$$u(x,y)=\left(\bar{u}(0)-\frac{v_L x}{b/2}\right)\left(\frac{3}{2}\left(1-\left(\frac{y}{b/2}\right)^2\right)\left(1-\frac{v_L b}{840\upsilon}\left(2-7\left(\frac{y}{b/2}\right)^2-7\left(\frac{y}{b/2}\right)^4\right)\right)\right) \tag{3.3}$$

$$v(y)=v_L\left(\frac{y}{b}\left(3-\left(\frac{y}{b/2}\right)^2\right)-\frac{v_L}{280\upsilon}y\left(2-3\left(\frac{y}{b/2}\right)^2+\left(\frac{y}{b/2}\right)^6\right)\right) \tag{3.4}$$

The same tolerances as were used in the Newtonian, impermeable parallel plate solution are applied for the Berman (1953) velocity profile matches. The *x*-direction velocity match is presented in Figure 3.7, the *y*-direction velocity match is presented in Figure 3.8, and the average absolute relative error for the four different flow rates is presented in Table 3.3. The parallel plate domain has zero efficiency in these cases, which is the largest flow that can be considered to be leaking out of the channel walls. The Berman (1953) leaky parallel plate solutions are not accurate for large Reynolds numbers $(N_{\mathrm{Re}} < 7)$, but the Reynolds numbers for these cases are all small enough to preserve the accuracy of the analytical solution. The average absolute relative error is consistently less than 3% across the parallel plate domain.

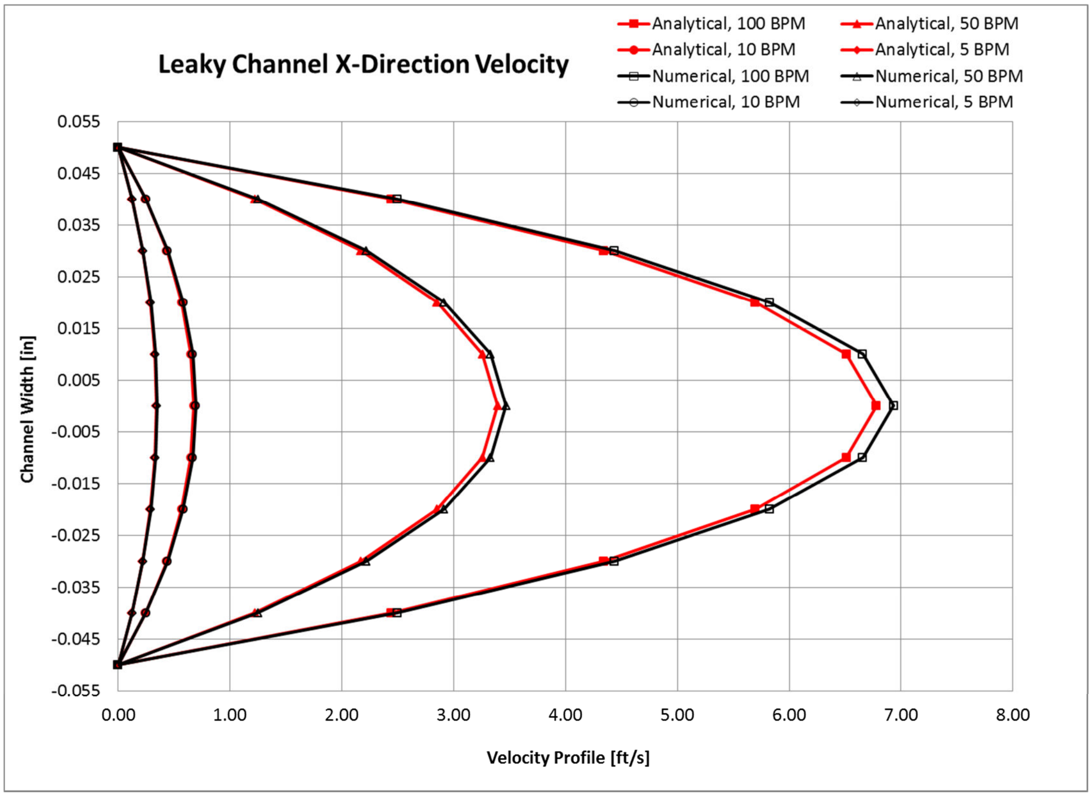

Fig. 3.7—Uniformly permeable parallel plate *x*-direction velocity analytical match for a Newtonian fluid midway along the channel length.

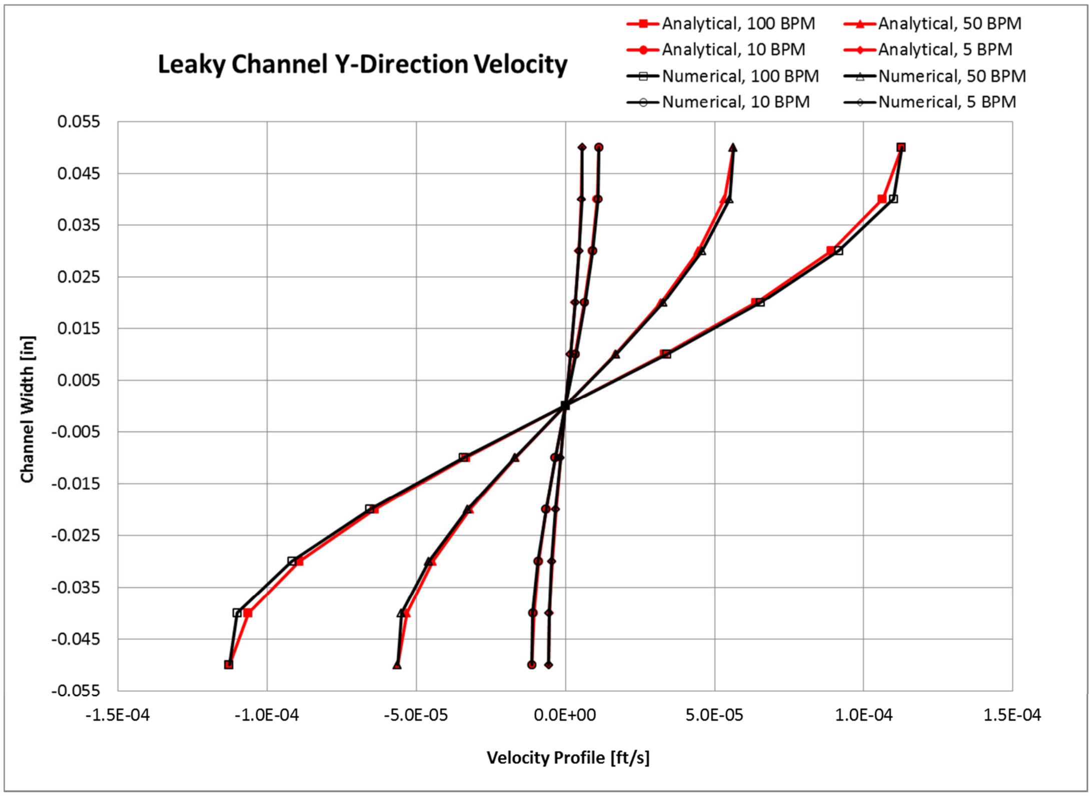

Fig. 3.8—Uniformly permeable parallel plate *y*-direction velocity analytical match for a Newtonian fluid.

Table 3.3—Average absolute relative error compared to uniformly permeable parallel plate Newtonian velocity analytical solutions for a range of channel flow rates.

Inflow Rate (BPM)	Average Absolute Relative Error (%) *x*-Direction Velocity	Average Absolute Relative Error (%) *y*-Direction Velocity
5	2.2	2.8
10	2.2	2.7
50	2.2	2.7
100	2.2	2.7

The pressure across the leaky parallel plate domain is different from the impermeable cases in that less fluid is present toward the end of the domain. Lower flow requires less energy to move, so a nonlinear trend of decreasing pressure is observed in the leaky parallel plate case with lower pressures overall (Fig. 3.9).

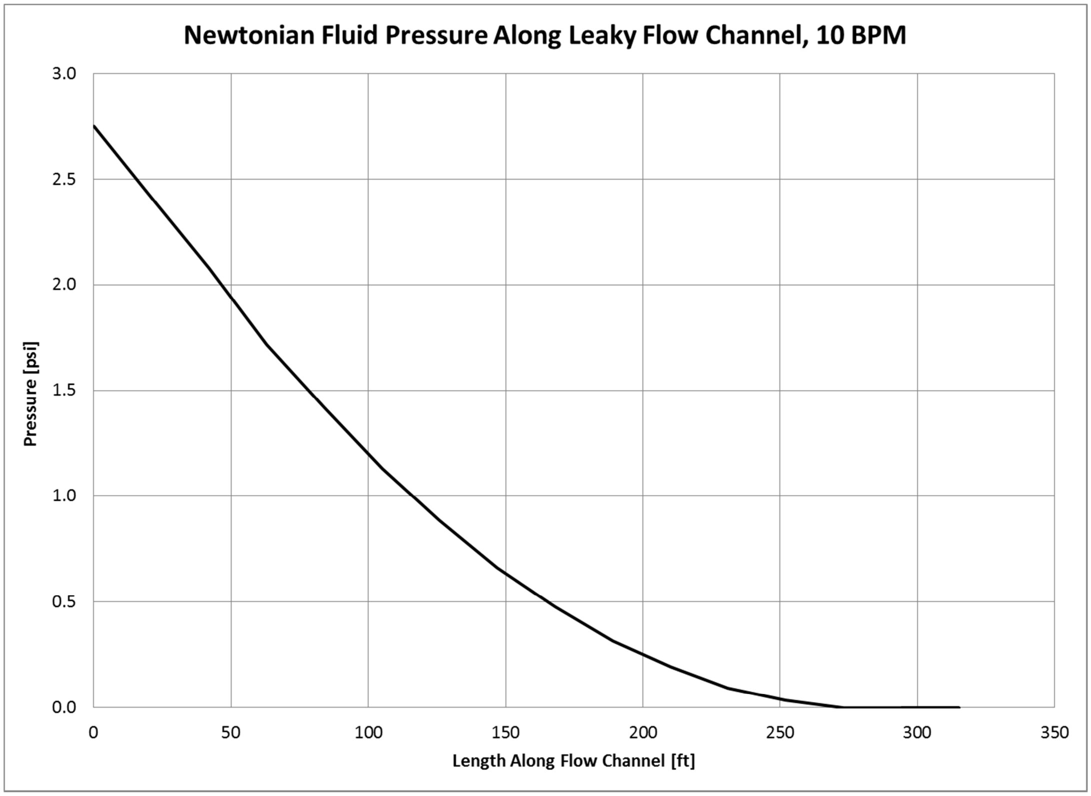

Fig. 3.9—Uniformly permeable parallel plate pressure profile for a Newtonian fluid and 10 BPM flow rate.

The pressure drop is more severe near the parallel plate flow entrance and diminishes as the flow leaks out the channel walls. This is a zero efficiency domain where all the flow entering leaks out the channel walls. The low pressures are also due to the low viscosity (1 cp fluid as with the Newtonian impermeable parallel plate case). The uniform leakoff applied at the flow channel walls removes the flow as it progresses so that no flow is present at the end of the parallel plate domain. This is demonstrated by the output *x*-direction velocity profile, which shows diminishing flow in the *x*-direction (Fig. 3.10).

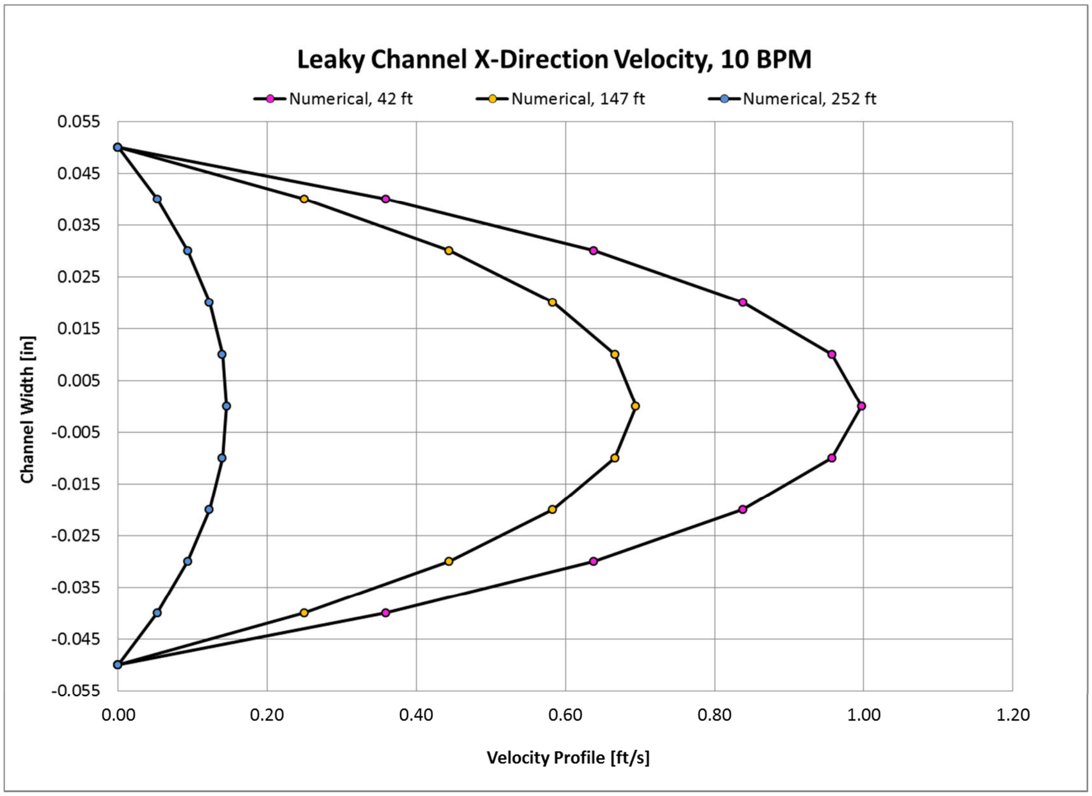

Fig. 3.10—Uniformly permeable parallel plate *x*-direction velocity profile for a Newtonian fluid and 10 BPM flow rate at three locations along the flow channel length.

3.2 Acid Profile Match

The acid concentration analytical profile match is developed with the leaky parallel plate flow solution and is presented in Figure 3.11.

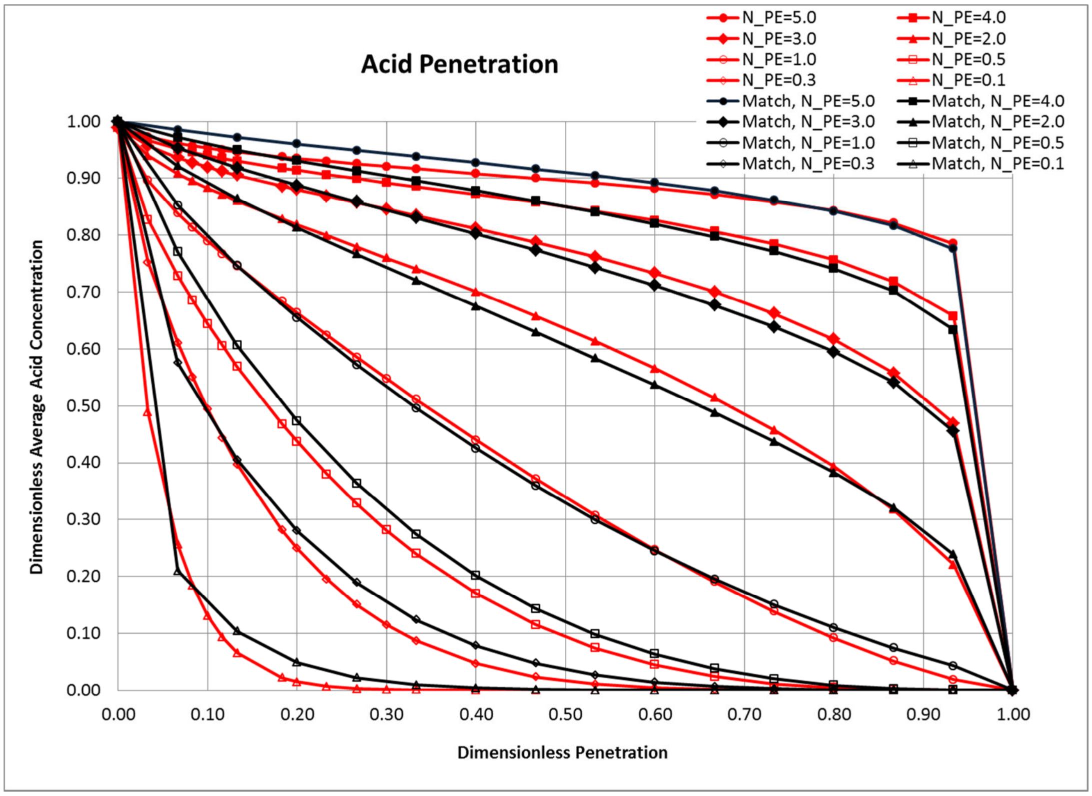

Fig. 3.11—Uniformly permeable parallel plate with Newtonian fluid, acid penetration analytical match for an infinitely reactive acid/mineral system over a range of Peclet numbers.

This match required expanding the Mou (2009) first order upwinding approach to a second order upwinding approach in the dominant flow direction (*x*-direction) for higher Peclet numbers $\left(N_{Pe} > 1\right)$. This is due to the sharp gradient between the concentration of acid in the flow channel and that at the very end of the domain, which is zero. Note that the analytical solution is for a zero efficiency fracture, so the acid concentration at the very end of the domain must be zero. The first order discretization of the derivative in the *x*-direction originally appeared as in Eq. 3.5.

$$u\frac{C_{i,j,k}-C_{i-1,j,k}}{\Delta x}=u\frac{\partial C}{\partial x}-u\frac{\Delta x}{2}\frac{\partial^2 C}{\partial x^2}+u\frac{(\Delta x)^2}{6}\frac{\partial^3 C}{\partial x^3}+HOT \quad \textbf{(3.5)}$$

This expression was expanded to a second order discretization scheme as shown in Eq. 3.6.

$$u\frac{0.5C_{i-2,j,k}-2C_{i-1,j,k}+1.5C_{i,j,k}}{\Delta x}=u\frac{\partial C}{\partial x}-u\frac{(\Delta x)^2}{3}\frac{\partial^3 C}{\partial x^3}+u\frac{(\Delta x)^3}{4}\frac{\partial^4 C}{\partial x^4}+HOT \quad \textbf{(3.6)}$$

The leading error terms in both schemes are negative, which means the absolute gradient will always be lower than that of the analytical solution (*HOT* represents the higher order terms that are part of the Taylor series expansion and not explicitly written). This is the numerical dispersion that appears as smoothing between the high concentration in the flow channel and the zero concentration at the very end of the domain. This is why the acid concentration tends to be under predicted toward the end of the domain for very high Peclet numbers and zero efficiency fractures.

The second order upwinding scheme reduces the effect of discretization error for the same grid dimensions. This is most important in the *x*-direction, since the flow in that direction is typically orders of magnitude larger than that in any other direction and this creates the largest error in the system. A second order upwinding approach was also attempted in the *y*-direction as this direction defines the convection and diffusion that is critical to the shape of the concentration profile and resultant etching. Due to the symmetry of this system, the separation of flow directions at the center of the fracture prevented this approach from converging even if a first order, transitioning to second order approach was implemented. Very slight numerical noise at the fracture centerline created disturbances that prevented the acid concentration profile from converging. The *z*-direction velocity for most fracture geometries is expected to be relatively small, so first order discretization is preserved here. Time steps of one second are recommended to maintain the model's accuracy.

The fluid velocity and acid concentration profile problems have opposing numerical qualities. The largest error term in the acid concentration problem is directly dependent on the grid block size in the *x*-direction. To solve the fluid flow problem, however, the grid block size in the *x*-direction must be large enough to satisfy the Courant-Friedrichs-Lewy (CFL) stability criterion (Fletcher, 1991). This criterion essentially states that the flow in any one direction cannot exceed the grid block length in that direction in one time step and is described by Eq. 3.7.

$$\frac{v_i \Delta t}{\Delta x_i} < 1 \qquad \textbf{(3.7)}$$

The code occasionally converges if grid block sizes slightly beyond the recommended CFL criterion are used, but the resolved velocity profile is inaccurate when analytically compared and quickly becomes unstable as increasingly small grid block sizes are used. The acid solution, however, is observed to benefit from smaller grid block sizes, since the leading error term in each direction diminishes as smaller grid block sizes are used.

For this reason, the acid concentration profile is decoupled from the grid used for the fluid algorithm in the *x*-direction. The *x*-direction velocity component is interpolated between grid nodes using a harmonic average. The finer velocity in this direction is used in the acid concentration algorithm to diminish further the error at high Peclet numbers. The average absolute errors across the range of Peclet numbers appropriate for use of the analytical solution are presented in Table 3.4.

Table 3.4—Average absolute relative error compared to uniformly permeable parallel plate with a Newtonian fluid, acid concentration analytical solution for a range of Peclet numbers.

Peclet Number	Average Absolute Relative Error for Concentration Profile (%)
0.1	1.1
0.3	1.7
0.5	2.3
1.0	1.4
2.0	1.4
3.0	1.0
4.0	1.0
5.0	1.4
6.0	2.0
7.0	2.8

Both first order and second order upwinding schemes in the *x*-direction are used to produce Table 3.4. For very low Peclet numbers the first order scheme under predicts the severe concentration profile near the fracture entrance, so a weighting function is used to decrease uniformly the first order scheme acid concentration profile throughout the fracture. The weighting factor goes from zero to one and was constructed to match the analytical expression for the acid concentration profile at Peclet numbers below 0.5. At moderate Peclet numbers, second order upwinding in the *x*-direction is used in combination with the first order upwinding scheme. The initial condition for acid in the fracture is that no acid is present in the fracture. The first order scheme calculates a lower acid concentration profile than is analytically supported. Then the second order scheme determines a new acid concentration profile throughout the fracture, but this concentration is too high as it begins with the resolved profile from the first order upwinding scheme. A polynomial expression has been developed based on matching the analytical acid concentration to assign a weighting factor between the first order (too low) and resolved second order (too high) profiles. Peclet numbers greater than 5.0 use the resolved second order upwinding scheme, which also starts with first order upwinding. The error increases for higher Peclet numbers where nearly inlet strength acid reaches the end of the domain. This error is less than 10% and is confined to the fracture tip grid blocks as very high concentrations of acid are calculated but the sharp gradient cannot be preserved (due to the leading error terms for the first order and second order upwinding approaches). This combined upwinding approach explains the slight uptick in error for Peclet numbers just under 1.0 and Peclet numbers higher than 5.0.

3.3 Etched Width Profile Match

The match of the analytical etched width for a range of Peclet numbers is presented in Figure 3.12.

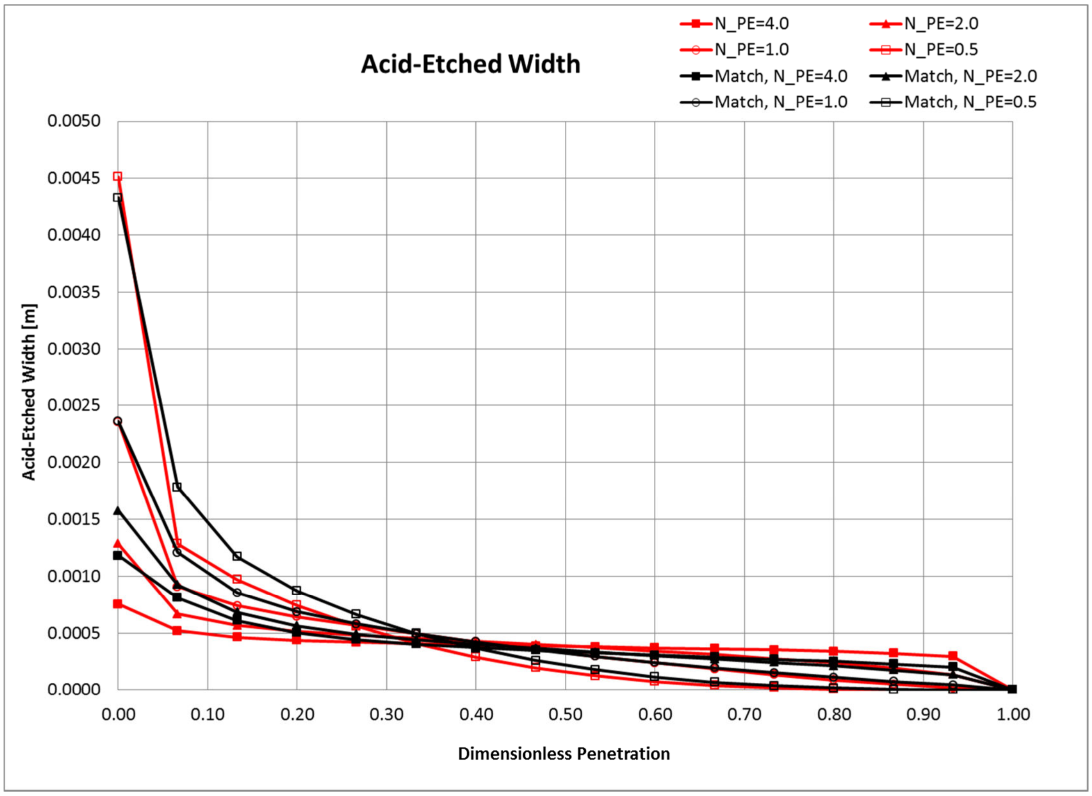

Fig. 3.12—Uniformly permeable parallel plate etched width analytical match for an infinitely reactive acid/mineral system over a range of Peclet numbers.

The shape of the numerically derived acid-etched width agrees with the analytical solution at low Peclet numbers. For higher Peclet numbers, the analytical acid-etched width is more evenly distributed across the length of the fracture than that of the numerically derived acid-etched width. The general trend of more etching near the fracture inlet for lower Peclet numbers and more even etching across the fracture at higher Peclet numbers is demonstrated by the model output. Despite differences between the analytical and numerical solutions in the profile of acid-etched width along the domain, the numerical and analytical solutions agree on conservation of mass to within 1% for $1 < N_{PE} < 7$.

CHAPTER IV

PARAMETRIC STUDY

This chapter presents a range of cases that demonstrate the model capabilities. The cases investigate parameters that are of interest in acid fracture treatment design: the effective diffusion, fluid type, fluid efficiency, pump rate, acid volume, mineralogy, geology, fracture geometry, acid type and concentration.

4.1 Confined Fracture Case Study

All fractures begin as radial fractures until growing sufficiently in height to reach adjoining stress barriers. The fracture then grows in length until the leakoff flow rate approaches the inflow to the fracture. A fracture that has reached adjoining stress barriers to grow at least twice as long in length compared to height has Perkins-Kern-Nordgren (PKN) geometry (Smith, 2007). This fracture geometry is used with the treatment parameters in Table 4.1 to evaluate the model output. The formation heterogeneity parameters $\left(\lambda_{D,x}, \lambda_{D,z}, \sigma_D\right)$ are kept constant with the same values being used for all the case studies presented in this chapter. In reality, these parameters likely change from layer to layer but these properties are held constant here to investigate how changing the acid fluid characteristics and fracture geometry affect the simulation output.

Table 4.1—Input fluid data for simulations.

Acid Type & Concentration	15% by wt. Hydrochloric (HCl) Acid
Mineralogy	Limestone
Effective Diffusion Coefficient	8 x 10^{-6} cm^{2}/s
Injection Temperature	100˚F
Pump Rate	40 BPM (constant), 20 BPM per half-wing
Injection Time	20 minutes
Young's Modulus	4.5 MMpsi
Closure Stress	2000 psi
Pore Volumes to Breakthrough	1.5
Fraction of Acid to React on Surface Before Becoming Leakoff	0.3
Power Law Index	0.65
Consistency Index	0.05 Pa-s^{n}

StimPlan 3D (Smith, 2010) was used to create a PKN type fracture, pumping a 30# crosslinked pad fluid at 40 BPM for approximately 12 minutes to produce a fracture that is about twice as long as it is tall (Fig. 4.1).

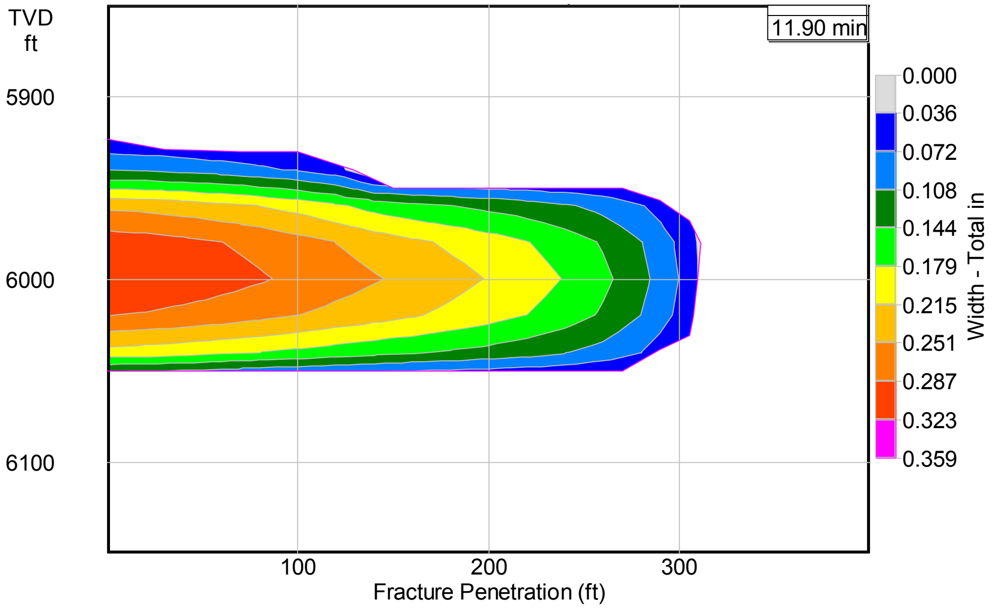

Fig. 4.1—Fracture geometry from StimPlan at end of 30# crosslinked pad injection with stress barriers.

The fracture width is read across the fracture height and length into the acid model as input data to generate the physical domain for the acid injection simulation. Note that the fracture geometry is output at the corners of cells, and the acid model requires the average width located between these nodes to populate each grid block. The average of neighboring nodes of the StimPlan output width across the fracture height and length is what is input to the acid model.

4.2 Fluid Sensitivity

4.2.1 Gelled Acid Treatment Example

The fluid parameters represent a gelled acid system with maximum apparent viscosity of 50 cp in the fracture. It is assumed that the flow can enter the fracture everywhere along the fracture height (i.e., the interval is densely perforated along the entire fracture height). The fracture in this simulation has zero efficiency, meaning all the fluid entering the fracture initially leaks out the fracture walls. The SIMPLEM loop tolerance was raised an order of magnitude for real world cases to encourage velocity convergence (10^{-2}), and a relaxation factor of 0.5 was used for the pressure iterations. All figures presented in this section are captured at the end of the acid fracture treatment.

The calculated fracture pressure is presented in Figure 4.2. This output pressure is relative to a pressure of 0 psi along the fracture boundary and in the inactive cells.

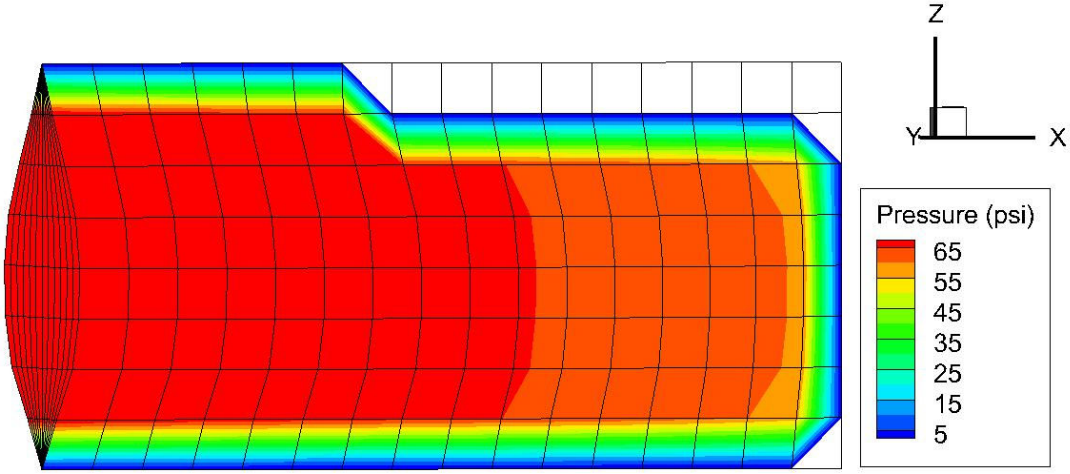

Fig. 4.2—Fracture pressure for the gelled acid case.

The fracture pressure represents the energy required to move the flow down the fracture, otherwise there are no pressure dependent properties in the model. The model output pressure is not the net pressure or pressure related to fracture closure but rather the pressure needed to overcome friction in the fracture to move the fluid. The maximum fracture pressure is at the inlet and decreases along the fracture. The pressure is maintained due to the decrease in fracture width despite the flow decreasing along the fracture due to leakoff and some width generation through acid etching. The apparent viscosity in the fracture is presented in Figure 4.3 at the vertical centerline of the fracture across the fracture width and length.

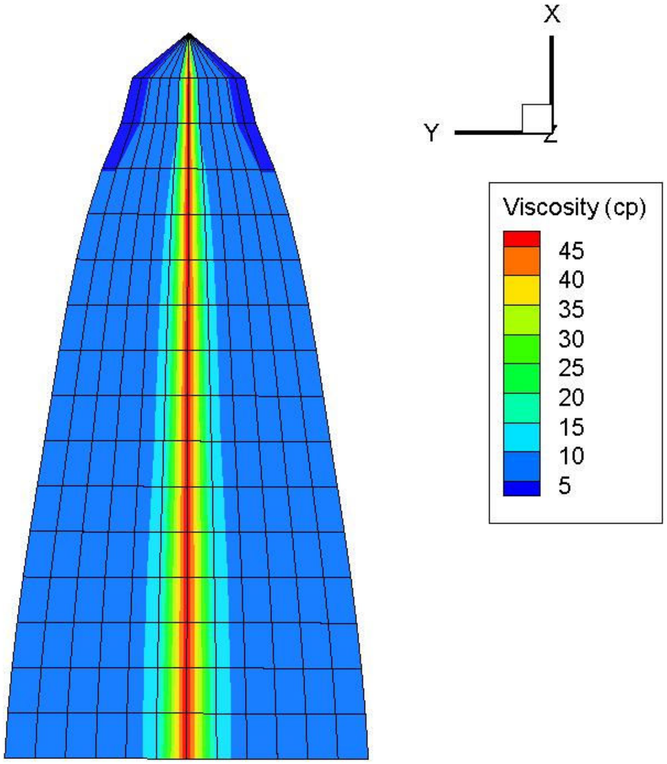

Fig. 4.3—Apparent viscosity across fracture width for the gelled acid case at the vertical centerline.

The apparent viscosity increases toward the center of the fracture where the shear is low. This is the main property of a power law or shear thinning fluid. This band of higher apparent viscosity occurs throughout the center of the fracture with much lower apparent viscosity near the fracture walls. The maximum apparent viscosity of 50 cp is reached at the fracture centerline with respect to width, which is the practical upper apparent viscosity limit for the gelled acid fluid. The apparent viscosity near the fracture surface is approximately 5 cp along the fracture, so the lower apparent viscosity limit of 1 cp is not used in the simulation. The Reynolds number is 429 based on the lowest apparent viscosity near the wall and the inlet fracture velocity (Zhen et al., 2013). Any turbulent flow effects are not included in the model, and research on this topic is ongoing.

The velocity components follow the shape of the fracture. The *x*-direction velocity is shown across the fracture width and height in Figures 4.4-4.5.

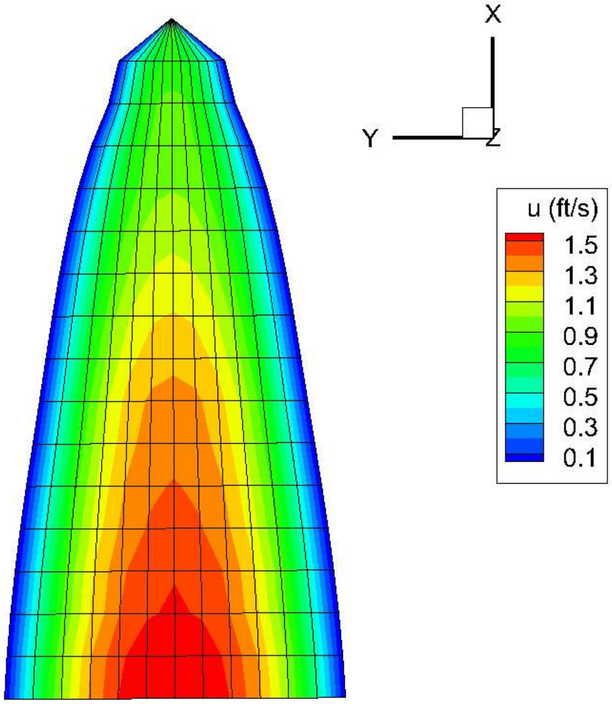

Fig. 4.4—Velocity in the *x*-direction across fracture width for the gelled acid case at the vertical centerline.

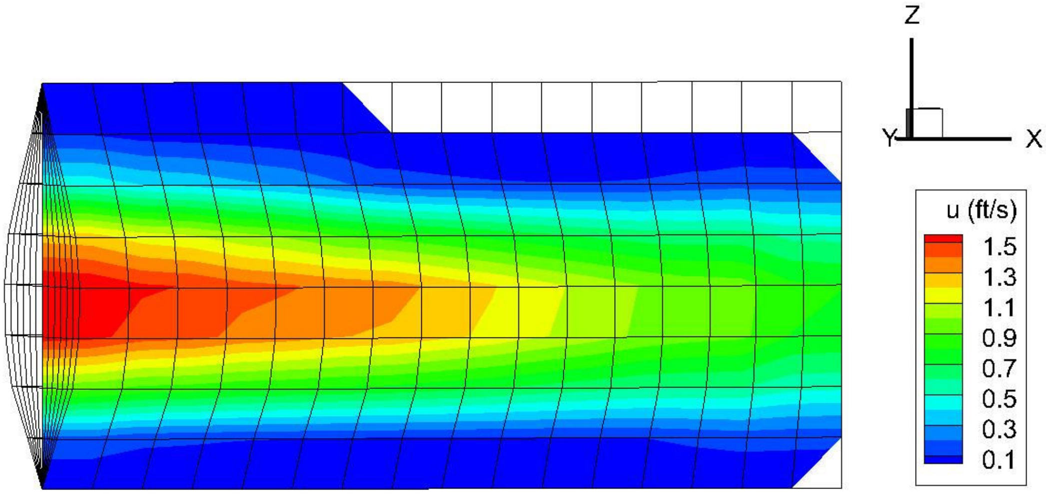

Fig. 4.5—Velocity in the *x*-direction across the fracture height for the gelled acid case at the centerline of the fracture width.

The fracture *x*-direction velocity is highest near the fracture inlet. The flow rate through the fracture is the largest at this location and reduces as fluid leaks into the surrounding formation along the length and height of the fracture. Even though the fracture leakoff is set to equal approximately the pump rate into the fracture (zero efficiency), hydraulic fracture leakoff decreases with the square root of time so the initial leakoff flow rate decreases slightly over the treatment time. Flow out the fracture tip in the *x*-direction is therefore necessary for code stability. Without this admittance the pressure oscillates and builds, failing to converge to resolve the velocity fields in the fracture. Allowing the flow to exit out the ends of the fracture in the *x*-direction creates some fluid movement in the *z*-direction (Fig. 4.6).

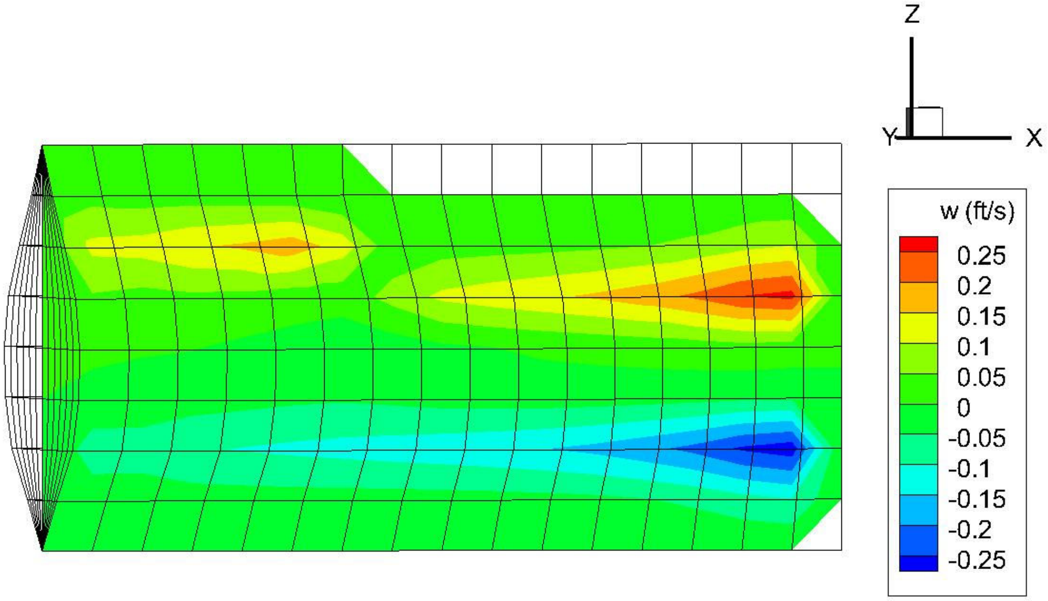

Fig. 4.6—Velocity in the *z*-direction across fracture height for the gelled acid case at the centerline of the fracture width.

The *z*-direction velocity occurs as fluid is lost out the fracture tip and as the fracture width diminishes. Fluid is allowed to leak out of the fracture in the *x*-direction everywhere the width goes to zero. The fluid in the fracture then tends to replace the fluid that is lost and some movement in the vertical direction occurs. The fluid movement across the fracture height is nonsymmetrical, because the initial fracture shape is nonsymmetrical. Fluid is lost unevenly from the fracture so that the movement of fluid in the vertical direction varies throughout. Additionally, the fracture width decreases more severely at the vertical centerline in the fracture length direction. This compression of the width in the middle of the fracture also forces some fluid to move vertically toward the top and bottom portions of the fracture.

Most of the fluid in the fracture is lost as leakoff out the sides of the fracture (Fig. 4.7).

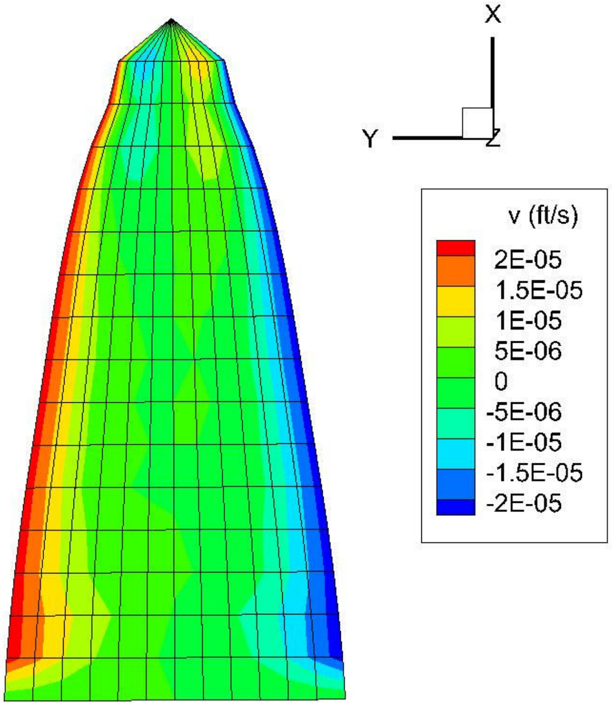

Fig. 4.7—Velocity in the *y*-direction across fracture width for the gelled acid case at the vertical centerline.

Initially, the leakoff is calculated by the model to be what is specified in the geometry input file for fluid efficiency, using the fluid efficiency to calculate what portion of the inlet flow rate leaks out the fracture walls. This leakoff then follows a Carter type coefficient where the leakoff is dependent on the square root of pump time (Penny and Conway, 1989). The hydraulic fracture leakoff condition continues until the acid at the fracture surface reaches an acid concentration that is 0.1 kg-mole/m^3. Past this point in time the leakoff criterion switches to an acid fracture leakoff that is defined by Hill et al. (1995) where the pore volumes to breakthrough of the formation is used to accelerate the leakoff and reflect the presence of wormholes created by the acid. The leakoff velocity is higher toward the fracture inlet as opposed to the fracture tip, which reflects the acid fracture leakoff criterion. The *y*-direction velocity has components near the fracture tip that are opposite to the direction of the leakoff at the fracture walls. This is because the fluid flow near the fracture tip diverges with most of the flow leaking out the fracture walls and a small portion flowing out the fracture tip (about 0.8%). This divergence of flow at the fracture tip is depicted in Fig. 4.8.

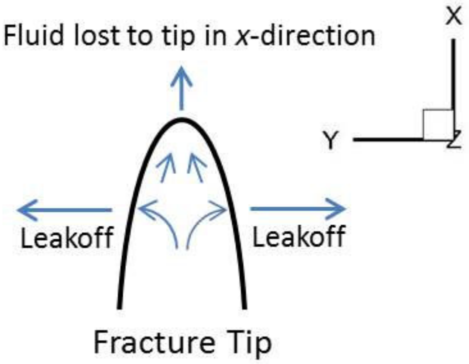

Fig. 4.8—Depiction of flow divergence at the fracture tip in the *x*- and *y*-directions.

The fracture leakoff, width, and the effective diffusion coefficient determine the Peclet number, which characterizes the penetration of the acid in the fracture (Fig. 4.9).

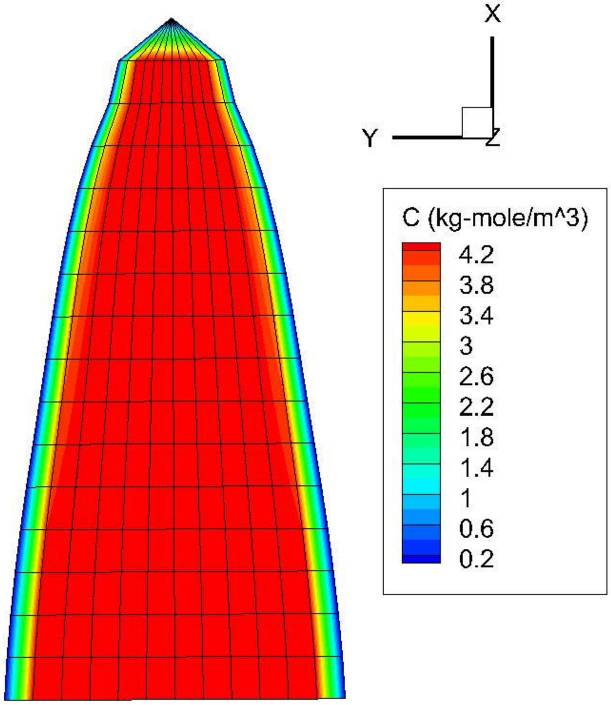

Fig. 4.9—Acid concentration across fracture width for the gelled acid case at the vertical centerline.

The acid reaches the tip of the fracture at near its full strength. The initial Peclet number for this example is approximately 18 using an average initial fracture width and leakoff, so acid should reach the very end of the fracture close to the inlet concentration. This is demonstrated to occur by Figure 4.10.

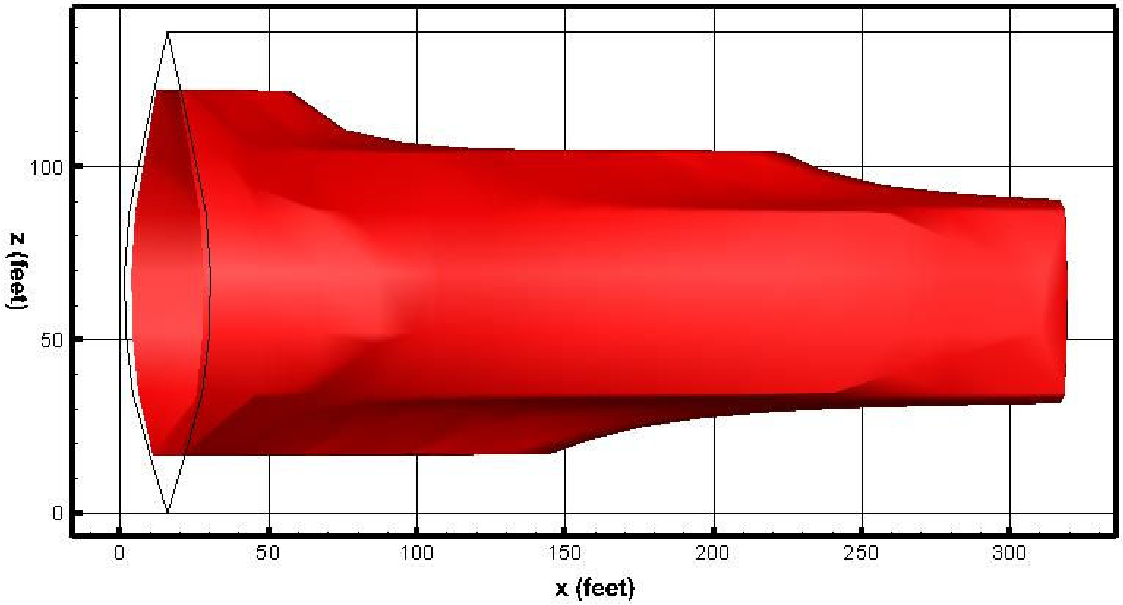

Fig. 4.10—Isosurface demonstrating penetration of 95% inlet strength acid concentration for the gelled acid case.

High concentrations of acid reach the full extent of the fracture for this case, so the acid-etched width must also be distributed across the fracture length and height. This is revealed to occur by Figure 4.11.

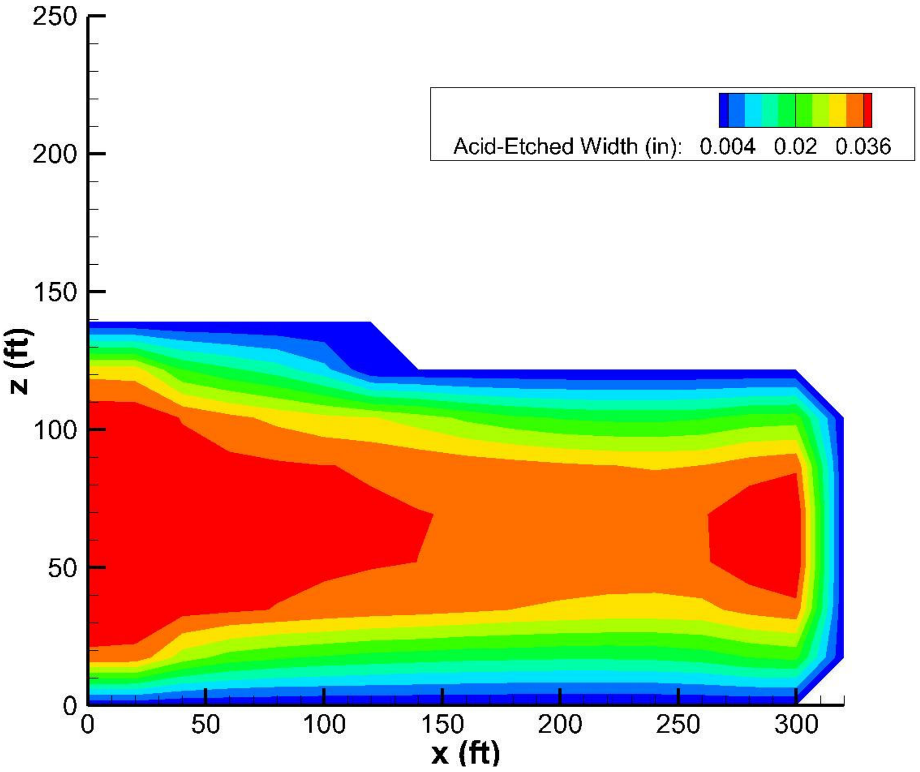

Fig. 4.11—Acid-etched width for the gelled acid case.

The acid-etched width is distributed almost uniformly across the fracture length, and this arrangement of acid-etched width is supported by the analytical expressions for the acid concentration and the etched width in a parallel plate domain. The differences from the analytical solution are because of the non-uniform, initial fracture width. The fracture narrows toward the fracture tip in the *x*-direction. The narrower width at the tip enables more acid to diffuse to the fracture surface and create etching during the treatment. Thus, more acid-etched width is observed in this region of the fracture.

The conductivity follows the pattern of acid-etched width across the fracture (Fig. 4.12).

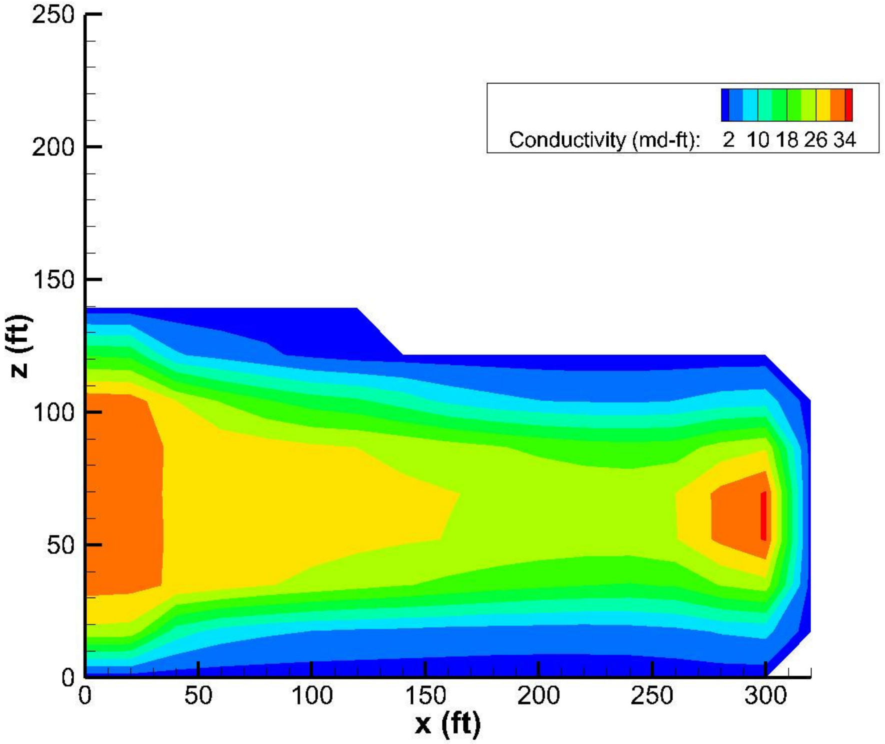

Fig. 4.12—Mou-Deng conductivity after closure for the gelled acid case.

Geostatistical parameters typical of a layered carbonate reservoir are used to calculate the Mou-Deng conductivity $\left(\lambda_{D,x} = 1, \lambda_{D,z} = 0.05, \sigma_D = 0.4\right)$ (Oeth et al., 2011). The conductivity is generated over the entire extent of the fracture and reaches the fracture tip. The higher conductivity at the fracture tip is due to the smaller width, which enables diffusion of the acid to create etching and conductivity. The high conductivity near the fracture entrance is because of the relatively high concentration of acid entering the fracture. At the end of the treatment any acid still in the fracture is assumed to create etching at the ratio of the user specified fraction of acid to react on the fracture surface before becoming leakoff ($f_r = 0.3$ for this case, which is supported via experimental comparison by Mou (2009)). This generates additional conductivity everywhere along the fracture but mostly where the fracture is the widest as the largest amount of acid is there to create additional etching. This counteracts the effect of narrower width generating the majority of the etching.

4.2.2 Weakly Gelled Acid Treatment Example

The same treatment parameters as were used previously are input to the acid model, except that the gel characteristics of the acid are weaker (Table 4.2).

Table 4.2—Updated parameters to reflect weakly gelled acid fluids.

Effective Diffusion Coefficient	8×10^{-5} cm^2/s
Power Law Index	0.85
Consistency Index	0.01 $Pa\text{-}s^n$

Laboratory data by collected by various researchers demonstrate that diffusion can increase by multiple orders of magnitude for straight acids as compared to gelled acid fluids (Roberts and Guin, 1974; de Rozieres et al., 1994; Conway et al., 1999). Therefore, the diffusion is increased by one order of magnitude to model a fluid that is only weakly gelled. The figures presented in this section are captured at the end of the acid fracture treatment. The fluid flow characteristics of the treatment are very similar to the gelled acid case but the pressure gradient is smaller to push the less viscous fluid through the wider fracture (Fig. 4.13).

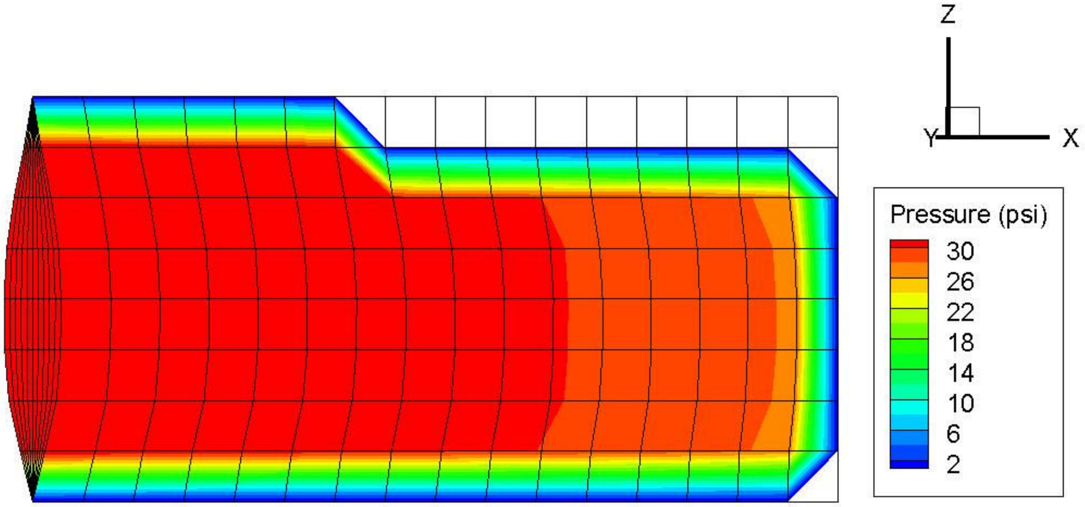

Fig. 4.13—Pressure across the fracture for the weakly gelled acid case.

The pressure required to move fluid across the fracture is lower for this weakly gelled acid case than for that of the previous gelled acid case. This is in part due to the additional acid-etched width generated during the treatment because of the higher effective diffusion. The additional width from acid etching reduces the resistance to the fluid moving through the constricting fracture.

The lower pressures are also because of the lower consistency index, which creates a lower apparent viscosity. The maximum apparent viscosity still occurs at the center of the fracture where the shear is the lowest, and the limit of 10 cp is reached at this location (Fig. 4.14). The lower apparent viscosity cutoff of 1 cp is not used in this simulation. The Reynolds number for this case is 533 and is larger than that of the gelled acid case mainly due to the slightly decreased viscosity throughout the fracture.

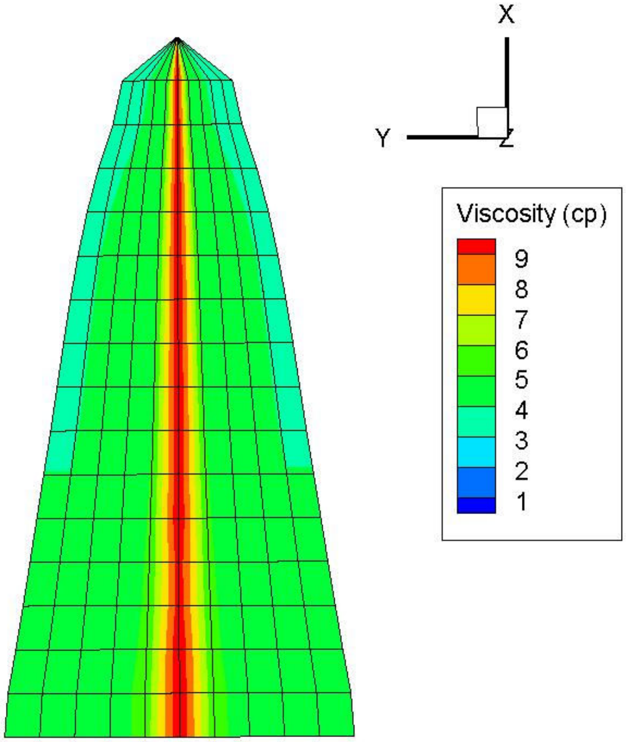

Fig. 4.14—Apparent viscosity across the fracture width for the weakly gelled acid case at the vertical centerline.

The velocity components appear similar to those for the previously presented gelled acid case. The main difference is that the *x*-direction velocity is slightly lower throughout the fracture due to the increased acid-etched width (Figs. 4.15-4.16).

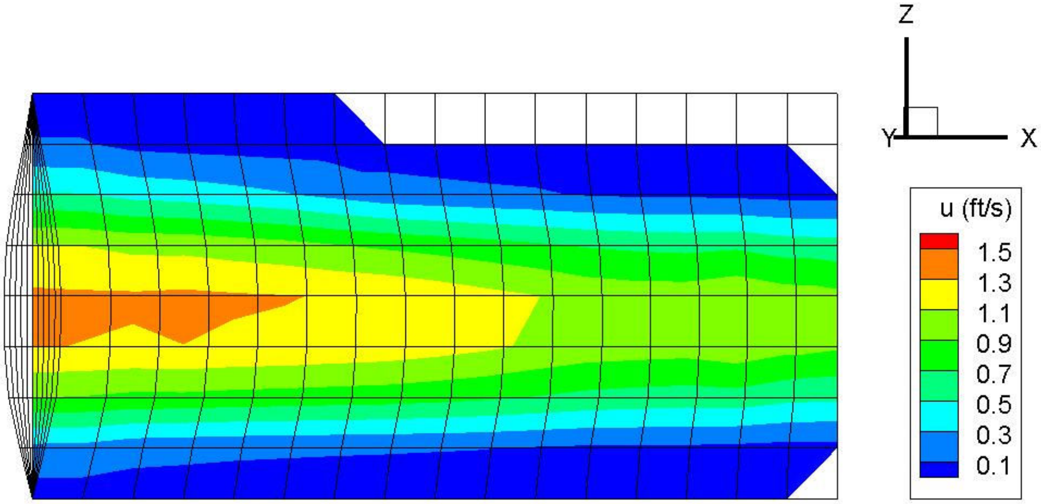

Fig. 4.15—Velocity in the *x*-direction across the fracture height for the weakly gelled acid case at the centerline of the fracture width.

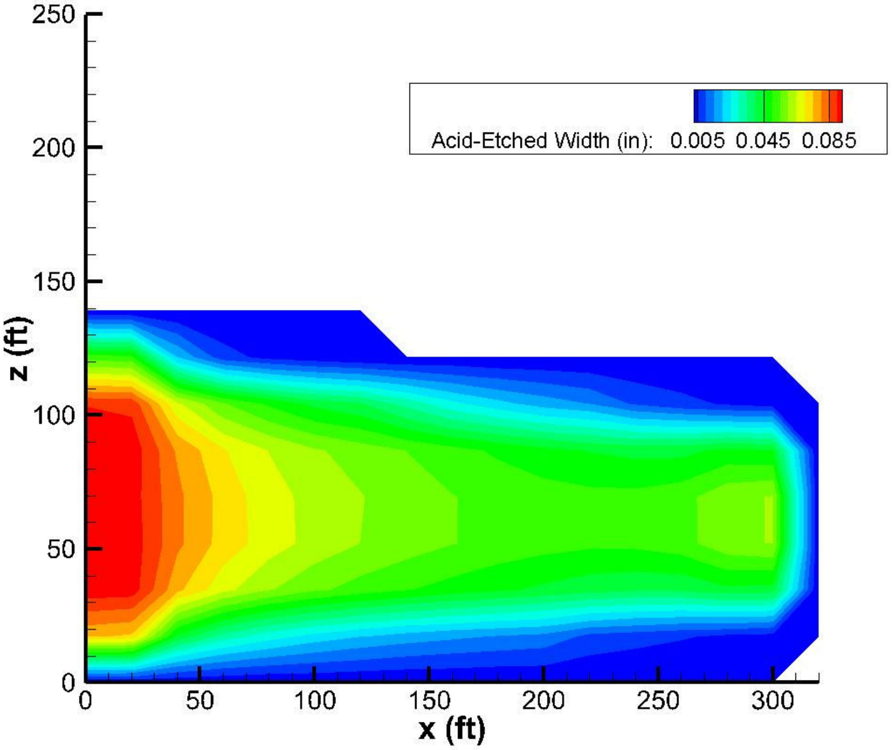

Fig. 4.16—Acid-etched width for the weakly gelled acid case.

Additional etching near the fracture inlet increases the fracture width there, which lowers the *x*-direction velocity slightly. Additional acid-etched width near the fracture entrance is expected for a treatment with a lower Peclet number, and the initial Peclet number for this case is 1.8 (compared to 18 for the strongly gelled acid case).

Higher Peclet numbers are characterized as having high concentrations of acid reach the fracture tip. As the Peclet number decreases, the penetration of acid is also expected to decrease. The initial Peclet number for the weakly gelled acid case is an order of magnitude lower than that for the gelled acid. The penetration of near inlet strength acid is substantially diminished in this case. This is shown to occur in Figure 4.17.

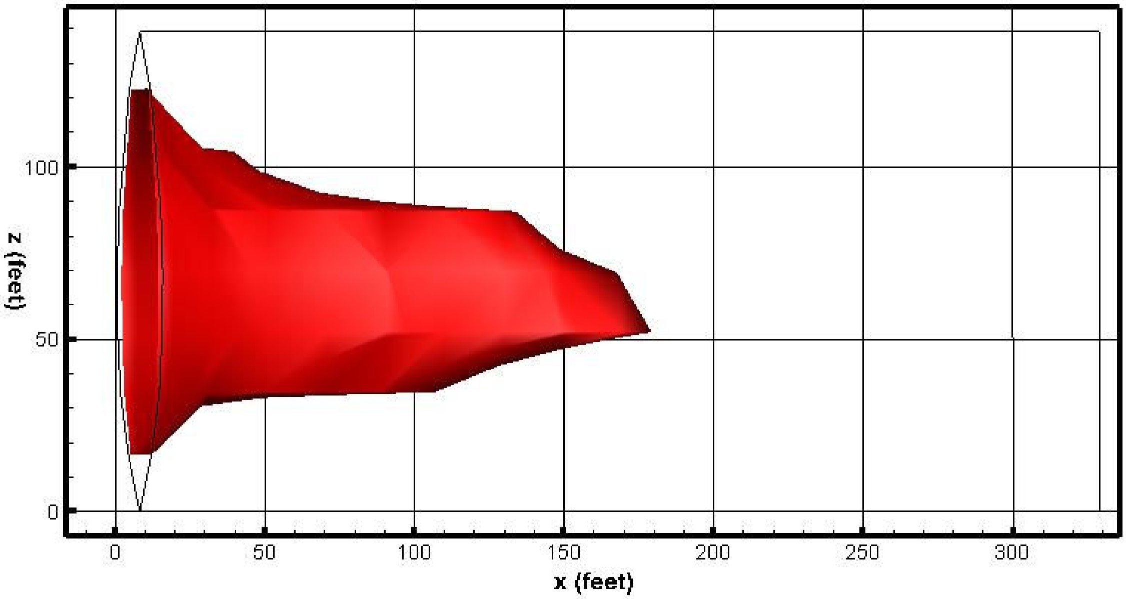

Fig. 4.17—Isosurface demonstrating penetration of 95% inlet strength acid concentration for the weakly gelled acid case.

The acid-etched width at higher Peclet numbers is evenly distributed across the fracture. As the Peclet number decreases, the acid-etched width is biased toward the fracture entrance and diminishes more severely in the direction of the fracture tip. The weakly gelled acid demonstrates this behavior. The higher effective diffusion emphasizes etching at the fracture tip where the width is initially narrower, but the majority of the etching occurs near the fracture entrance. The conductivity follows the pattern of acid-etched width across the fracture and is similarly biased to be highest at the fracture entrance (Fig. 4.18).

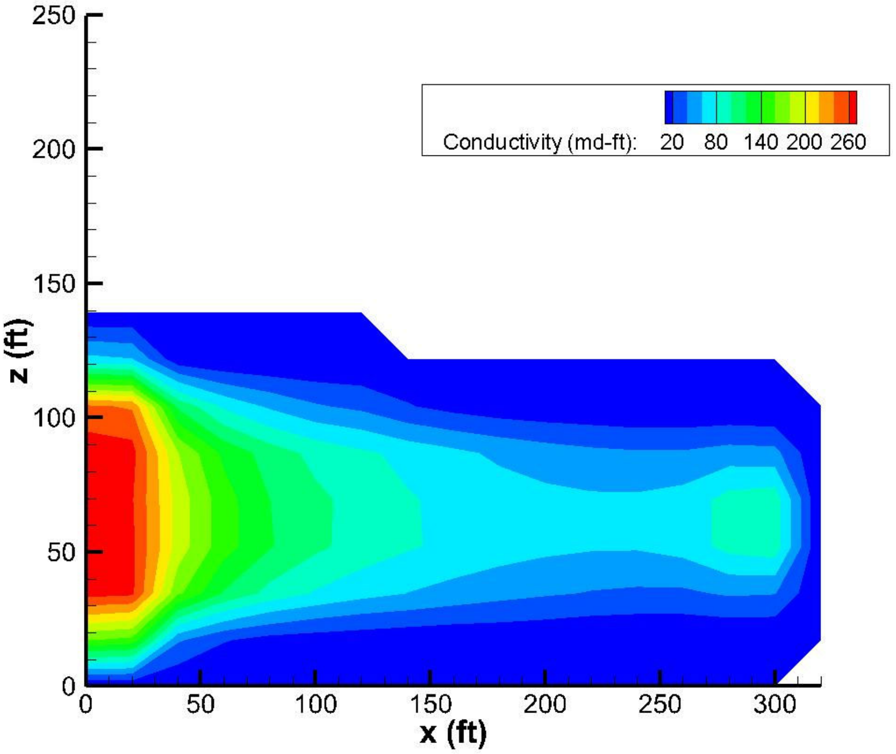

Fig. 4.18—Mou-Deng conductivity after closure for the weakly gelled acid case.

Conductivity is generated across the entire fracture area with the highest conductivity at the fracture entrance. More conductivity is created in the weakly gelled acid case because of the higher effective diffusion of the acid to the fracture surfaces. More acid reaches the fracture surface to create etching and conductivity. The shape of the conductivity across the fracture length with the majority of the conductivity having been generated near the fracture entrance is expected to occur as the Peclet number decreases (initially 18 for the gelled acid case compared to 1.8 for the weakly gelled acid). Overall, the etching and conductivity are less uniform for the weakly gelled acid, which is expected given the higher input effective diffusion.

4.2.3 Straight Acid Treatment Example

The same treatment parameters as were used previously are input to the acid model, except that the fracture fluid viscosity is constant at 1 cp and the effective acid diffusion is increased another order of magnitude (8×10^{-4} cm^2/s) to represent the increased diffusion that occurs with a straight acid (Roberts and Guin, 1974; de Rozieres et al., 1994; Conway et al., 1999). This decreases the initial Peclet number to 0.18 (two orders of magnitude smaller than the gelled acid case). The Reynolds number for this case is 2340 and is larger than the previously presented cases because of the smaller viscosity.

The simulation does not reach the specified treatment time in this case, because the simulation cannot resolve the velocity and pressure fields throughout the fracture. The model terminates because the leakoff is significantly smaller than the inflow pump rate (17.3 BPM of leakoff versus the user input flow rate of 20 BPM) as not enough acid is actually in the fracture to initiate sufficient acid fracture leakoff to match the inflow pump rate. The model allows the acid fluid to flow out of the fracture tip in the *x*-direction, but the tip is narrow and higher pressure is required to push the fluid out through the fracture tip. Conversely, the fracture becomes very wide near the entrance due to the large acid concentration, high effective diffusion, and acid fracture leakoff at the entrance, which increase the etched width. The pressure then builds in the fracture to push fluid through the narrow tip, while a lower pressure at the fracture entrance is calculated to match the user specified inlet flow rate. This causes the SIMPLEM algorithm to crash. The model cannot run the entire user specified treatment time for this case because the simulation fails to resolve the velocity and pressure profile throughout the fracture. The model ends after simulating about 14 minutes of the 20 minute treatment.

The large etched width generated in the fracture near the entrance is observed in Figure 4.19.

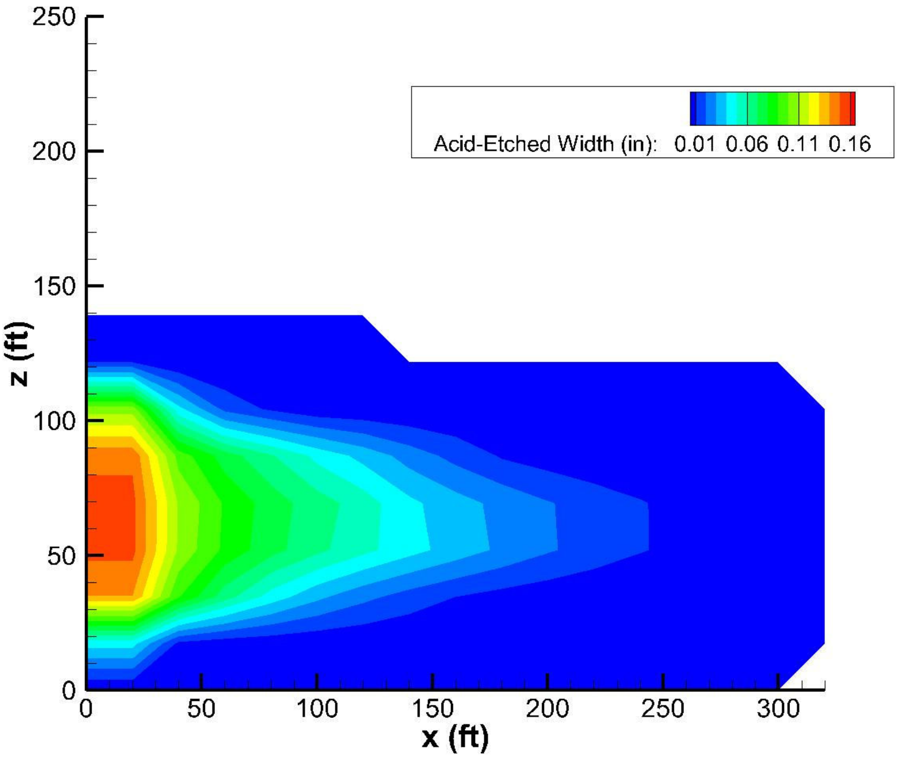

Fig. 4.19—Acid-etched width for the straight acid case.

The leakoff increases near the fracture inlet where the acid immediately spends due to the high effective diffusion. The high effective diffusion causes acid to reach the surface of the fracture and initiate acid fracture leakoff. The increase in leakoff of the acid fluid causes additional etching near the fracture entrance.

Low Peclet number acid fracture treatments have short penetration of the acid into the fracture. The model supports this characterization as high concentrations of acid do not extend into the fracture (Fig. 4.20).

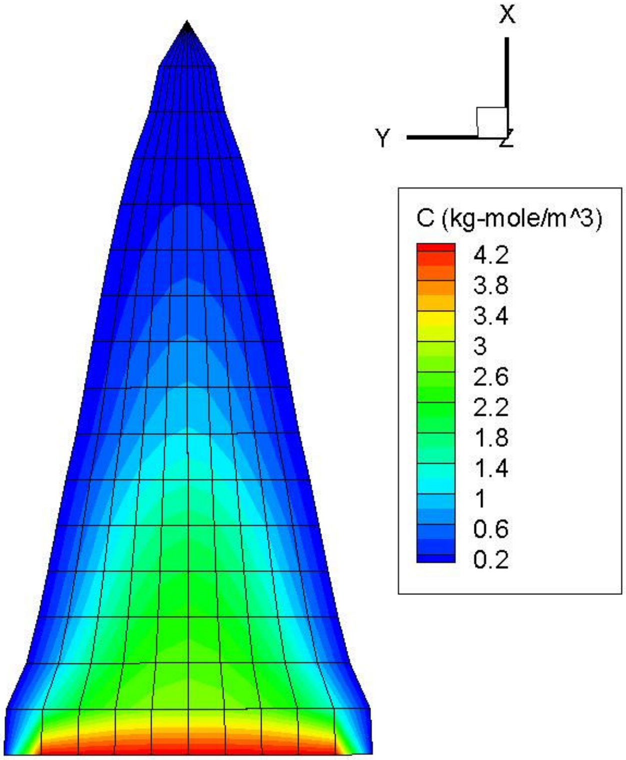

Fig. 4.20—Acid concentration across fracture width for the straight acid case at the vertical centerline.

The effective diffusion is so high for this case that the acid is quickly consumed as it enters the fracture. The concentration gradient along the fracture length is greatly diminished. The low Peclet number supports the acid penetration output from the model for the straight acid case. Correspondingly, the conductivity is also severely diminished along the fracture length (Fig. 4.21).

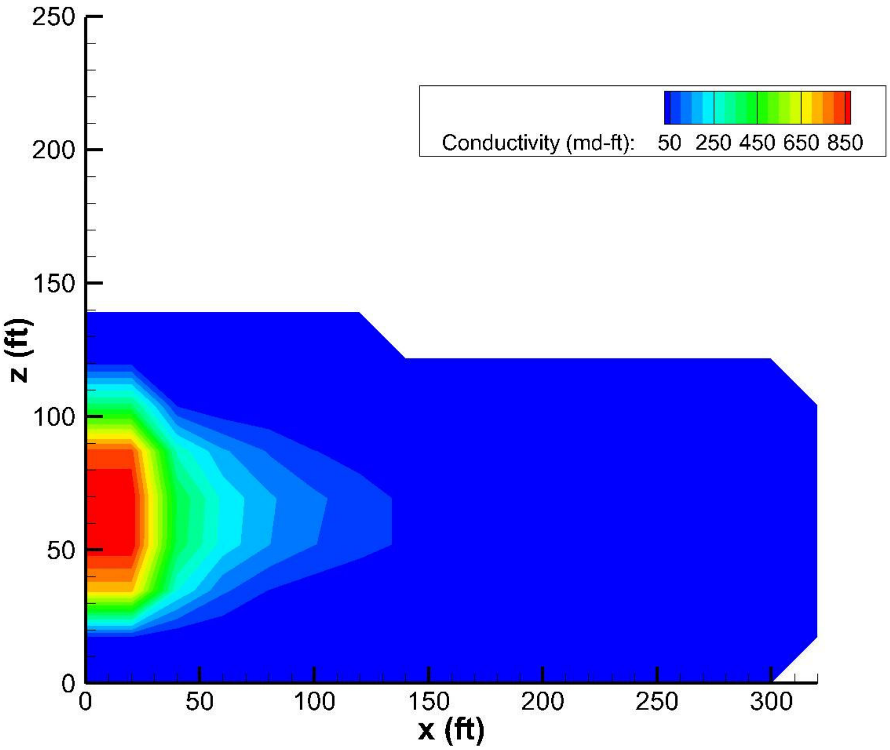

Fig. 4.21—Conductivity after closure for the straight acid case.

The majority of the conductivity is generated near the fracture entrance, because of the high effective diffusion. The high effective diffusion also causes the acid fracture leakoff, which accelerates the etching. This is a common problem in acid fracture treatments with numerous diffusion and leakoff control measures having been developed to extend etching along the fracture (Gdanski, 2005).

4.3 Dolomite Mineralogy

4.3.1 Gelled Acid Treatment Example

The 15% by weight hydrochloric acid has roughly 86.6% the dissolving power with dolomite as compared to limestone (Schechter, 1992). The same input data for the previously presented cases should therefore produce similar etching and output conductivity profiles for the same fracture geometry if the mineralogy is uniformly dolomite. The gelled acid case output for a uniform dolomite mineralogy is presented in Figures 4.22-4.23.

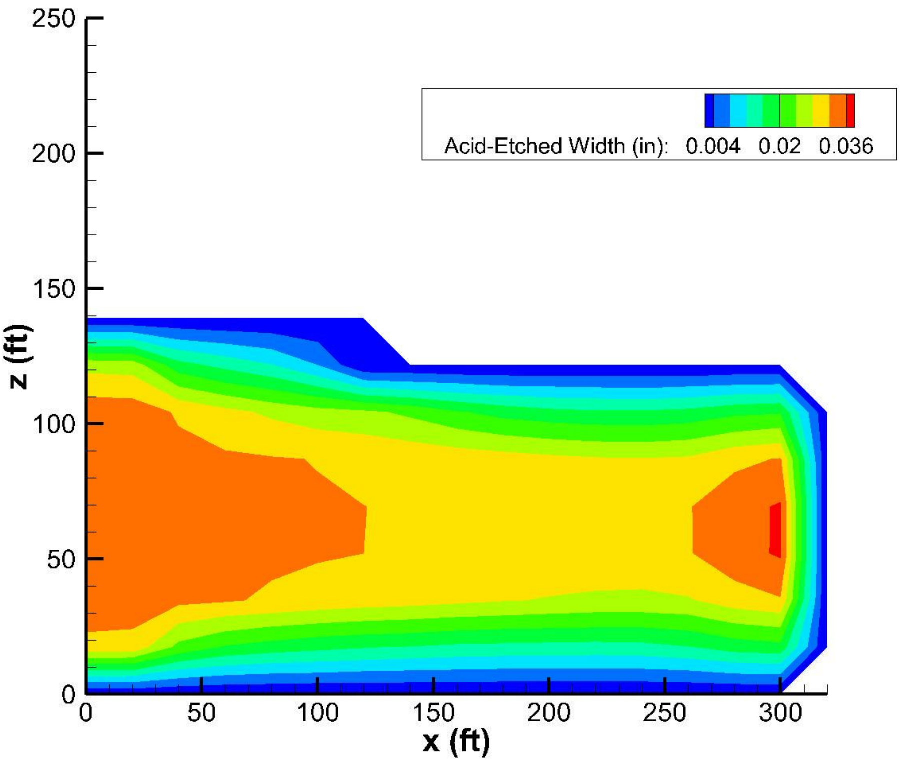

Fig. 4.22—Acid-etched width for the dolomite gelled acid case.

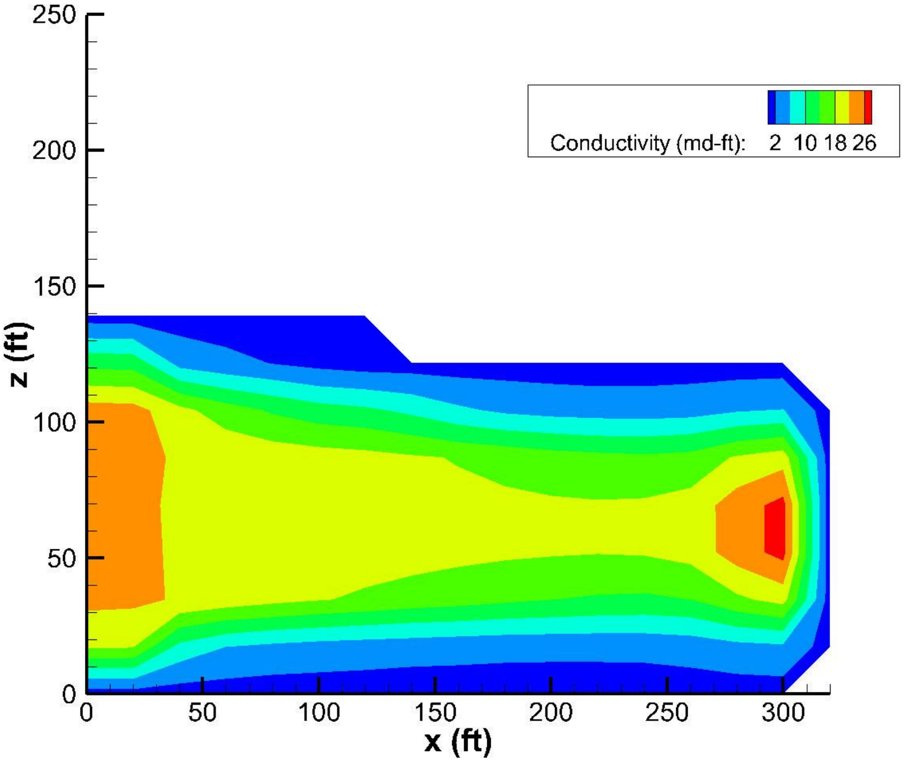

Fig. 4.23—Conductivity after closure for the dolomite gelled acid case.

The average acid-etched width for this dolomite case is 86.7% of that for the uniformly limestone case. The pattern of acid-etched and conductivity along the fracture is identical to that of the limestone case, but the etched width everywhere is slightly lower overall.

4.3.2 Nonzero Fluid Efficiency

Dolomite formations are occasionally tighter than conventional limestone formations. The fracture efficiency can be changed by the user in the geometry file to reflect lower leakoff values during the acid injection stage. The output acid-etched width for a fracture efficiency of 0.5 and the gelled acid fluid is presented in Figure 4.24.

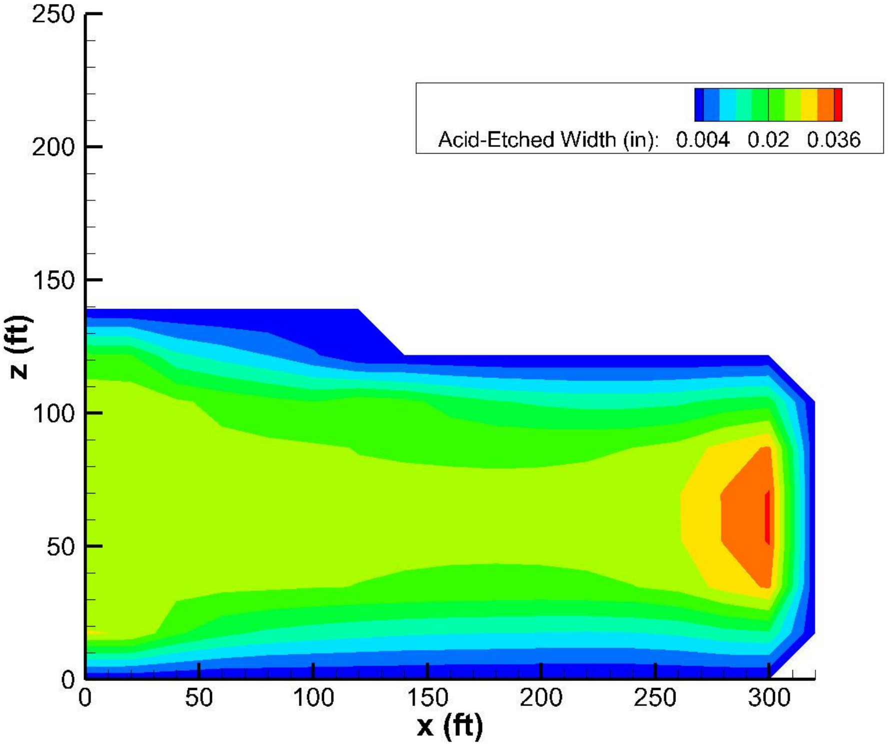

Fig. 4.24—Acid-etched width for the dolomite gelled acid case with 0.5 fluid efficiency.

The acid-etched width is slightly lower overall throughout the fracture compared to the zero efficiency case. Cases with higher efficiency have lower leakoff, so less acid is moved to the walls of the fracture to react and create etching. The etching is also more pronounced toward the fracture tip. This is due to less acid being lost as leakoff, which supports higher concentrations of acid reaching the fracture tip (compared to the acid concentration near the fracture tip for the zero efficiency case). Additionally, in cases where the fluid efficiency is not zero, the acid concentration along with the fluid is allowed to leak out the fracture tip. More fluid moving through the narrow fracture tip enables higher concentrations of acid to reach the fracture tip compared to the zero efficiency case. These features of the simulation cause the acid concentration to be maintained in the fracture *x*-direction and not diminish as much compared to the zero efficiency case. The unevenness of etching (more at the tip relative to that created near the fracture entrance) is then more pronounced for this case than for the higher leakoff case. This is reflected in the output conductivity (Fig. 4.25).

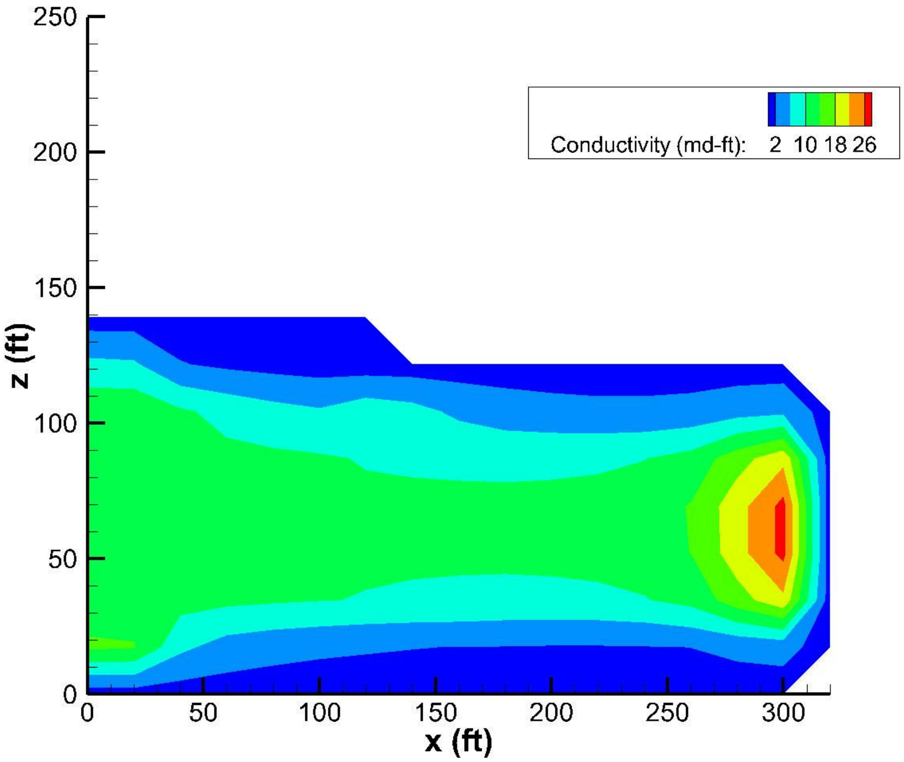

Fig. 4.25—Conductivity after closure for the dolomite gelled acid case with 0.5 fluid efficiency.

The conductivity is lower across the fracture for the case with higher fluid efficiency compared to the zero efficiency case. Lower leakoff and faster moving fluid in the *x*-direction help to move the acid across the fracture length and support high concentrations of acid along the fracture length. In reality, fluid efficiencies greater than zero indicate that the fracture is still growing, but the model does not capture the stimulation benefit from the acid that moves beyond the initial user input fracture geometry. The model accepts one input geometry at the beginning of each simulation, so the most realistic model predictions occur for a zero efficiency fracture.

4.3.3 Increased Temperature

Dolomite has a reaction rate constant that is two orders of magnitude smaller than that for limestone, and this constant has Arrhenius-type temperature dependency (Economides et al., 1994; Li et al., 1993). Increasing the input temperature therefore increases the reaction rate constant and the reaction at the walls of the fracture. The effective diffusion also increases with temperature (Conway et al., 1999). Simulations were run with input temperatures ranging from 50˚F to 200˚F for both dolomite and limestone mineralogy, and the results were the same as those presented for the gelled acid cases (for that effective diffusion coefficient and fluid system).

In reality, the effective diffusion would change with the input temperature. At present, the model accepts one user input temperature to adjust the acid reaction rate at the fracture walls. The effective diffusion that is supplied by the user should correspond to that user input temperature. As has been demonstrated, the effective diffusion is a critical parameter that determines how the acid spends in the fracture and what conductivity results from the acid injection. The input effective diffusion must reflect the dominant temperature throughout the fracture.

4.4 Acid Volume

The volume of acid contacting the fracture can be changed a number of ways with the model: pump rate, acid volume to be injected, injection time, acid concentration, and the fraction of acid to react on the surfaces before leaking into the surrounding formation. This section investigates how the acid concentration and pump rate affect the etching for the gelled acid case.

The acid concentration is increased to 28% by weight for the HCl gelled acid case with limestone mineralogy and zero efficiency. The acid-etched width for the higher acid concentration is presented in Figure 4.26.

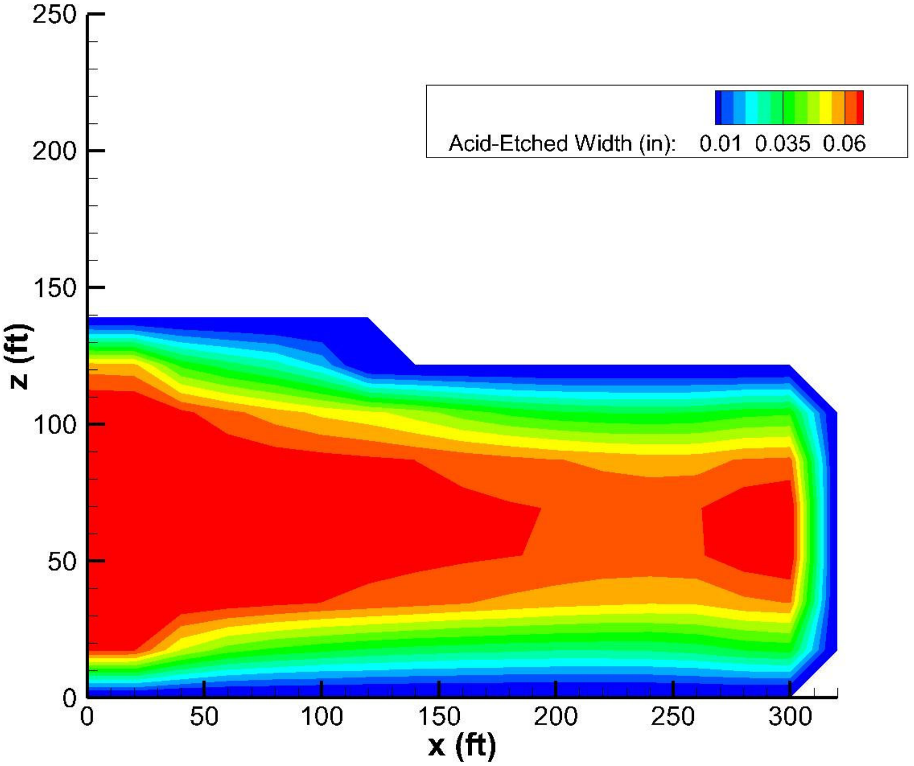

Fig. 4.26—Acid-etched width for the gelled acid, limestone case with 28% by wt. HCl.

The 28% by weight HCl case has 1.87 times the acid mass entering the fracture compared to the 15% by weight HCl gelled acid case, and the average acid-etched width for this case is 1.84 times that of the 15% by weight HCl case. The conductivity is about 4.4 times that of the lower acid concentration case (Fig. 4.27). The acid-etched width is related to the conductivity by a power of 2.49, so the conductivity is within 3% of that predicted based on mass conservation. The shape of the conductivity and acid-etched width profiles remain unchanged assuming the same effective diffusion coefficient can be used. In reality, the effective diffusion would likely increase by about 10% due to the increase in the acid concentration (Conway et al., 1999).

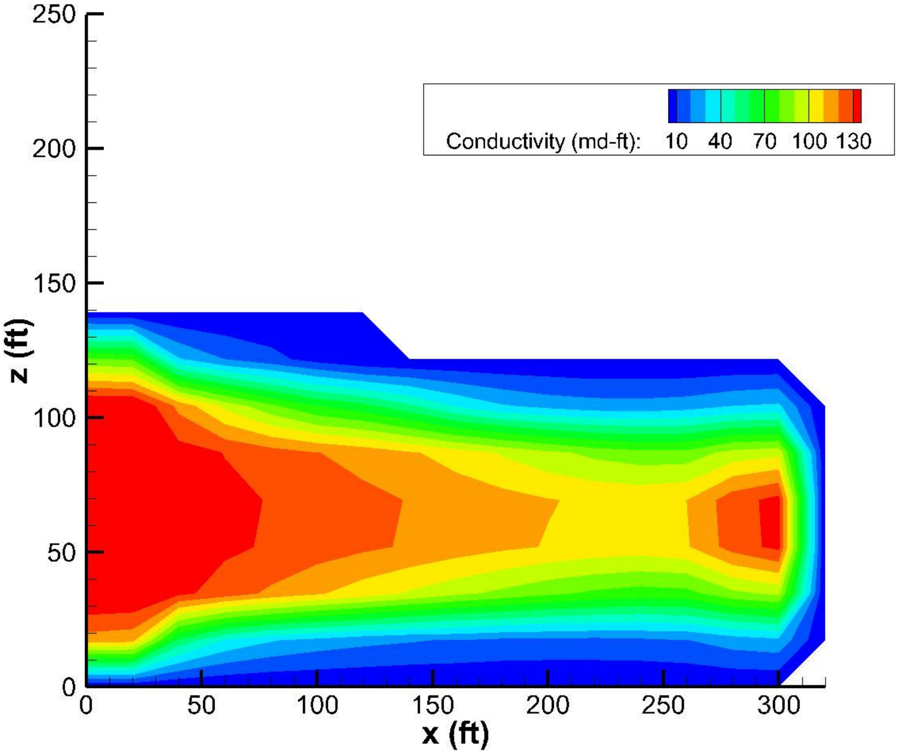

Fig. 4.27—Conductivity after closure for the gelled acid, limestone case with 28% by wt. HCl.

The pump rate is halved for the gelled acid case with limestone mineralogy and zero efficiency. The same volume of pad fluid is pumped to create roughly the same fracture height and length, but the overall fracture surface area is approximately 40% lower than the original confined geometry case. The smaller pump rate also creates slightly smaller initial fracture width. New widths are input to the acid model to investigate the effect of a smaller pump rate on treatment performance (Fig. 4.28).

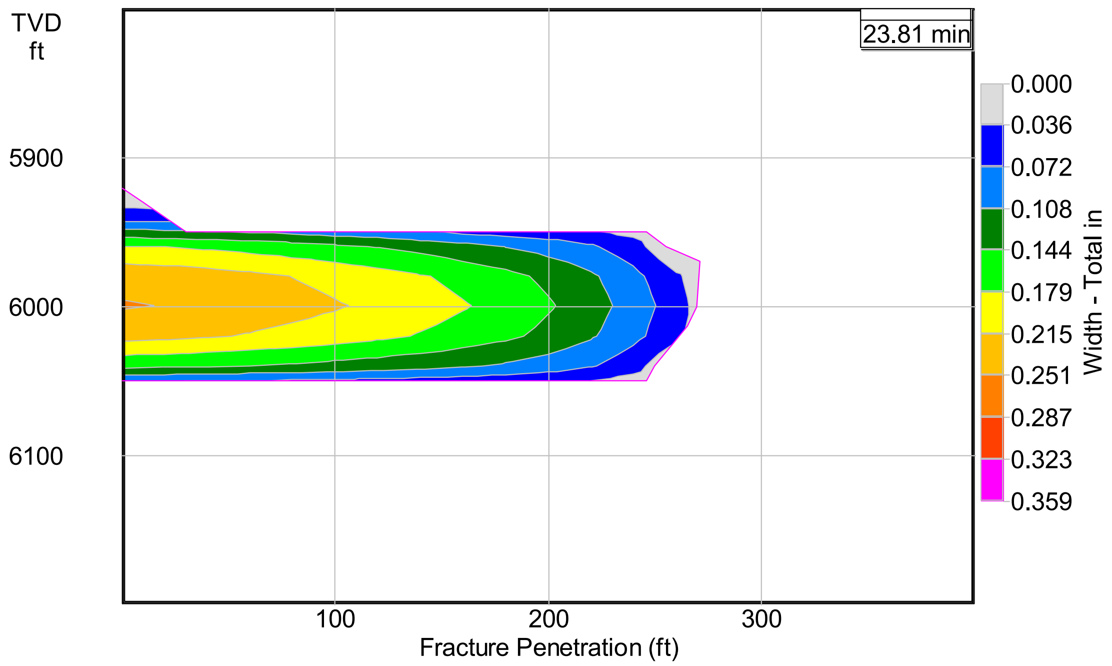

Fig. 4.28—Smaller fracture geometry for the 10 BPM pump rate case.

The smaller initial fracture width encourages diffusion of the acid to the fracture surfaces to create etching, but the leakoff rate is reduced because the pump rate is lower for this zero efficiency fracture. The initial Peclet number for this case is approximately 12. This is a relatively high Peclet number, and the shape of the acid-etched width is similar to that of the original gelled acid case as near inlet strength acid reaches the fracture extent to create etching (Fig. 4.29).

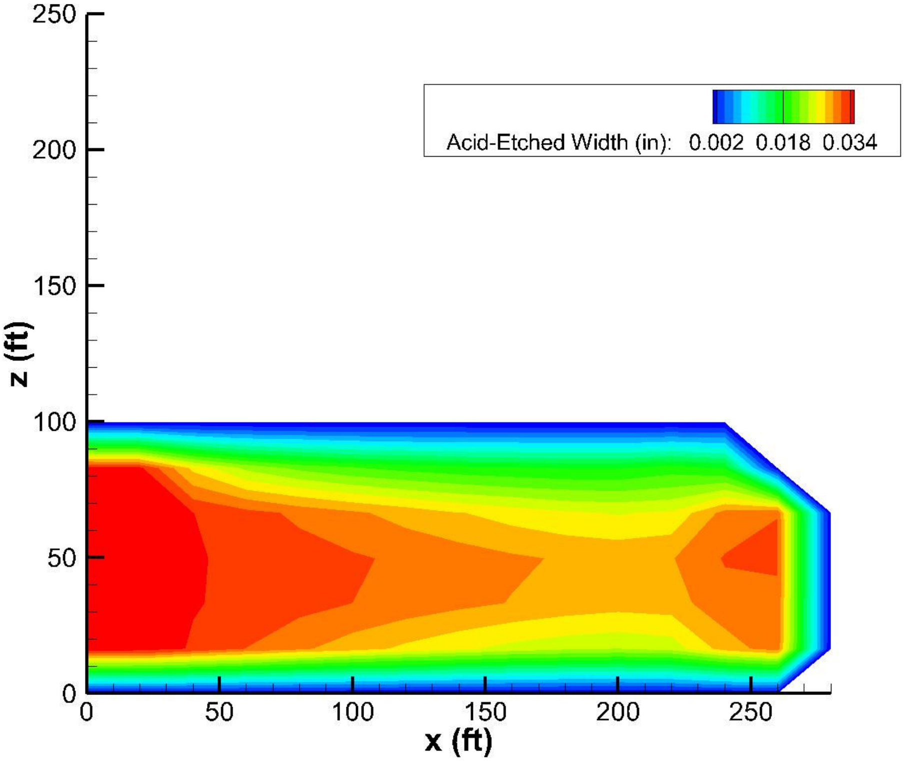

Fig. 4.29—Acid-etched width for the 10 BPM pump rate case.

Acid is distributed almost evenly across the fracture length and height, so the slightly smaller initial width enables acid diffusion to produce etching everywhere. However, the acid transport is reduced because of the smaller leakoff across the fracture. The competing effects between the lower leakoff and narrower fracture width with smaller fracture area create acid-etched width values that are similar to the original gelled acid case. The conductivity for the lower pump rate case is also similar in magnitude and shape compared to the originally presented gelled acid case (Fig. 4.30). Despite the smaller fracture area, the overall conductivity is slightly lower than that of the first gelled acid case because of the lower fracture leakoff.

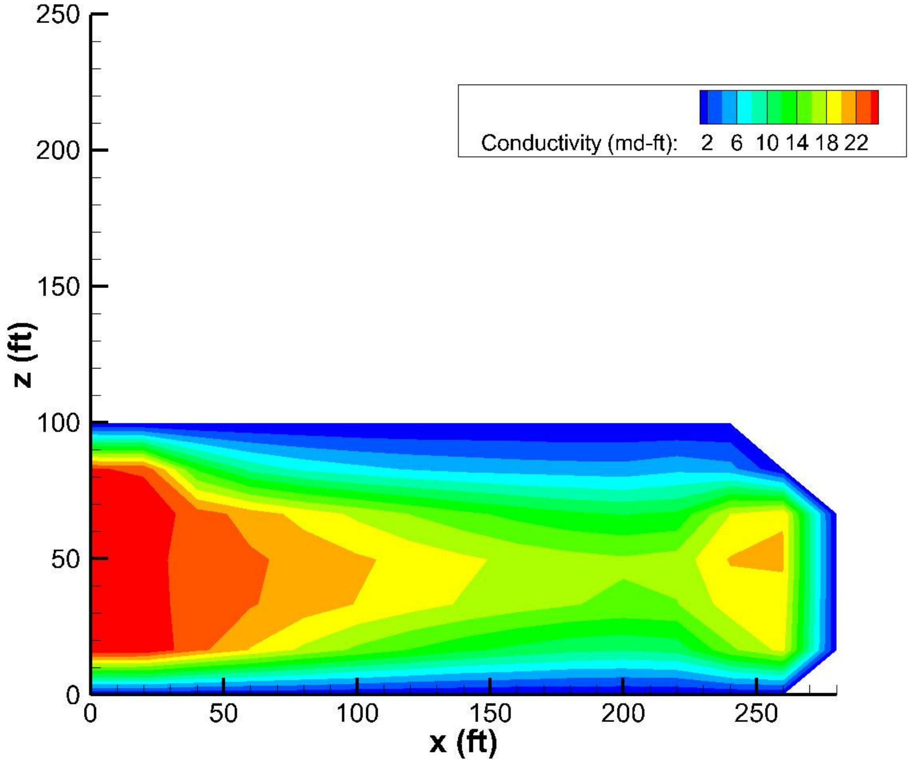

Fig. 4.30—Conductivity for the 10 BPM pump rate case.

4.5 Geologic Layering

The model accepts mixed geology. The model reads in the mineralogy and permeability per layer from separate input files, similar to how it reads the initial fracture width arrays across the fracture height. The geologic layering is observable from the output reaction rate coefficient; the higher coefficient (red bands) corresponds to limestone, the lower coefficient (blue/green bands) corresponds to dolomite, and zero values (dark blue bands) indicate a nonreactive layer (Fig. 4.31). There are two nonreactive layers at the top of the fracture, two limestone layers at the bottom of the fracture, and two dolomite layers between additional limestone layers in the middle of the fracture.

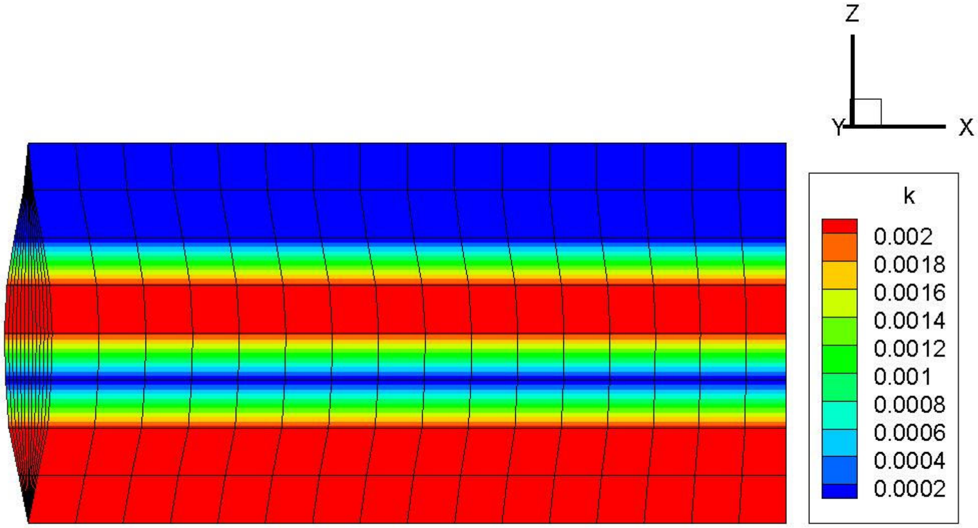

Fig. 4.31—Reaction rate coefficient plot demonstrating mixed geology layers.

The leakoff is also specific to each geologic layer. The total leakoff is equal to the injection rate multiplied by one minus the fracture efficiency $(q_{inj}(1-eff))$, but the permeability input file adjusts the leakoff to reflect what leakoff is going to each layer. The permeability file uses the actual layer permeability to adjust how much of the leakoff goes to each layer based on the Carter leakoff coefficient (Penny and Conway, 1989). The leakoff for the mixed geology case has higher leakoff in the limestone layers (dark blue bands), lower leakoff in the dolomite layers (light blue bands), and the lowest leakoff in the nonreactive layers at the top of the fracture (light green bands) (Fig. 4.32).

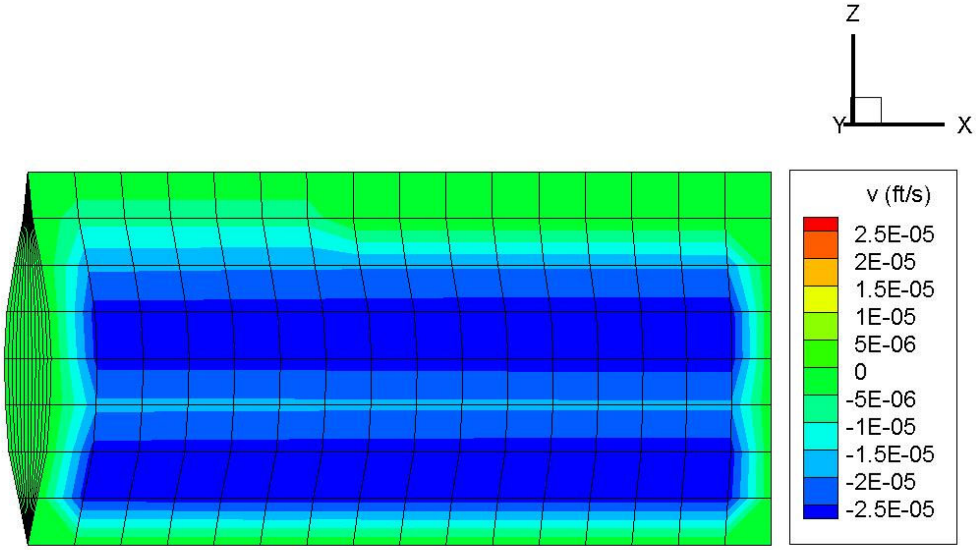

Fig. 4.32—Leakoff velocity across the fracture demonstrating mixed geology layers.

The fracture acid-etched width is arranged to reflect the formation properties in the fracture. The acid-etched width is highest in the limestone layers as these have the larger reaction rate coefficient, more leakoff, and higher dissolving power. These layers have similar values for acid-etched width as the uniform limestone, gelled acid case. Dolomite layers have slightly less acid-etched width and the nonreactive layers have none (Fig. 4.33).

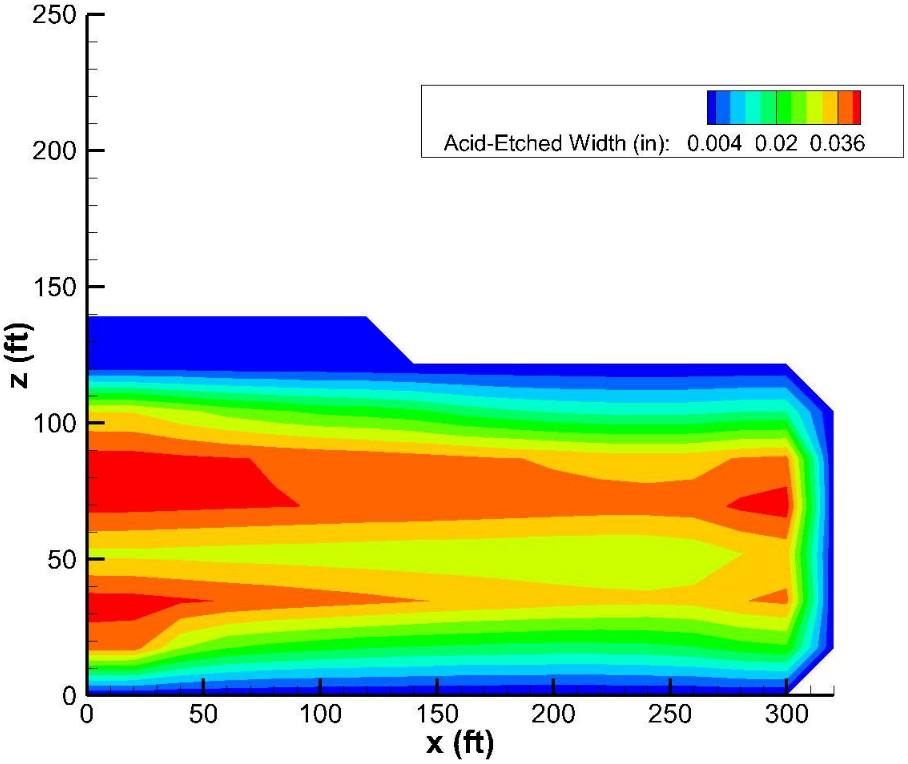

Fig. 4.33—Acid-etched width for the gelled acid, mixed geology case.

The conductivity follows a similar pattern with the largest conductivity in the limestone layers, lower conductivity in the dolomite layers, and no conductivity in the nonreactive layers (Fig. 4.34). Given the mixed geology and slightly lower leakoff, this case follows the competing effects of permeability and mineralogy distributions case using the Mou-Deng conductivity correlations. It has lower conductivity overall than the gelled acid case, which follows the permeability distribution dominant, uniform mineralogy criteria.

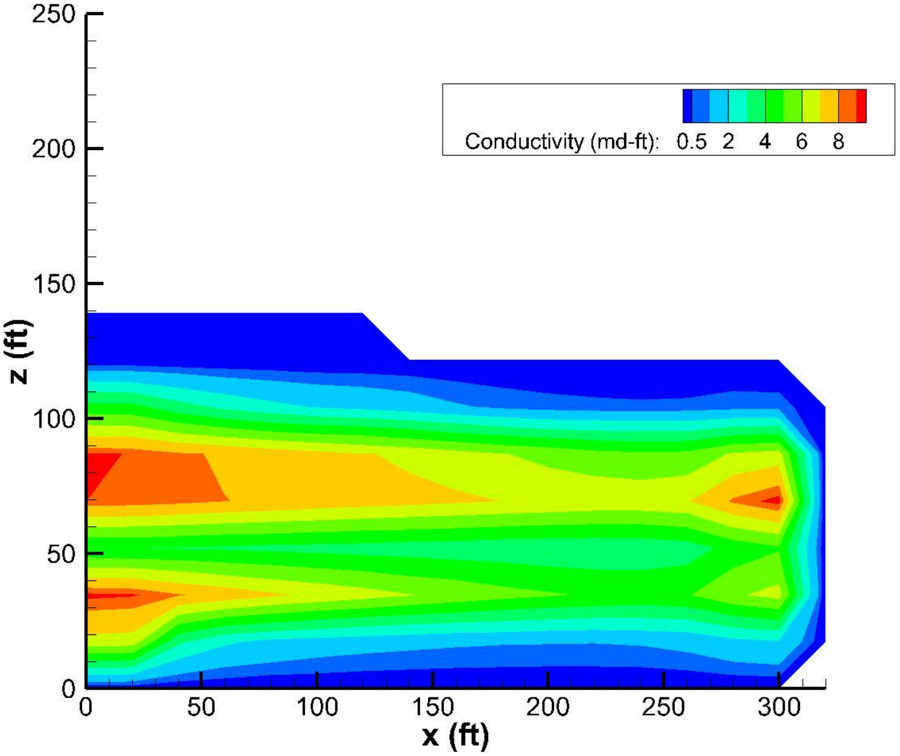

Fig. 4.34—Conductivity after closure for the gelled acid, mixed geology case.

4.6 Completion Effects

The model can be manipulated such that fluid only enters through certain portions of the fracture along its height. This is meant to mimic the entrance conditions when only part of the fracture height is perforated. This section investigates two completion geometries: 20 feet of perforations at the fracture center, and two clusters of 20 foot perforations along the fracture height. The perforation locations will be indicated by arrows in the following figures.

The fluid flow characteristics change when the acid is not permitted to enter the fracture over the entire fracture height. The *x*-direction velocity demonstrates how the flow moves through the fracture for the two completion scenarios (Figs. 4.35-4.36).

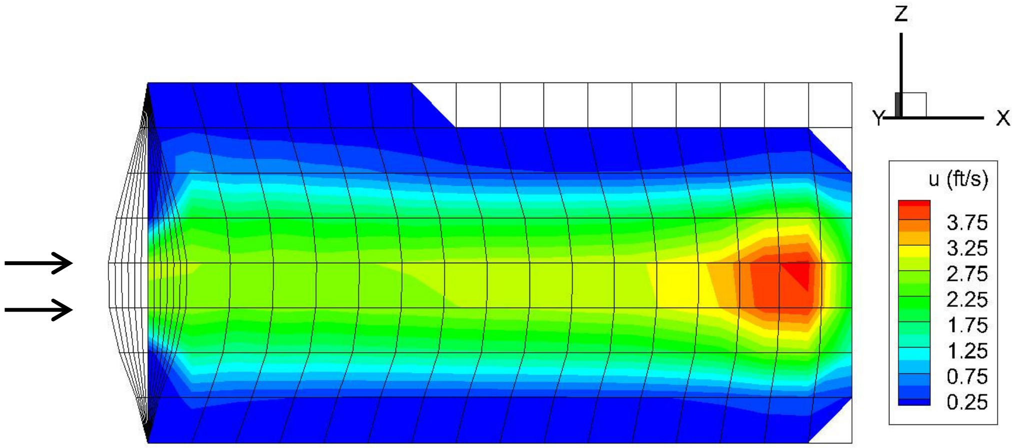

Fig. 4.35—Profile of *x*-direction velocity for the gelled acid case with 20 foot centered perforations.

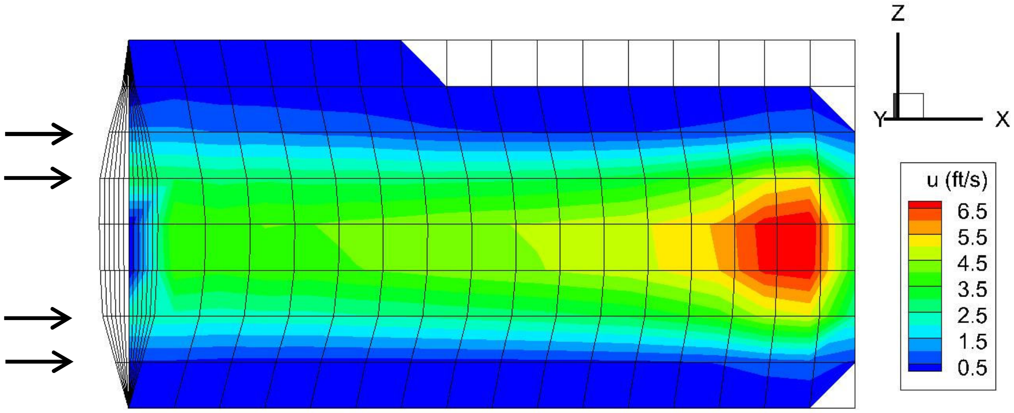

Fig. 4.36—Profile of *x*-direction velocity for the gelled acid case with two 20 foot perforation clusters.

These cases demonstrate how the perforation clusters affect the flow in the fracture. The flow enters at the perforation locations and spreads vertically across the fracture near the entrance. The *x*-direction flow velocity at the simulated fracture perforations is faster than that for the original gelled acid case where the fluid is allowed to enter the fracture over the entire fracture height. The flow merges in the center of the fracture where the width is the widest for the two perforation cluster case. The flow expands slightly in the fracture for the single, centered perforation cluster case. The *x*-direction fluid velocity at the end of the fracture is relatively large and indicates that the majority of the flow is centered in the fracture for both cases. The narrower width near the tip accelerates this concentrated flow.

The acid concentration is the largest in the portions of the fracture with flow movement (Figs. 4.37-4.38).

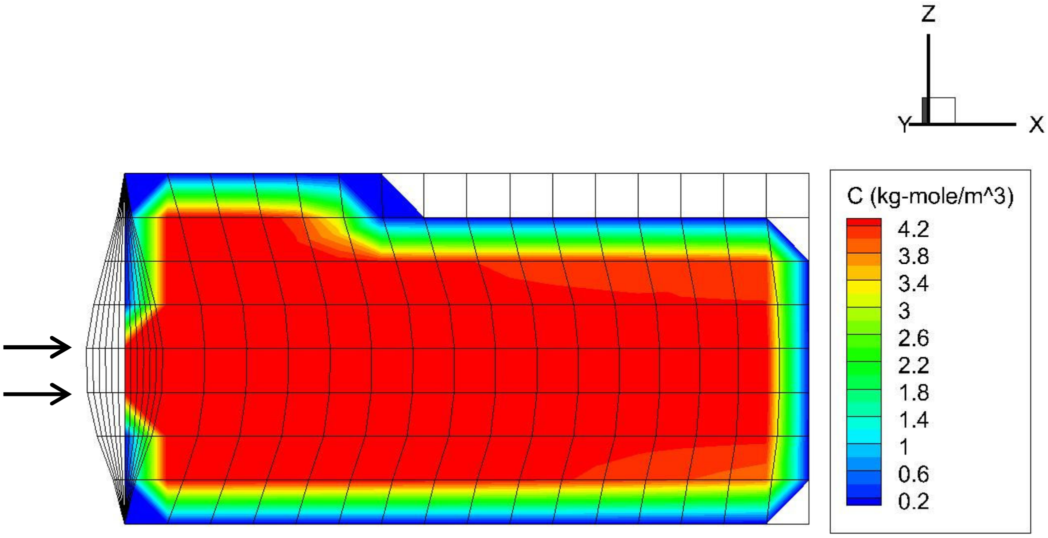

Fig. 4.37—Profile of acid concentration for the gelled acid case with 20 foot centered perforations.

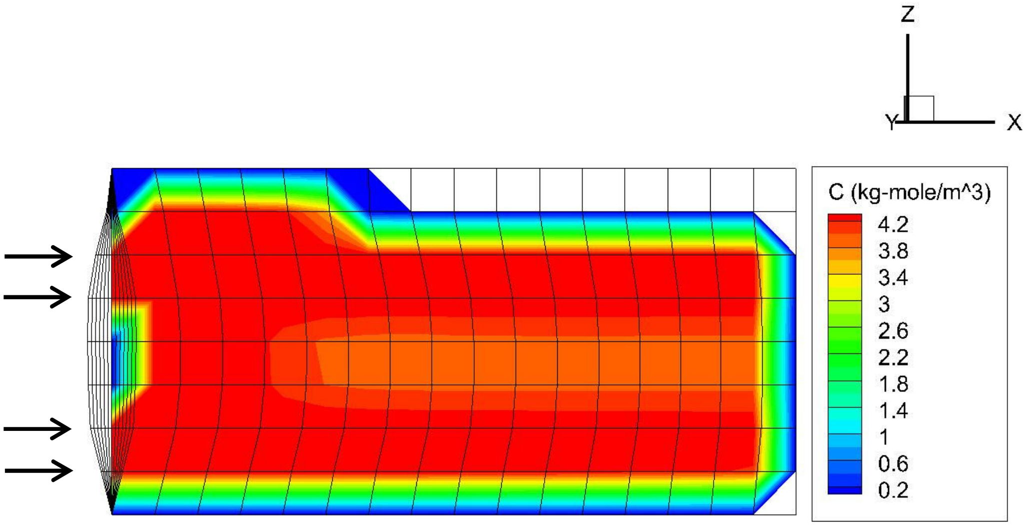

Fig. 4.38—Profile of acid concentration for the gelled acid case with two 20 foot perforation clusters.

The acid penetrates the fracture extent but the highest concentration occurs at the locations along the fracture height where the flow enters. The code has been executed with and without using the effective diffusion coefficient to model diffusion in the vertical or *z*-direction. The effective diffusion is too small to produce any quantitative difference. At the first grid block into the fracture, the flow has moved vertically to push acid across the extent of the fracture height for both completion scenarios. The acid profile through the fracture is then similar to what was originally presented for the gelled acid case (the case assuming dense perforations cover the entire fracture height at the wellbore).

The acid-etched width further demonstrates how the acid concentration is slightly more localized across the fracture than for the densely perforated, gelled acid case presented in Section 4.2.1, but the etching pattern is overall quite similar (Figs. 4.39-4.40).

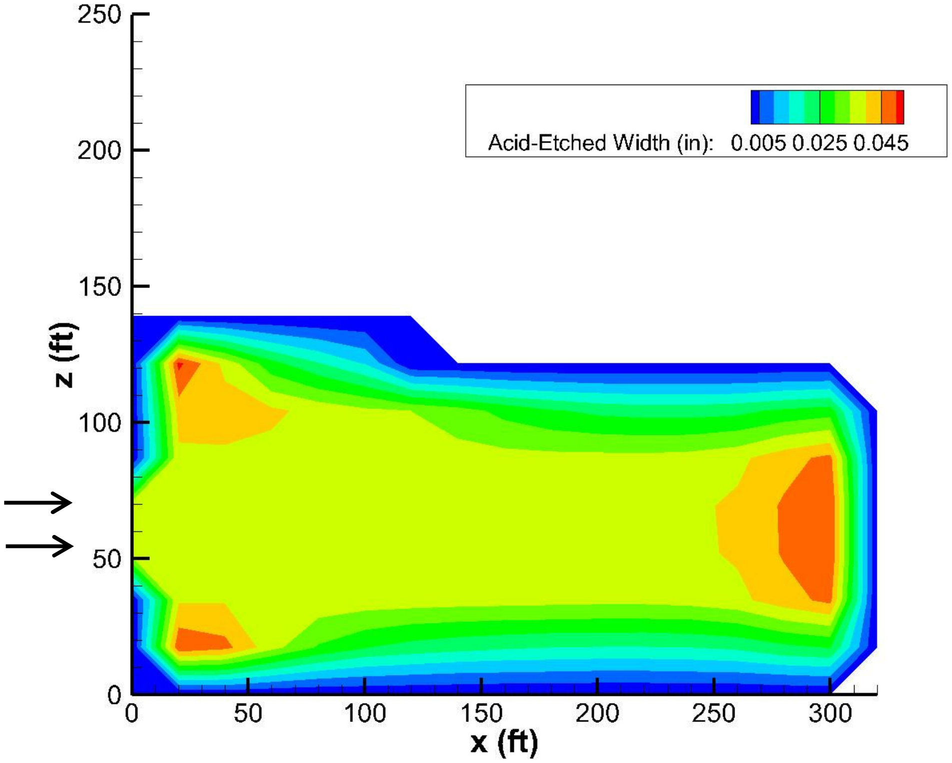

Fig. 4.39—Acid-etched width for the gelled acid case with 20 foot centered perforations.

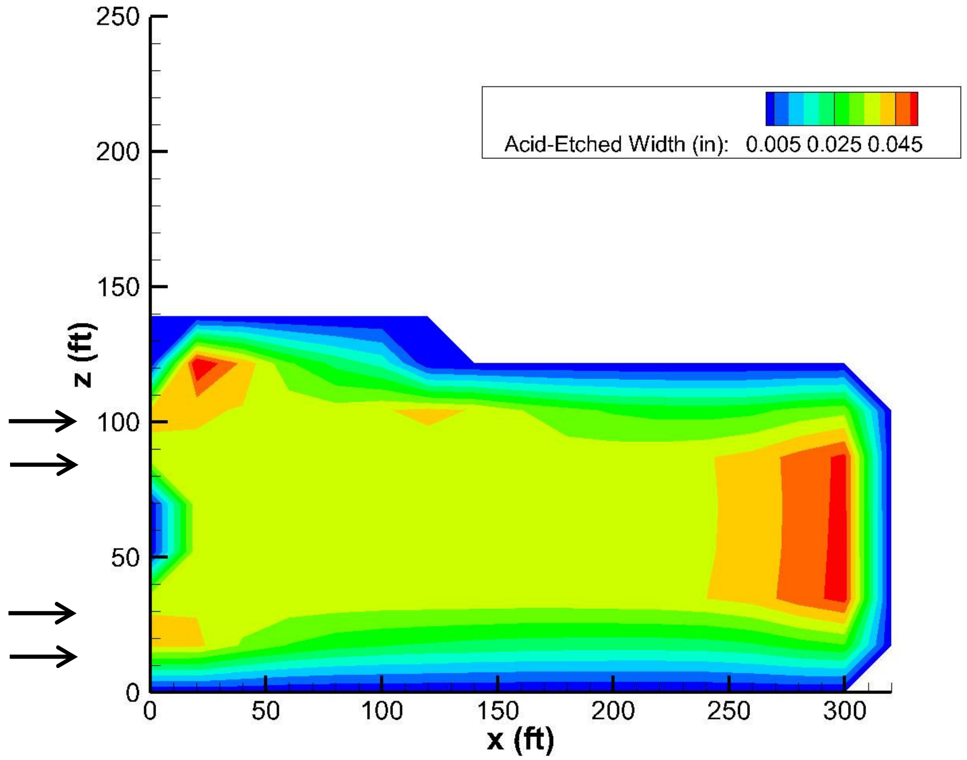

Fig. 4.40—Acid-etched width for the gelled acid case with two 20 foot perforation clusters.

The highest etching occurs near the fluid entrance at the top and bottom portions of the fracture as well as at the fracture tip. There is no etching at the fracture entrance where the fluid does not enter, since the flow pushes the fluid toward the fracture tip. In reality, some diffusion would occur back toward the fracture entrance but the effective diffusion is many orders of magnitude smaller than the convection in this direction. More etching occurs at the locations of narrower initial width because the acid does not spend over the entire fracture as with the densely perforated completion case, so more acid is available to create etching at these locations. The conductivity demonstrates the slightly higher etching that occurs with the limited entrance conditions (Figs. 4.41-4.42).

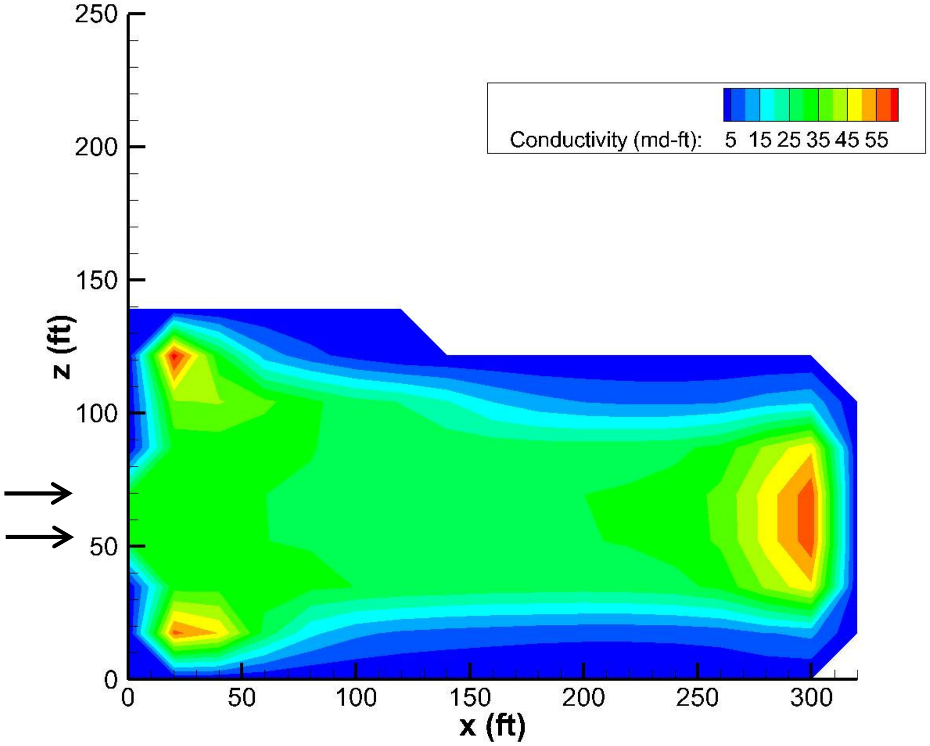

Fig. 4.41—Conductivity after closure for the gelled acid case with 20 foot centered perforations.

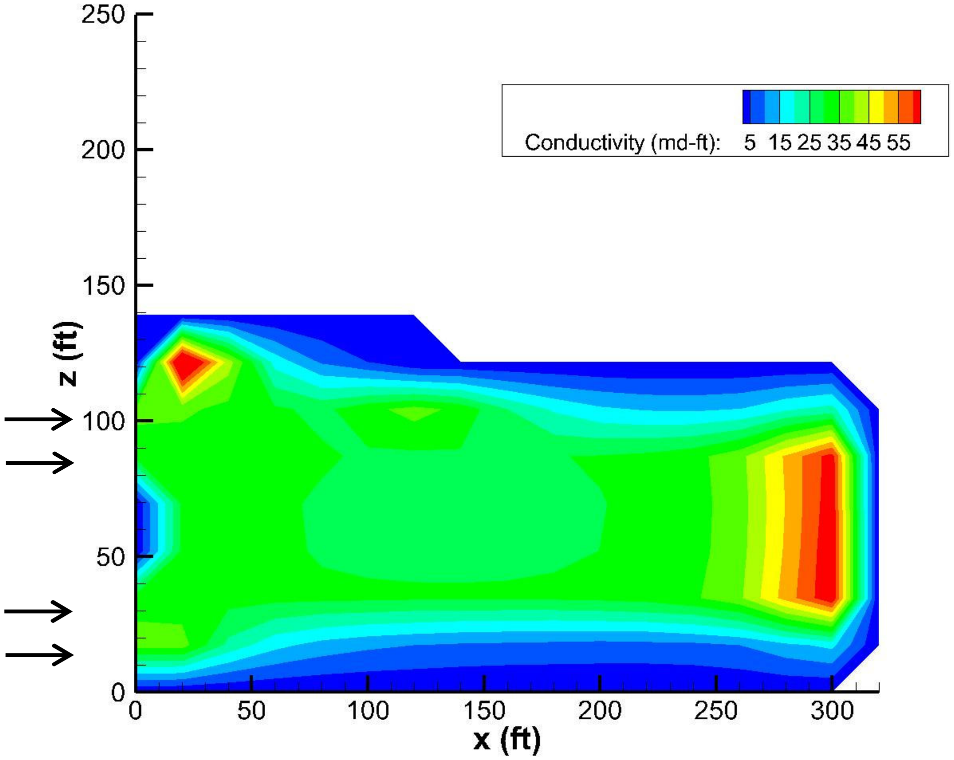

Fig. 4.42—Conductivity after closure for the gelled acid case with two 20 foot perforation clusters.

4.7 Weak Acids

Hydrochloric acid is the most commonly pumped acid for acid fracture treatments (Williams et al., 1979). Hydrochloric acid is typically approximated as being infinitely reactive and can be inappropriate for high temperature, limestone mineralogy formations where the acid spending is fast or in completion schematics where the well tubulars are exposed to the acid for long periods of time. Occasionally, weak acids are pumped to slow the etching across the fracture and minimize corrosion of the well equipment.

Formic acid is one such alternative to hydrochloric acid. It is a weaker, organic acid that reacts incompletely with the carbonate rock. The calculated dissolving power and reaction boundary condition change in the model to reflect that of the formic acid. The input effective diffusion for formic acid would also change and usually the pumped concentrations for organic acids are less than 15% by weight (Buijse et al., 2004), but these input parameters are kept constant for comparative purposes. The boundary condition uses the empirical equation presented in Williams et al. (1979) with the formic acid dissociation constant at the input temperature (100˚F). This creates a quadratic equation for the amount of acid reacted at the fracture surface. Lastly, the concentration for the acid fracture leakoff boundary condition is increased to reflect the lower dissolving power of the formic acid.

Weaker acids have lower dissolving powers than hydrochloric acid, and the result of this is lower generated acid-etched width compared to the original gelled HCl acid case (Fig. 4.43).

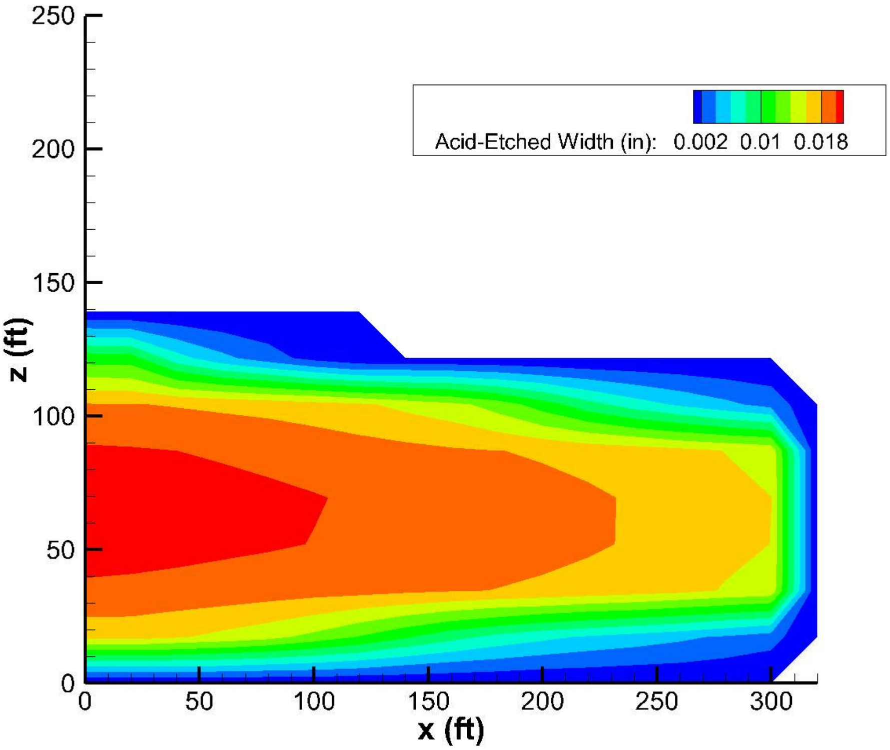

Fig. 4.43—Acid-etched width for the weak acid case.

The acid-etched width is about half that of the original HCl gelled acid case. The combination of the lower dissolving power, higher acid fracture leakoff concentration condition, and reverse reaction boundary condition diminishes the acid-etched width over the extent of the fracture. The acid-etched width follows a different shape than for the fast reacting HCl acid, because the acid concentration is higher in the fracture as the concentration builds at the fracture surface. After closure, the high concentration of acid in the fracture then creates additional etching that follows the shape of the fracture width. This is further demonstrated by the fracture conductivity (Fig. 4.44).

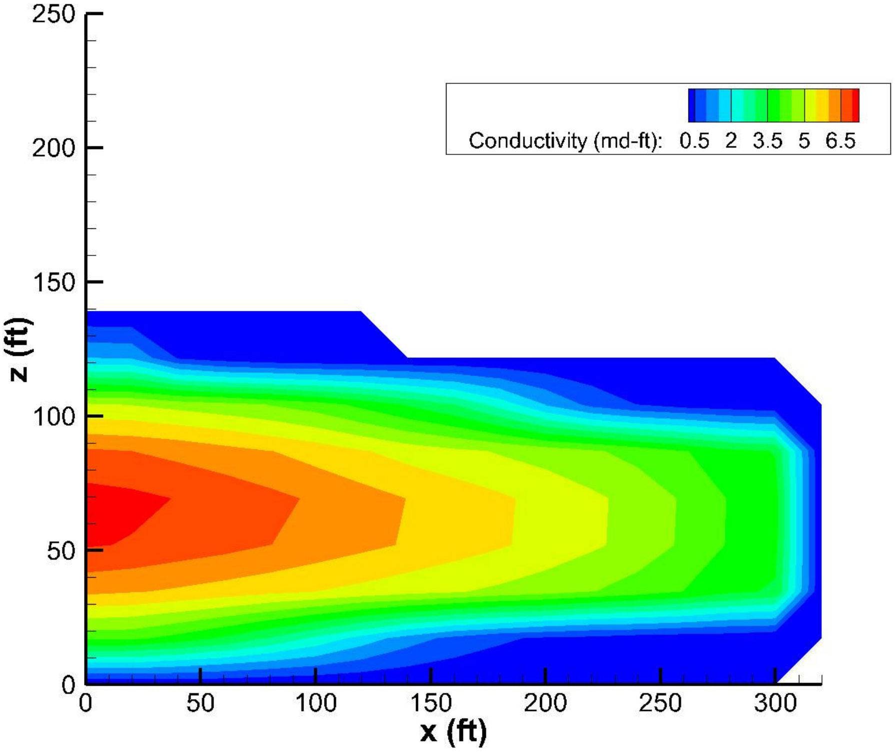

Fig. 4.44—Conductivity after closure for the weak acid case.

The tradeoff in using weaker acids is that etching is generally extended along the fracture length and the risk of corrosion is diminished, but significantly lower conductivity is created compared to the standard HCl gelled acid treatment. The model allows for both types of acids to be input and evaluated for treatment design.

4.8 Radial Fracture Geometry

The same input data used in the confined or PKN geometry case is used to demonstrate the etching expected with a radial geometry fracture (Fig. 4.45).

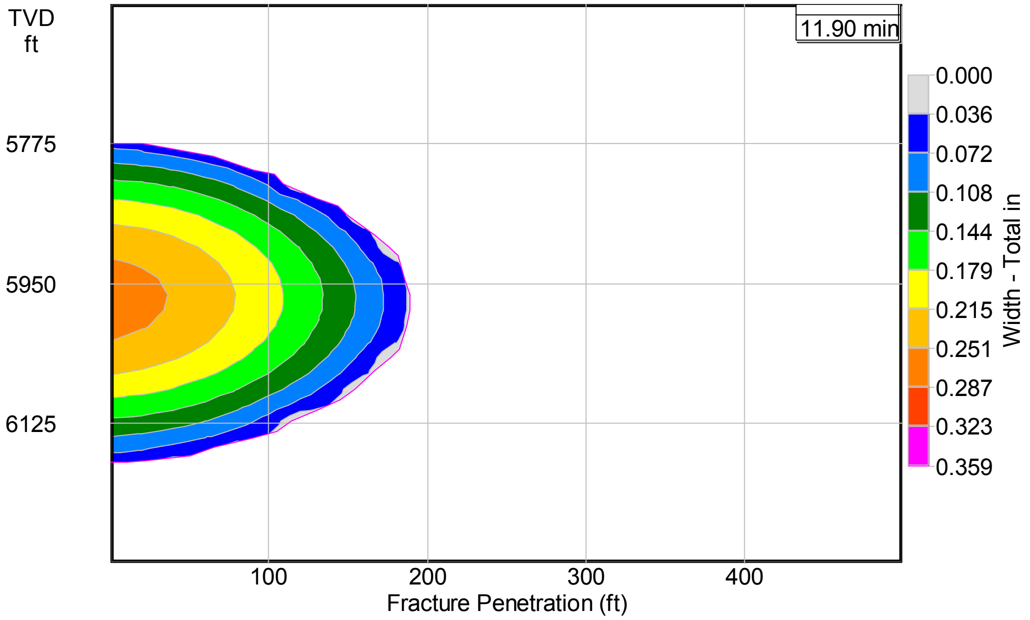

Fig. 4.45—Fracture geometry from StimPlan at end of 30# crosslinked pad injection without stress barriers.

The radial geometry case has a radius of approximately 200 feet. The initial width is lower and about 80% of that for the confined fracture geometry case. The pressure required to push the same flow rate of fluid through the fracture is presented in Figure 4.46.

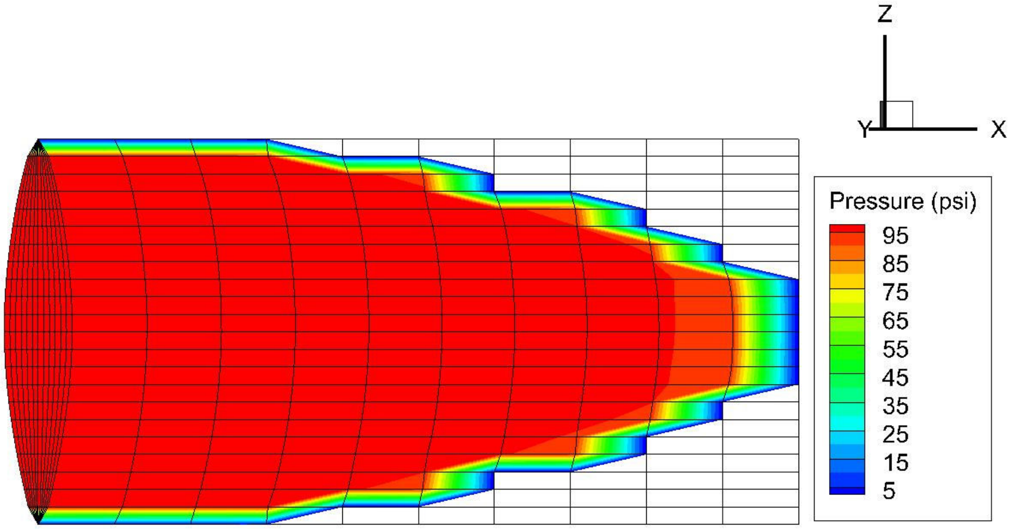

Fig. 4.46—Fracture pressure for the gelled acid case with radial fracture geometry.

Despite the higher pressure in the fracture, because of the larger fracture height the *x*-direction velocity is lower everywhere (Fig. 4.47). Fluid is allowed to exit the fracture in the *x*-direction at any location on the fracture tip (anywhere the width goes to zero in the *x*-direction). The flow moves across the fracture height to exit at these locations along the fracture (Fig. 4.48). Anywhere the flow leaks out the fracture ends causes movement in the vertical direction to replace this lost flow in the fracture (as was observed with the confined fracture geometry case).

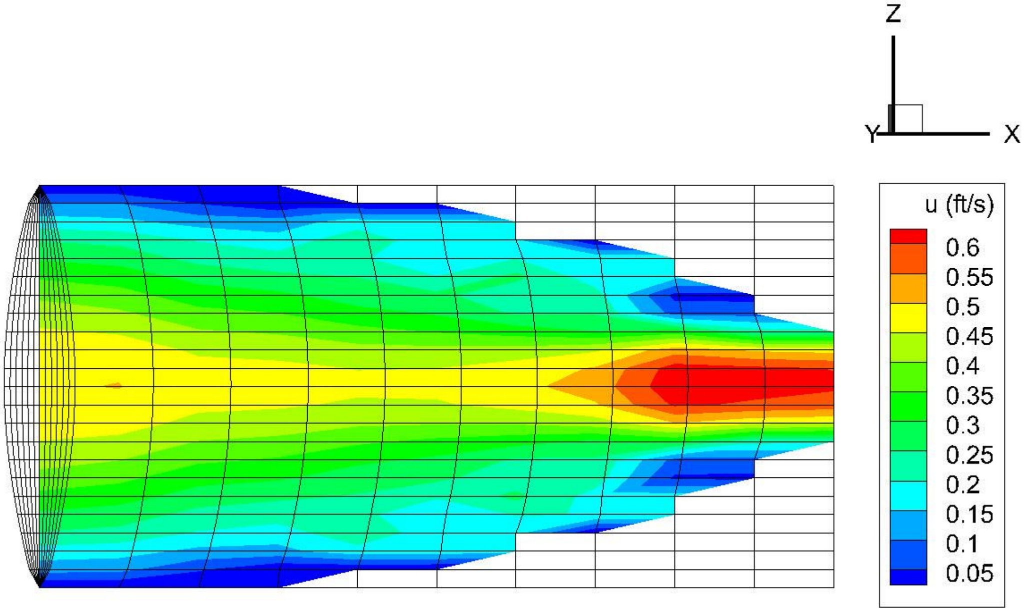

Fig. 4.47—Velocity in the *x*-direction across the fracture height for the gelled acid case with radial fracture geometry.

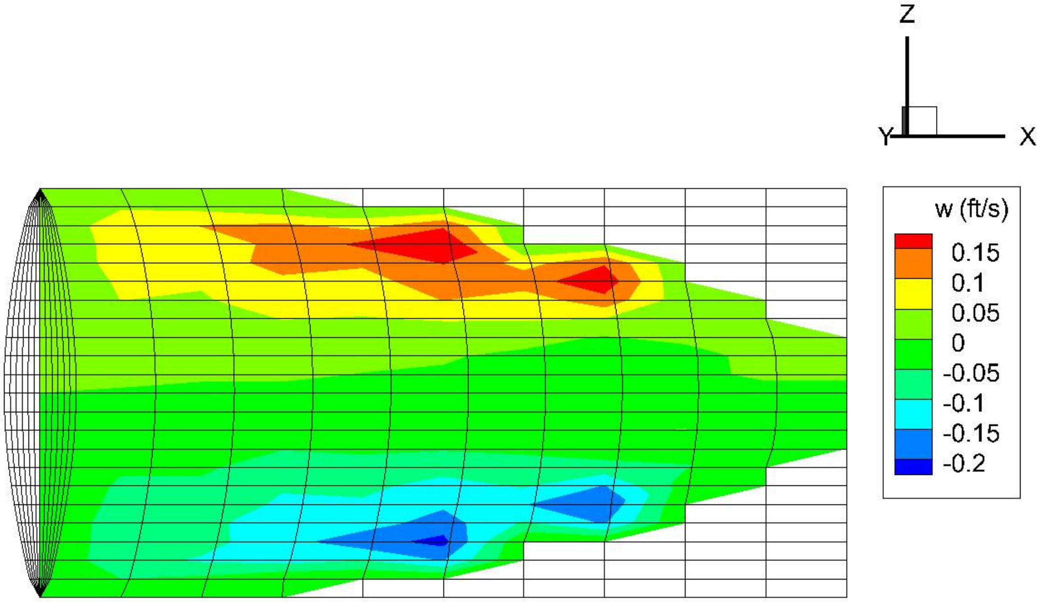

Fig. 4.48—Velocity in the *z*-direction across the fracture height for the gelled acid case with radial fracture geometry.

The initial Peclet number is approximately 10 for this case. The fracture surface area is over 50% larger, which decreases the leakoff velocity out the fracture surfaces for the same zero efficiency treatment. The larger fracture area would result in lower acid-etched width everywhere, but this is counteracted to a degree by the lower initial width for the radial case. Despite the lower Peclet number and larger fracture area compared to the confined geometry case, high concentrations of acid occur throughout the fracture to generate relatively even etching on the fracture surfaces (Fig. 4.49).

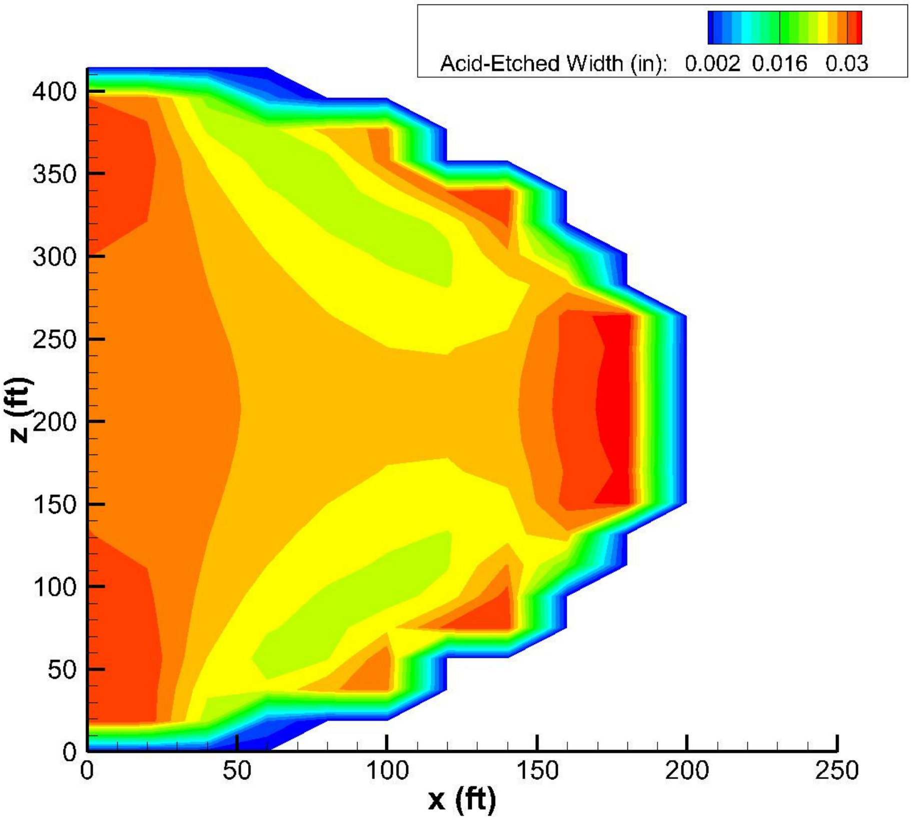

Fig. 4.49—Acid-etched width for the gelled acid case with radial fracture geometry.

The areas with lower initial width still show relatively larger etching. The etching is lower across the fracture compared to the confined geometry case due to the lower leakoff and also noting that the same mass of injected acid generates etching across a much larger fracture area. The conductivity is correspondingly lower (Fig. 4.50).

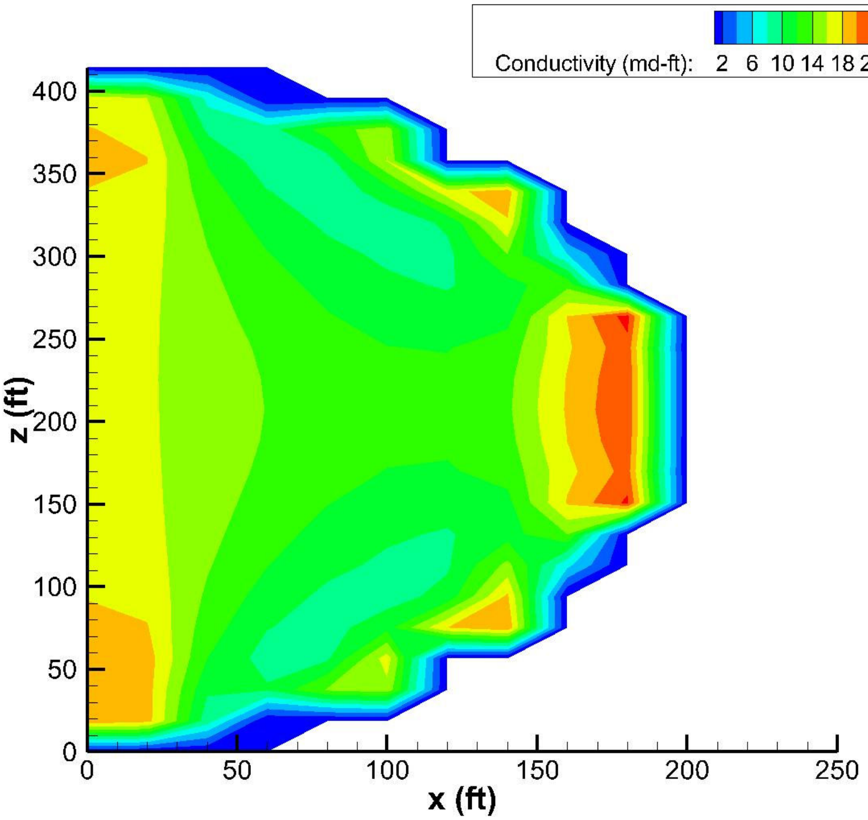

Fig. 4.50—Conductivity after closure for the gelled acid case with radial fracture geometry.

The radial case demonstrates that the characteristics of the model for the prediction of the acid-etched width and resulting conductivity remain consistent: areas of lower initial width generate more etching for fast reacting acid fluid systems but the

Peclet number determines the overall shape of the etching across the fracture. The model can accept different fracture geometries as input as long as the grid stability criteria are maintained. For most cases, it is recommended that 20 foot grid blocks be used in the *x*-direction and particularly for restricted entrance conditions (i.e., perforation clusters). A grid block size of 10 feet is usually appropriate in the *z*-direction. The grid block size in the *y*-direction is automatically determined within the model. This grid block size is set based on the Peclet number and analytical match developed in Chapter III.

4.9 Reynolds Numbers for Fracture Cases

The Reynolds number has been calculated for each case presented in this parametric study at the end of the simulated treatment (Table 4.3). The Reynolds number indicates a flow transition from laminar to turbulent conditions, but no modeling of turbulent flow characteristics is part of this work. Research on the nature of turbulence in channels with power law fluids is ongoing (Zhen et al., 2013).

Table 4.3—Reynolds numbers for cases presented in Chapter IV.

Case	Reynolds Number	Case	Reynolds Number
Gelled Acid	429	10 BPM Pump Rate	230
Weakly Gelled Acid	533	Mixed Geology	453
Straight Acid	2336	Centered Perforations	831
Dolomite Gelled Acid	435	Two Perforation Clusters	616
Nonzero Fluid Efficiency	471	Weak Acid	465
Gelled Acid, 28% HCl	390	Radial Geometry	79

4.10 Finer Gridding for Confined Geometry, Gelled Acid Case

The first confined fracture geometry, gelled acid case presented in this chapter is simulated again with halved grid block sizes in the *x*- and *z*-directions (10 feet by 10 feet versus 20 feet by 20 feet). The interpolated average width based on the StimPlan output fracture geometry is used to populate the width arrays for the additional model blocks. The final calculated acid-etched width is presented in Figure 4.51.

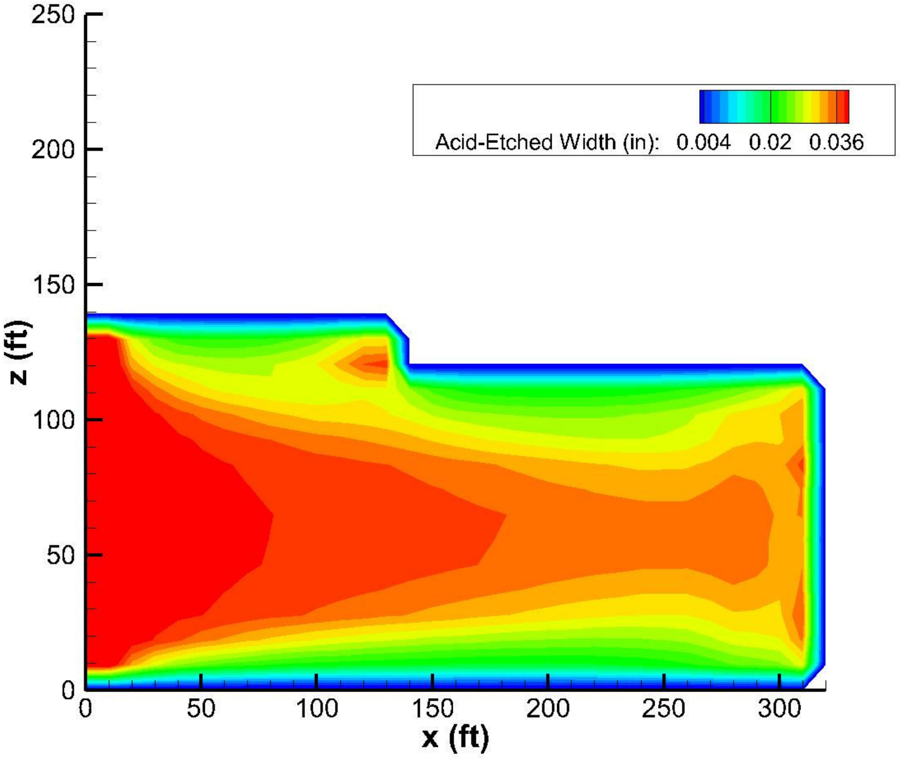

Fig. 4.51—Acid-etched width for finer gridded gelled acid case.

The same absolute values of acid-etched width are calculated for both the finer and coarser simulations. Also, the majority of etching is creating near the wellbore and at areas with small initial width (i.e., the tip of the fracture), which agrees with the coarser simulation output. The overall features of the acid-etched width profile for the coarser model are supported by the finer model output. The finer model has a smoother acid-etched width profile overall with slightly less etching concentrated at the fracture tip, but the general shape and profile values are captured by the coarser model. The same can be observed for the output fine grid conductivity in comparison to the original gelled acid coarse grid simulation conductivity (Fig. 4.52).

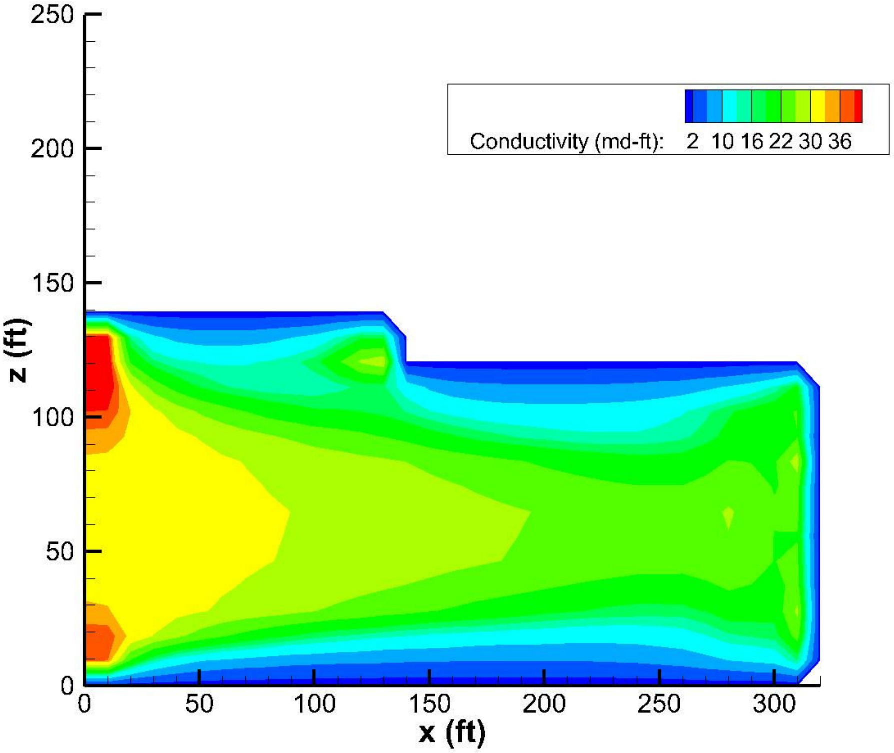

Fig. 4.52—Conductivity for finer gridded gelled acid case.

CHAPTER V

FIELD CASE STUDY

This chapter demonstrates how actual field cases may be analyzed by modeling a multistage acid fracture treatment pumped in the Permian Basin. The model is used to estimate the conductivity generated during this treatment and to provide recommendations for future acid fracture treatments. The first section concerns diagnostic evaluation of an acid fracture treatment in the Scurry Area Canyon Reef Operators Committee (SACROC) Unit. The second section offers recommendations for future acid fracture treatment designs in the SACROC Unit based on the results of the real acid fracture case study.

5.1 SACROC Well Lower Stage Acid Fracture Analysis

The SACROC Unit is a unitized field that comprises the Canyon Reef reservoir in Scurry County, Texas (Brummett et al., 1976). The formation is a limestone reef with average producing depth of 6700 feet. Discovered in 1948, the reservoir was first produced under depletion (solution gas drive), followed by unitization and pressure maintenance in 1957, and then converted to pattern waterflooding and CO_2 injection beginning in 1979. Currently the field is producing by miscible CO_2 enhanced oil recovery. To improve productivity and processing rates, acid fracture treatments are executed for producers and injectors alike in the lower Middle Canyon section of the reservoir.

The field case study well is an injector at the crest of the reef structure that is completed in the Middle Canyon layer in the Canyon Reef reservoir. The well was stimulated with two gelled acid fracture treatments in July 2011. The lower treatment was pumped through two perforation clusters. This treatment includes four stages of 15% by weight HCl gelled acid. The treatment fluid types, volumes, and the average surface pump rate for each stage are presented in Table 5.1. A 20% by weight HCl acid with a non-emulsified iron control system was pumped ahead of the acid fracture treatment for sludge prevention, and that portion of the treatment is not part of this analysis.

Table 5.1—Pump schedule for lower acid fracture treatment.

Stage Number	Fluid Description	Volume (bbl)	Average Surface Pump Rate (BPM)
1	Brine	64.3	4.6
2	30# crosslinked fluid	46.0	4.7
3	15% by weight gelled HCl	25.2	4.6
4	30# crosslinked fluid	46.9	6.6
5	15% by weight gelled HCl	23.8	7.6
6	30# crosslinked fluid	46.7	5.0
7	15% by weight gelled HCl	24.1	7.9
8	30# crosslinked fluid	50.7	7.9
9	15% by weight gelled HCl	23.3	7.8
10	Flush	84.1	7.8

The service company supplied rheological parameters are used in combination with the pump schedule and log data to populate a fracture geometry model. The fracture geometry just before the first acid injection stage is presented in Figure 5.1.

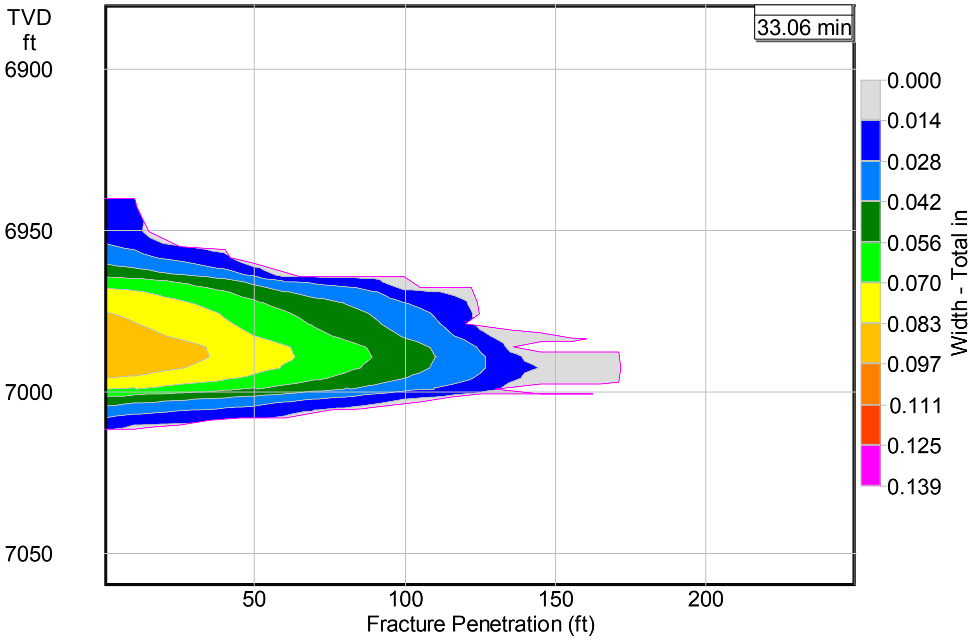

Fig. 5.1—Fracture geometry from StimPlan at the end of the first 30# crosslinked pad stage.

The model takes into account the flush volume specified by the user to simulate a nonreactive fluid displacing the acid through the fracture. Etching is calculated during the displacement stage and summarizes the acid-etched width created during the entire gelled acid stage. The acid-etched width at the end of the first acid injection stage is presented in Figure 5.2.

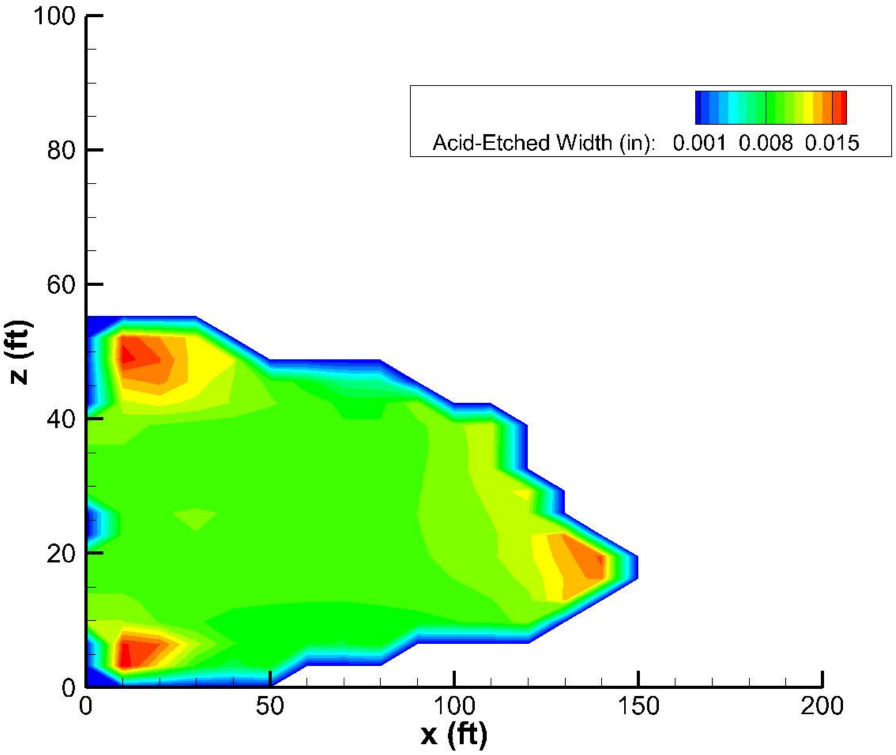

Fig. 5.2—Acid-etched width across the fracture at the end of the first acid injection stage.

The initial Peclet number for this case is 7.1. Etching occurs almost evenly across the fracture, which is expected given the relatively high Peclet number. The fluid efficiency during the treatment is nearly zero (calculated by StimPlan). The fracture is barely open with the total bottomhole 7.2 BPM flow rate, being close to closure and having fracture widths less than 0.1 inches throughout the fracture. The acid concentration in the fracture demonstrates how the acid spends across the fracture with slightly lower concentrations at the tip. A series of images demonstrates how the acid fluid is flushed from the fracture with the next 30# crosslinked pad stage (Figs. 5.3-5.4).

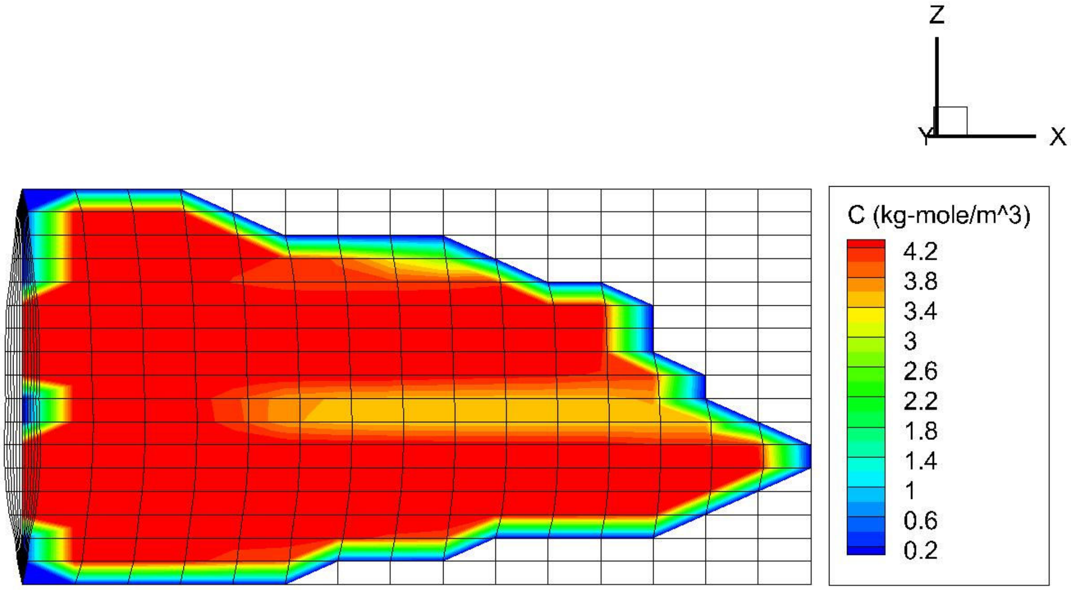

Fig. 5.3—Acid concentration at fracture centerline just before the second 30# crosslinked stage enters the fracture.

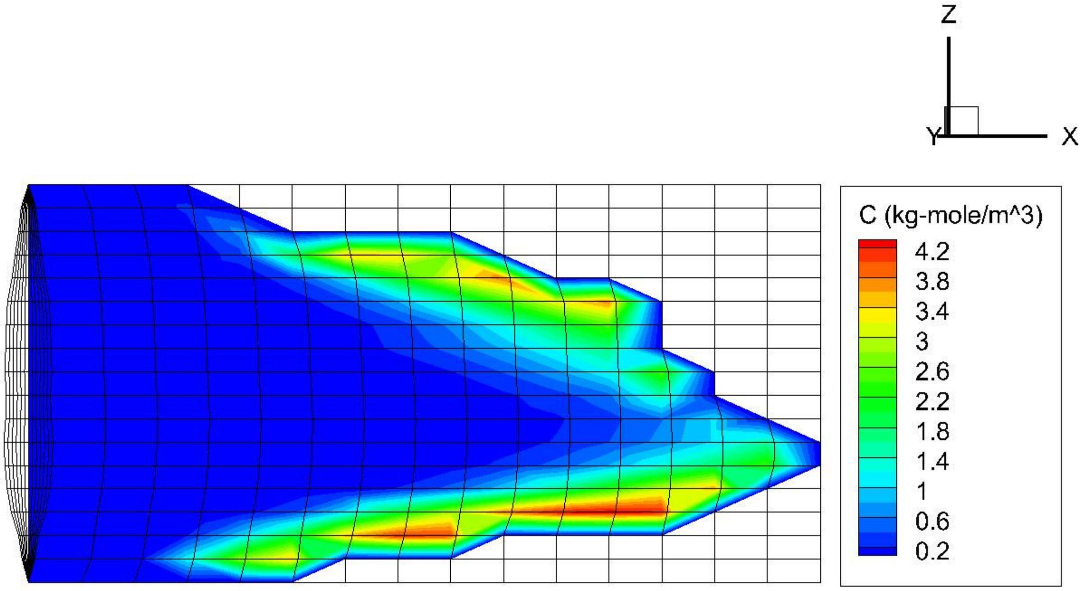

Fig. 5.4—Acid concentration at fracture centerline as the 30# crosslinked stage flushes the fracture.

The geometry for the beginning of the next acid injection stage is also taken from the same StimPlan simulation. The fluid properties for the gelled acid system were input to StimPlan but no acid concentration was specified as part of the StimPlan simulation. This was done intentionally to preserve just the hydraulic geometry coming from StimPlan based on the rheological properties of the fluids and stresses in the formation. Note that this approach assumes that the acid-etched width has little impact on the overall fracture geometry.

The geometry from StimPlan at a simulated treatment time just before the second acid stage enters the fracture is input to the acid fracture model. The fracture area is slightly smaller than for the previous acid stage, because a job shut down occurred just before the second acid stage entered the fracture. This caused the fracture to close and it is reopening as the second acid injection stage is pumped. The acid-etched width resulting from the next stage of acid injection is presented in Figure 5.5.

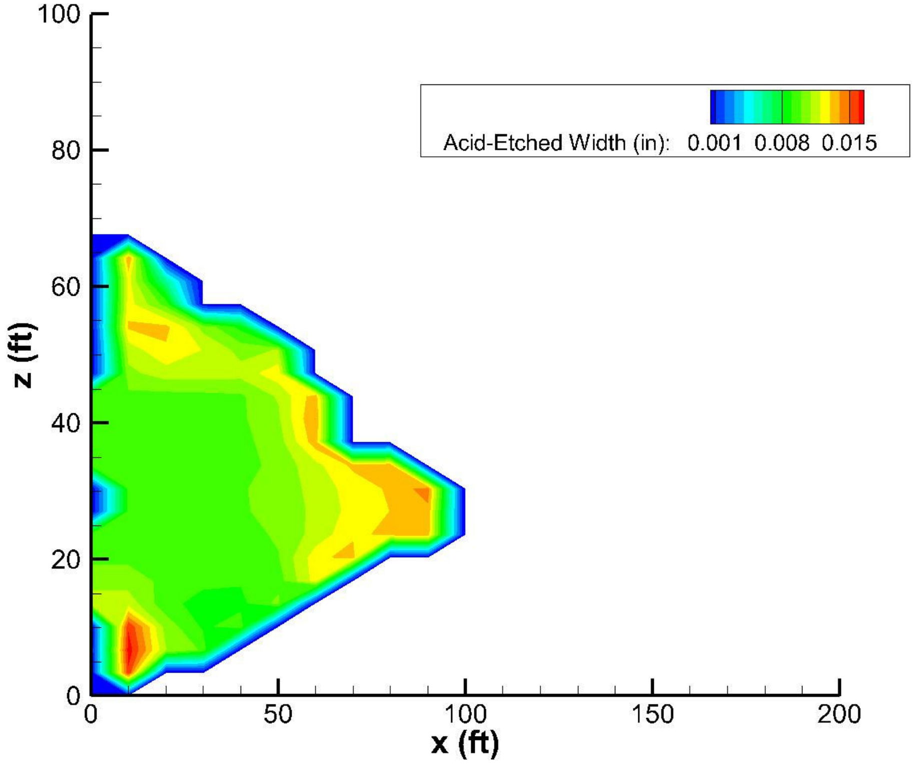

Fig. 5.5—Acid-etched width generated from the second acid injection stage.

The job was briefly shut down just ahead of this acid stage entering the fracture, and the fracture length is recessed compared to the first acid injection stage. Approximately the same volume of acid was injected during the second acid stage as was for the first acid stage. Despite the fracture recessing in length, the height grows so that the total fracture area is similar to that during the first acid injection stage and nearly the same acid-etched width is created across the fracture. The acid-etched width is still developed largely in areas of lower initial fracture width. This is emphasized by the fact that each acid stage is followed by a large flush stage that displaces the acid fluid in the fracture. This demonstrates how important the fracture width is to the spending of acid and creation of etching in the fracture.

The simulated acid-etched width for the final two stages of acid injection is presented in Figures 5.6-5.7. The shape and magnitude of the acid-etched width across the fracture remains the same as the Peclet number ranges based on the fracture geometry from 4.6 to 12.4 among the four stages and the volume of acid pumped for each acid injection stage is similar.

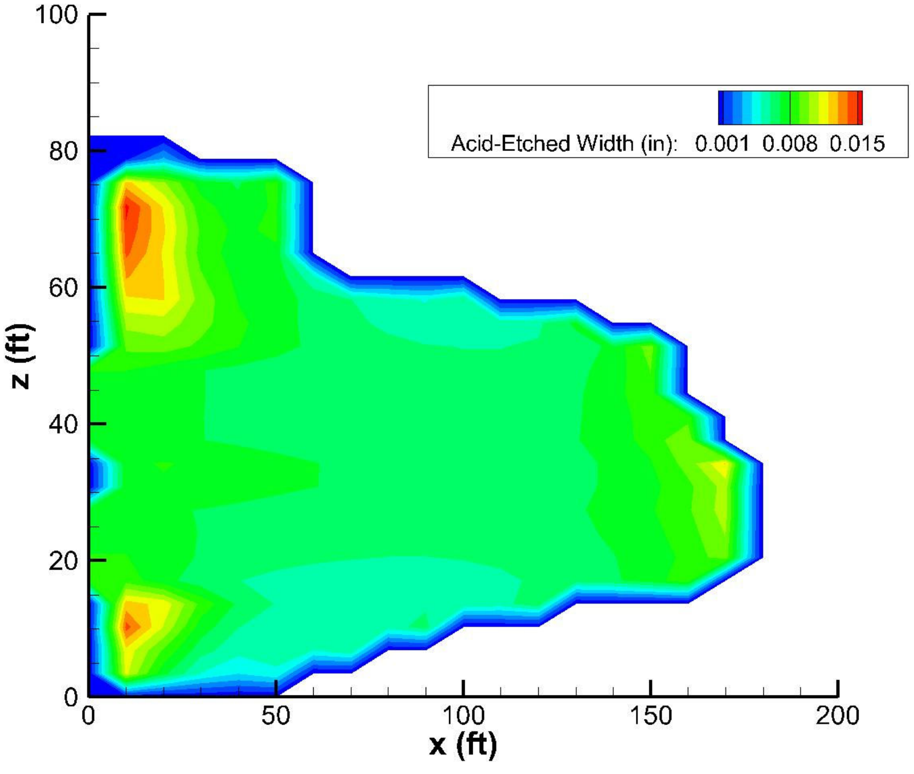

Fig. 5.6—Acid-etched width generated from the third acid injection stage.

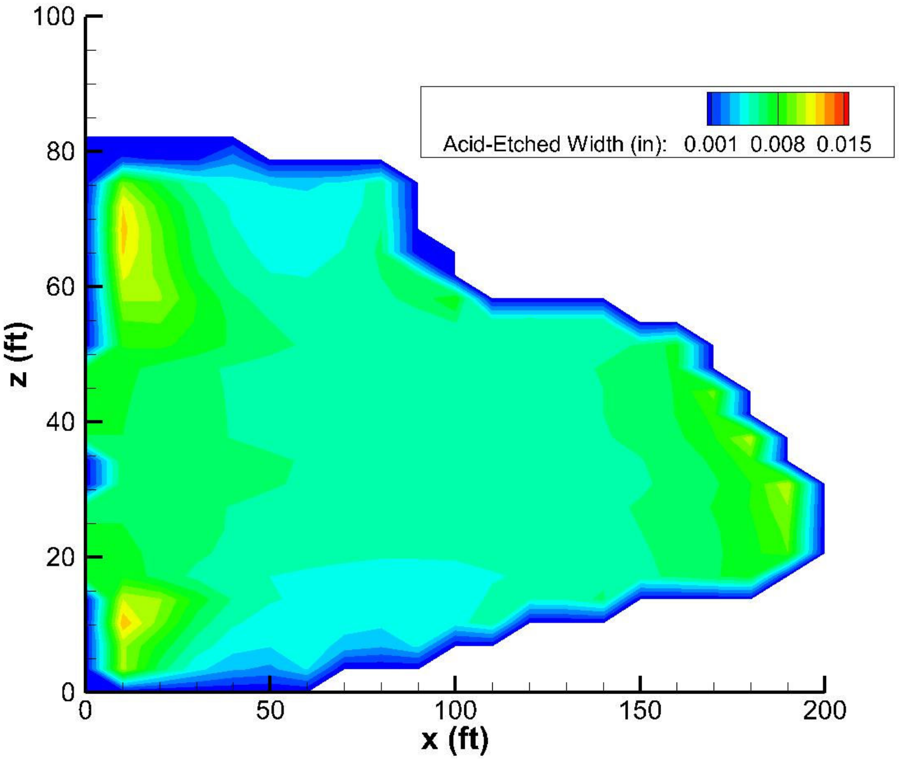

Fig. 5.7—Acid-etched width generated from the fourth acid injection stage.

The final step in analyzing the total treatment benefit is to add all the acid-etched widths together from each of the acid injection stages and then calculate the total conductivity. This information is presented in Figures 5.8-5.9.

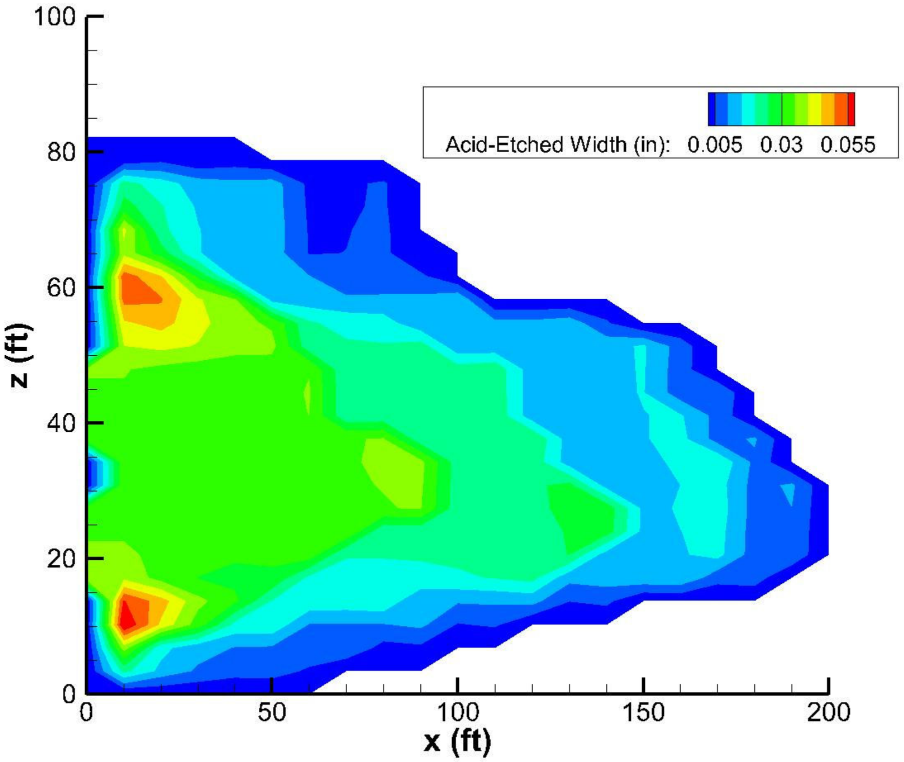

Fig. 5.8—Total acid-etched width generated during the multistage acid fracture treatment.

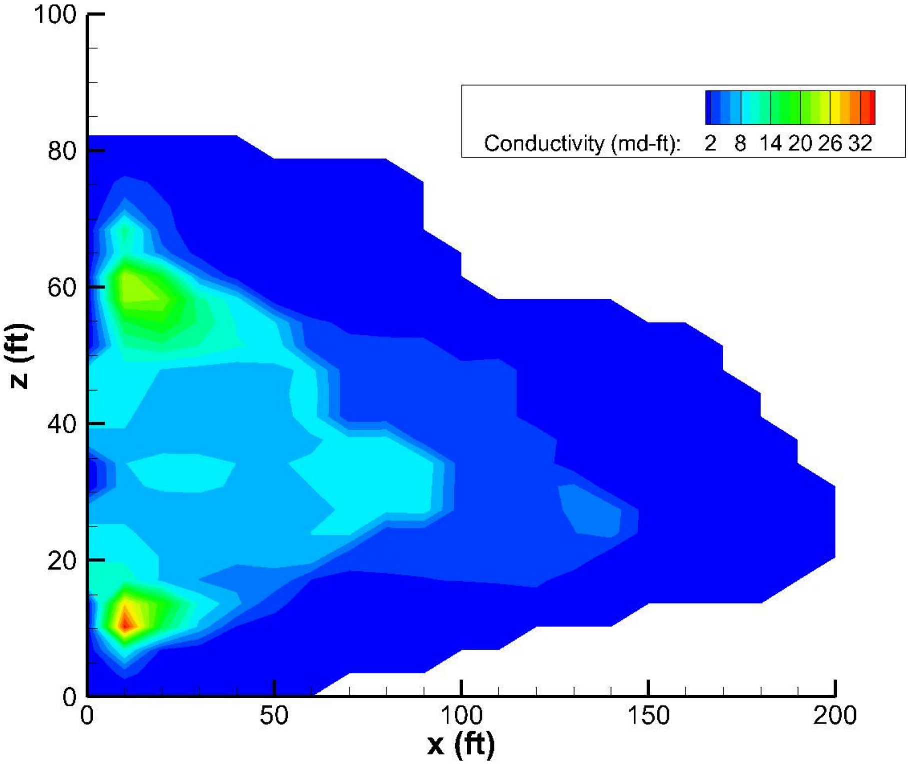

Fig. 5.9—Total conductivity generated during the multistage acid fracture treatment.

The same geostatistical parameters are used across the fracture in the Mou-Deng conductivity correlation and represent the characteristics of the formation. These parameters indicate the formation is not strongly layered $\left(\lambda_{D,x} = 1, \lambda_{D,z} = 0.75, \sigma_D = 0.2\right)$. Acid-etched width is generated across most of the fracture, but most of the conductivity is created in the first half of the fracture and in the vicinity of the perforations. The arithmetic average of conductivity across the fracture for locations where there is acid-etched width is approximately 4 md-ft after closure. This suggests that the acid fracture treatment provided a small stimulation benefit. Injectivity records show no prior injection into the Middle Canyon layer, so the injectivity before and after the acid fracture treatments cannot be compared. The results of the model indicate that well stimulation did occur but it is unclear how successful the actual treatment was in improving the well injectivity.

StimPlan can also be used to calculate the acid-etched width resultant from a particular treatment. For comparative purposes, an acid concentration of 15% by weight HCl is added to the StimPlan fracture model acid fluid and the output acid-etched width is presented in Figure 5.10.

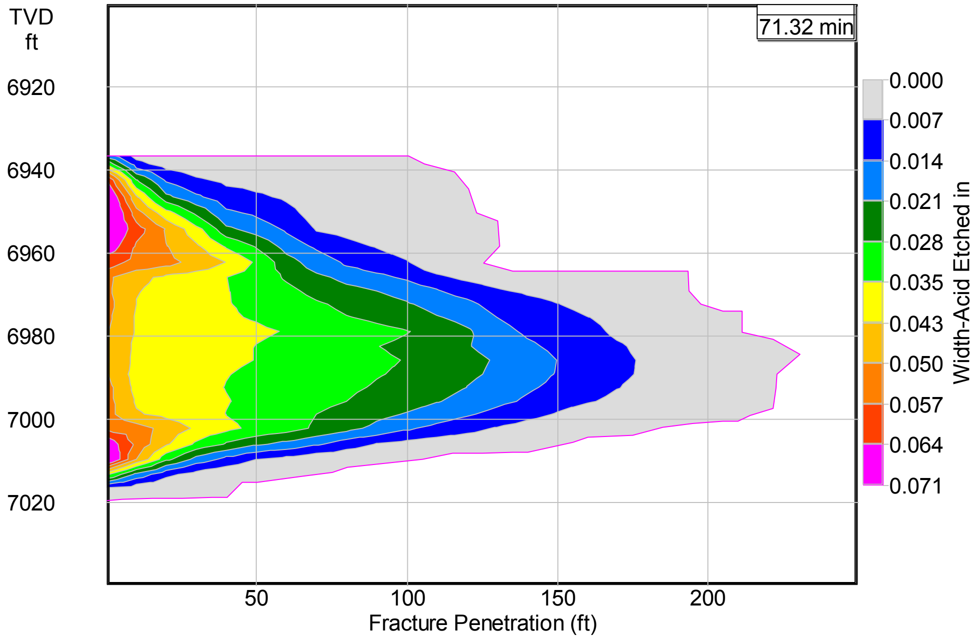

Fig. 5.10—StimPlan predicted total acid-etched width for Middle Canyon acid fracture treatment.

The acid-etched width predicted by StimPlan is similar in magnitude to that predicted with the new acid model. The shape of the acid-etched width supports higher etching in the top and bottom portions of the fracture near the perforations, which is also a feature of the acid-etched width calculated by the new acid model. The penetration of the acid-etched width estimated by each simulator is similar with most of the acid-etched width generated in the middle of the fracture to an extent of about 150 feet. Despite not simulating the changes in fracture geometry during the treatment and the effect of the acid-etched width on the fracture geometry, the acid transport and dissolution model agrees reasonably with the output acid-etched width provided by StimPlan. This is in part due to the fracture being a near zero efficiency fracture, which supports the acid fracture model's assumptions.

5.2 Recommendations for Future Treatments

The acid fracture treatments pumped for the two zones are meant to improve the injectivity of the well. This being the case, the operator may prefer to have more etching near the perforations where the injected fluid is entering the fracture. If this is the case, the treatment design is most likely acceptable. Even more acid or higher concentrations of acid could have been pumped to spend near the perforations and create additional acid-etched width. It is important to emphasize that the effective diffusion input to the model for this field case is based on a literature review. If the effective diffusion is higher, then more etching would occur near the fluid entrance at the perforations and the stimulation benefit would differ from what is predicted here.

Both StimPlan and the acid fracture model simulations indicate that the fluid efficiencies during the treatment are very close to zero. This means the fracture is trying to close during the treatment. As the fracture closes, the width diminishes and this causes the acid to spend faster. Increasing the surface flow rate after the first acid stage sustained a larger overall fracture width. This allows the acid to move farther down the fracture and create more acid-etched width over the entire fracture area instead of spending near the fluid entrance. Different fluids with larger viscosities could also be pumped to increase the hydraulic width in the fracture and improve acid transport toward the end of the fracture. However, if the goal is to create most of the etching near the fracture entrance, then the pumped fluids may be satisfactory.

The operator could consider investing in collecting post- and pre-treatment flow records for some zones of interest to investigate comprehensively how acid fracture treatment designs are proceeding in the field. It is impossible to validate the model analysis without some actual data pertaining to the flow being injected into or produced from a zone. If more effort is to be dedicated toward acid fracture treatment analysis and design, a plan for data collection before and after a treatment should be the first step toward treatment analysis.

CHAPTER VI

SUMMARY AND RECOMMENDATIONS

6.1 Model Summary

The model presented in this work is a three-dimensional acid transport and etched width simulator. A standard computational fluid dynamics algorithm is used to determine fluid movement in the fracture. The fluid movement defines how acid is convected through the fracture, and this is coupled to the diffusion of acid to the fracture surfaces. The resolved acid concentration profile determines the acid that is present near the fracture walls, and this is used to calculate the etching that can occur for a specific acid fracture treatment. Lastly, the etching is used to resolve the conductivity by way of newly presented conductivity correlations that incorporate small scale etching effects to describe the treatment performance.

The model adds a number of new features to the simulation of acid fracture treatments. The most important feature is that the fracture interior is gridded in all three directions. This allows the severe concentration profile that occurs across the fracture width to be captured as well as changes along the fracture height (e.g., layer mineralogy, layer permeability, and velocity gradients in the vertical direction). In using a computational fluid dynamics approach, the velocity profiles throughout the fracture are resolved instead of assuming the shape of a profile based on an analytical expression. The power law apparent viscosity can also be calculated precisely instead of using the standard gross shear rate in the x-direction through the fracture. The velocity profile is input directly to the partial differential equation for the acid concentration and affects how the diffusion is resolved throughout the fracture. This is the first model to use computational fluid dynamics to describe the three-dimensional profile of acid throughout a fracture to quantify the etching and conductivity that occurs for a specific acid fracture treatment.

The simulator does not describe all the physics of the acid fracture treatment process. The simulator only accepts one initial fracture geometry and updates the acid-etched width. No geomechanical effects are considered during the model simulation. The width is a critical parameter that defines the acid concentration in the fracture, however, so changes to the fracture geometry during the treatment should not be ignored. Additionally, the temperature throughout the fracture is considered to be constant by the model. This is not physically correct at early time, as fluid movement into a fracture creates a changing temperature profile in the fracture.

6.2 Recommendations for Future Work

The acid transport and etching model correctly predicts how acid moves and reacts to create etching in an irregular, constant geometry. The next step should be incorporation of the geomechanical effects. A more realistic approach would include changing the fracture geometry during a treatment and coupling this to the model. The model could be called in each time step by a fracture geometry simulator to resolve the acid concentration profile in the fracture and the acid-etched width profile. If the time step for the coupled models was small, iteration between the acid-etched width and hydraulic width may not be necessary.

A secondary benefit to incorporating the model to a hydraulic fracture geometry simulator is that many of these commercial packages calculate the temperature throughout the fracture. The acid model would then receive a temperature field as input data to calculate the effect on the effective diffusion, reaction at the boundary, and the rheological properties of the pumped fluids. An additional source of energy, the heat of the acid reacting with the rock, would also need to be added and included as part of the temperature model. Some commercial fracture simulators already include this feature.

The weakest part of this model is the computational fluid dynamics portion of the code. This algorithm is fickle and frequently crashes due to unphysical or divergent solutions. Using a pressure relaxation factor (typically 0.5) is critical to prevent instabilities that cause the code to crash. The initial fracture geometry may include fracture widths that narrow severely in the dominant flow direction. This input geometry can cause high pressures to appear in the acid model and particularly toward the fracture tip. These high pressures reverse the flow direction and the pressure oscillates until the program crashes. The code may also crash because unrealistically high pressures are required to push a certain flow rate through a very narrow portion of the fracture. In reality, this energy could never be supplied and the fracture would close at these locations. Occasionally, the pressure in the fracture may be negative or the pressure at the fracture inlet too low to match the user specified influent flow rate (i.e., too much flow entering the fracture with inlet pressures near zero). These conditions are numerically meaningless but may imply that the fracture geometry could change significantly during the treatment. Since the geometry is a fixed constant excepting the generated acid-etched width, this cannot be updated and the model results suffer from unphysical predictions.

The next step in improving acid fracture treatment design is to couple the three-dimensional acid concentration solution approach developed here to a fracture geometry model. Most hydraulic fracture models use semi-analytical expressions for the velocity profiles in the fracture. Typically the velocity profile results from the model during a simulation were very similar in shape to the analytical equations used by commercial software. The three-dimensional acid solution portion of the code could use the velocity profile (and temperature profile) from the commercial fracture simulator and calculate the acid concentration throughout the fracture. This methodology would marry the benefit of modeling the acid concentration throughout the fracture with the stability of commercial fracture geometry models for better acid-etched width and conductivity predictions.

REFERENCES

Acharya, S. and Moukalled, F.H. 1989. Improvements to Incompressible Flow Calculation on a Nonstaggered Curvilinear Grid. *Numer. Heat Transfer, Part B* **15**(2): 131-152.

Allen, E. 1995. Optimizing the Productivity of Acid-Fracture Treatments in Horizontal Wells. Paper SPE 30530 presented at the SPE Annual Technical Conference & Exhibition, Dallas, Texas, 22-25 October.

Al-Mutairi, S.H., Nasr-El-Din, H.A., Hill, A.D., and Al-Aamri, A.D. 2009. Effect of Droplet Size on the Reaction Kinetics of Emulsified Acid With Calcite. *SPEJ* **14**(4): 606-616.

American Petroleum Institute (API). 2004. *Recommended Practice for the Measurement of Viscous Properties of Completion Fluids*. Washington, D.C.: API Publishing Services.

ANSYS. 2010. FLUENT 13.0 [computer software]. Canonsburg, Pennsylvania: ANSYS, Inc.

Barree, R.D. 1983. A Practical Numerical Simulator for Three-Dimensional Fracture Propagation in Heterogeneous Media. Paper SPE 12273 presented at the Reservoir Simulation Symposium, San Francisco, California, 15-18 November.

Ben-Naceur, K. and Economides, M.J. 1989. Design and Evaluation of Acid Fracturing Treatments. Paper SPE 18978 presented at the SPE Joint Rocky Mountain Regional/Low Permeability Reservoirs Symposium and Exhibition, Denver, Colorado, 6-8 March.

Berman, A.S. 1953. Laminar Flow in Channels with Porous Walls. *J. Appl. Phys.* **24**(9): 1232-1235.

Bird, R.B., Armstrong, R.C., and Hassager, O. 1987. *Dynamics of Polymeric Liquids, Volume 1, Fluid Mechanics*. Hoboken, New Jersey: John Wiley & Sons, Inc.

Brummett, Jr., W.M., Emanuel, A.S., and Ronquille, J.D. 1976. Reservoir Description by Simulation at SACROC – A Case History. *JPT* **28**(10): 1241-1255.

Buijse, M., de Boer, P., Breukel, B., and Burgos, G. 2004. Organic Acids in Carbonate Acidizing. *SPE Prod. & Fac.* **19**(3): 128-134.

Cameron, J.R. and Prud'homme, R.K. 1989. Appendix C, Rheological Models and Friction Factors. In *Recent Advances in Hydraulic Fracturing*, eds. J.L. Gidley, S.A.

Holditch, D.E. Nierode, and R.W. Veatch, Jr., 388-393. Richardson, Texas: Society of Petroleum Engineers.

Canuto, C., Hussaini, M.Y., Quarteroni, A., and Zang, T.A. 1988. *Spectral Methods in Fluid Dynamics*. New York: Springer-Verlag Berlin Heidelberg.

Conway, M.W., Asadi, M., Penny. G.S., and Chang, F. 1999. A Comparative Study of Straight/Gelled/Emulsified Hydrochloric Acid Diffusivity Coefficient Using Diaphragm Cell and Rotating Disk. Paper SPE 56532 presented at the SPE Annual Technical Conference and Exhibition, Houston, Texas, 3-6 October.

Coulter, A.W., Alderman, E.N., Cloud, J.E., and Crowe, C.W. 1974. Mathematical Model Simulates Actual Well Conditions in Fracture Acidizing Treatment Design. Paper SPE 5004 presented at the SPE 49th Annual Fall Meeting, Houston, Texas, 6-9 October.

Davies, D.R., Bosma, M.G.R., and de Vries, W. 1987. Development of Field Design Rules for Viscous Fingering in Acid Fracturing Treatments: A Large-Scale Model Study. Paper SPE 15772 presented at the Fifth SPE Middle East Oil Show, Manama, Bahrain, 7-10 March.

De Rozieres, J., Chang, F.F., and Sullivan, R.B. 1994. Measuring Diffusion Coefficients in Acid Fracturing Fluids and Their Application to Gelled and Emulsified Acids. Paper SPE 28552 presented at the SPE 69th Annual Technical Conference and Exhibition, New Orleans, Louisiana, 25-28 September.

Deng, J., Mou, J., Hill, A.D., and Zhu, D. 2012. A New Correlation of Acid-Fracture Conductivity Subject to Closure Stress. *SPE Prod. & Oper.* **27**(2): 158-169.

Economides, M.J., Hill, A.D., and Ehlig-Economides, C. 1994. *Petroleum Production Systems*. Upper Saddle River, New Jersey: Prentice Hall, PTR.

Fletcher, C.A.J. 1991. *Computational Techniques for Fluid Dynamics 1, Fundamental and General Techniques, Second Edition*. New York: Springer-Verlag Berlin Heidelberg.

Gdanski, R. 2005. Recent Advances in Carbonate Stimulation. Paper IPTC 10693 presented at the International Petroleum Technology Conference, Doha, Qatar, 21-23 November.

Goel, N. and Shah, S. 2001. A Rheological Criterion for Fracturing Fluids to Transport Proppant during a Stimulation Treatment. Paper SPE 71663 presented at the SPE Annual Technical Conference and Exhibition, New Orleans, Louisiana, 30 September – 3 October.

Guo, J., Li, Y., Zhao, J., and Luo, J. 2004. Research of Three-Dimensional Model for Acid Fracturing and Optimum Design for the Treatments. Paper 2004-011 presented at the Petroleum Society's 5th Canadian International Petroleum Conference (55th Annual Technical Meeting), Calgary, Alberta, 8-10 June.

Hendrickson, A.R., Rosene, R.B., and Wieland, D.R. 1960. Acid Reaction Parameters and Reservoir Characteristics Used in the Design of Acidizing Treatments. Paper SPE 71 presented at the 137th National Meeting of the Petroleum Division of the American Chemical Society, Cleveland, Ohio, April.

Hill, A.D., Zhu, D., and Wang, Y. 1995. The effect of wormholing on the fluid-loss coefficient in acid fracturing. *SPE Prod. Fac.* **10**(4): 257-263.

Issa, R.I. 1985. Solution of the Implicitly Discretised Fluid Flow Equations by Operator-Splitting. *J. Comput. Phys.* **62**(1): 40-65.

Kalfayan, L.J. 2007. Fracture Acidizing: History, Present State, and Future. Paper SPE 106371 presented at the SPE Hydraulic Fracturing Technology Conference, College Station, Texas, 29-31 January.

Li, Y., Sullivan, R.B., de Rozieres, J., Gaz, G.L., and Hinkel, J.J. 1993. An Overview of Current Acid Fracturing Technology With Recent Implications for Emulsified Acids. Paper SPE 26581 presented at the 68th Annual Technical Conference and Exhibition, Houston, Texas, 3-6 October.

Lo, K.K. and Dean, R.H. 1989. Modeling of Acid Fracturing. *SPE Prod. Eng.* **4**(2): 194-200.

Meyer, B.R. 1989. Three-Dimensional Hydraulic Fracturing Simulation on Personal Computers: Theory and Comparison Studies. Paper SPE 19329 presented at the SPE Eastern Regional Meeting, Morgantown, West Virginia, 24-27 October.

Mou, J. 2009. Modeling Acid Transport and Non-Uniform Etching in a Stochastic Domain in Acid Fracturing. Ph.D. dissertation, College Station: Texas A&M University.

Mou, J., Zhu, D., and Hill, A.D. 2010. Acid-Etched Channels in Heterogeneous Carbonates–A Newly Discovered Mechanism for Creating Acid-Fracture Conductivity. *SPEJ* **15**(2): 404-416.

Nasr-El-Din, H.A., Al-Mohammad, A.M., Al-Aamri, A.D., and Al-Fuwaires, O. 2008. Reaction of Gelled Acid With Calcite. *SPE Prod. & Oper.* **23**(3): 353-361.

National Institute of Standards and Technology (NIST). 2004. IML++ (Iterative Methods Library) v. 1.2a. <http://math.nist.gov/iml++/>

Nierode, D.E. and Kruk, K.F. 1973. An Evaluation of Acid Fluid Loss Additives, Retarded Acids, and Acidized Fracture Conductivity. Paper SPE 4549 presented at the SPE Annual Fall Meeting, Las Vegas, Nevada, 30 September – 3 October.

Nierode, D.E. and Williams, B.B. 1971. Characteristics of Acid Reaction in Limestone Formations. *SPEJ* **11**(4): 406-418.

Novotny, E.J. 1977. Prediction of Stimulation From Acid Fracturing Treatments Using Finite Fracture Conductivity. *JPT* **29**(9): 1186-1194.

Oeth, C.V., Hill, A.D., Zhu, D., and Sullivan, R.B. 2011. Characterization of Small Scale Heterogeneity to Predict Acid Fracture Performance. Paper SPE 140336 presented at the SPE Hydraulic Fracturing Technology Conference, The Woodlands, Texas, 24-26 January.

Patankar, S.V. 1980. *Numerical Heat Transfer and Fluid Flow*. New York: Hemisphere Publishing Corporation.

Penny, G.S. and Conway, M.W. 1989. Chapter 8, Fluid Leakoff. In *Recent Advances in Hydraulic Fracturing*, eds. J.L. Gidley, S.A. Holditch, D.E. Nierode, and R.W. Veatch, Jr., 388-393. Richardson, Texas: Society of Petroleum Engineers.

Roberts, L.D. and Guin, J.A. 1974. The Effect of Surface Kinetics in Fracture Acidizing. *SPEJ* **14**(4): 385-395.

Romero, J., Gu, H., and Gulrajani, S.N. 2001. 3D Transport in Acid-Fracturing Treatments: Theoretical Development and Consequences for Hydrocarbon Production. *SPE Prod. & Fac.* **16**(2): 122-130.

Schechter, Robert S. Oil Well Stimulation. Englewood Cliffs, New Jersey: Prentice-Hall, Inc., 1992.

Settari, A. 1993. Modeling of Acid-Fracturing Treatments. *SPE Prod. & Fac.* **8**(1): 30-38.

Settari, A. and Cleary, M.P. 1984. Three-Dimensional Simulation of Hydraulic Fracturing. *JPT* **36**(7): 1177-1190.

Settari, A., Sullivan, R.B., and Hansen, C. 2001. A New Two-Dimensional Model for Acid-Fracturing Design. *SPE Prod. & Fac.* **16**(4): 200-209.

Shah, S.N. and Lord, D.L. 1992. Recent Advances in the Fluid Mechanics and Rheology of Fracturing Fluids. Paper SPE 22391 presented at the SPE International Meeting on Petroleum Engineering, Beijing, China, 24-27 March.

Smith, M.B. 2007. Hydraulic Fracturing, 4th Edition [course notes]. Tulsa, Oklahoma: NSI Technologies, Inc.

Smith, M.B. 2010. StimPlan™/InjecPlan™ Version 6.00 [computer software]. Tulsa, Oklahoma: NSI Technologies, Inc.

Tanner, R.I. 1988. *Engineering Rheology*. Oxford: Oxford University Press.

Terrill, R.M. 1965. Heat Transfer in Laminar Flow Between Parallel Porous Plates. *Int. J. of Heat and Mass Transfer* **8**(12): 1491-1497.

Williams, B.B., Gidley, J.L., and Schechter, R.S. 1979. *Acidizing Fundamentals*. Dallas, Texas: Society of Petroleum Engineers of AIME.

Williams, B.B. and Nierode, D.E. 1972. Design of Acid Fracturing Treatments. *JPT* **24**(7): 849-859.

Zhen, N., Handler, R.A., Zhang, Q., and Oeth, C. 2013. Evolution of a hairpin vortex in a shear-thinning fluid governed by a power-law model. *Phys. Fluids* **25**, 101703.

APPENDIX A

NAVIER STOKES EQUATIONS WITH POWER LAW APPARENT VISCOSITY MODEL

A-1 Derivation of Navier Stokes Equations with Apparent Viscosity

The Navier Stokes equations appear as follows for each direction using a pseudo-steady state numerical approach.

$$u\frac{\partial u}{\partial x}+v\frac{\partial u}{\partial y}+w\frac{\partial u}{\partial z}=-\frac{1}{\rho}\frac{\partial p}{\partial x}+\frac{\mu_{app}}{\rho}\left(\frac{\partial^2 u}{\partial x^2}+\frac{\partial^2 u}{\partial y^2}+\frac{\partial^2 u}{\partial z^2}\right)+$$
$$\frac{1}{\rho}\left(2\frac{\partial u}{\partial x}\frac{\partial \mu_{app}}{\partial x}+\left(\frac{\partial u}{\partial y}+\frac{\partial v}{\partial x}\right)\frac{\partial \mu_{app}}{\partial y}+\left(\frac{\partial u}{\partial z}+\frac{\partial w}{\partial x}\right)\frac{\partial \mu_{app}}{\partial z}\right) \text{.......................................} \textbf{(A. 1)}$$

$$u\frac{\partial v}{\partial x}+v\frac{\partial v}{\partial y}+w\frac{\partial v}{\partial z}=-\frac{1}{\rho}\frac{\partial p}{\partial y}+\frac{\mu_{app}}{\rho}\left(\frac{\partial^2 v}{\partial x^2}+\frac{\partial^2 v}{\partial y^2}+\frac{\partial^2 v}{\partial z^2}\right)+$$
$$\frac{1}{\rho}\left(\left(\frac{\partial u}{\partial y}+\frac{\partial v}{\partial x}\right)\frac{\partial \mu_{app}}{\partial x}+2\frac{\partial v}{\partial y}\frac{\partial \mu_{app}}{\partial y}+\left(\frac{\partial v}{\partial z}+\frac{\partial w}{\partial y}\right)\frac{\partial \mu_{app}}{\partial z}\right) \text{.......................................} \textbf{(A. 2)}$$

$$u\frac{\partial w}{\partial x}+v\frac{\partial w}{\partial y}+w\frac{\partial w}{\partial z}=-\frac{1}{\rho}\frac{\partial p}{\partial z}+\frac{\mu_{app}}{\rho}\left(\frac{\partial^2 w}{\partial x^2}+\frac{\partial^2 w}{\partial y^2}+\frac{\partial^2 w}{\partial z^2}\right)+$$
$$\frac{1}{\rho}\left(\left(\frac{\partial w}{\partial x}+\frac{\partial u}{\partial z}\right)\frac{\partial \mu_{app}}{\partial x}+\left(\frac{\partial w}{\partial y}+\frac{\partial v}{\partial z}\right)\frac{\partial \mu_{app}}{\partial y}+2\frac{\partial w}{\partial z}\frac{\partial \mu_{app}}{\partial z}\right) \text{.......................................} \textbf{(A. 3)}$$

The following dimensionless terms can be used for each direction to make the Navier Stokes equations dimensionless.

$$v_D=U_s v_i \text{ ....} \textbf{(A. 4)}$$
$$x_D=L_c x_j \text{ ....} \textbf{(A. 5)}$$
$$p_D=\frac{p}{\rho U_s^2} \text{ ....} \textbf{(A. 6)}$$

The characteristic velocity is U_s and the characteristic length is L_c in the above expressions. In the *x*-direction, the dimensionless Navier Stokes equation with non-Newtonian, apparent viscosity is derived.

$$u_D \frac{\partial u_D}{\partial x_D} + v_D \frac{\partial u_D}{\partial y_D} + w_D \frac{\partial u_D}{\partial z_D} = -\frac{\partial p_D}{\partial x_D} + \frac{\mu_{app}}{\rho U_s L_c}\left(\frac{\partial^2 u_D}{\partial x_D^2} + \frac{\partial^2 u_D}{\partial y_D^2} + \frac{\partial^2 u_D}{\partial z_D^2}\right) + \frac{1}{\rho U_s L_c}\left(2\frac{\partial u}{\partial x}\frac{\partial \mu_{app}}{\partial x} + \left(\frac{\partial u}{\partial y} + \frac{\partial v}{\partial x}\right)\frac{\partial \mu_{app}}{\partial y} + \left(\frac{\partial u}{\partial z} + \frac{\partial w}{\partial x}\right)\frac{\partial \mu_{app}}{\partial z}\right) \qquad \textbf{(A. 7)}$$

A similar form can be derived for the other two directions.

The apparent viscosity derivative term necessitates calculating the apparent viscosity at each cell face, so that the changes in the apparent viscosity along the fracture width, height, and length can be computed.

A-2 Second Invariant Discretization for Power Law Apparent Viscosity

The power law apparent viscosity is calculated based on the second invariant of the rate of strain tensor.

$$II_d = d_{11}d_{11} + d_{12}d_{21} + d_{13}d_{31} + d_{21}d_{12} + d_{22}d_{22} + d_{23}d_{32} + d_{31}d_{13} + d_{32}d_{23} + d_{33}d_{33} \qquad \textbf{(A. 8)}$$

Since the rate of strain tensor is symmetric ($d_{ij} = d_{ji}$), this expression can be simplified.

$$II_d = d_{11}^2 + d_{22}^2 + d_{33}^2 + 2d_{12}^2 + 2d_{13}^2 + 2d_{23}^2 \qquad \textbf{(A. 9)}$$

The second invariant expression may be expanded based on the definition of the rate of strain tensor.

$$II_d = \left(\frac{1}{2}\left(\frac{\partial u}{\partial x}+\frac{\partial u}{\partial x}\right)\right)^2 + \left(\frac{1}{2}\left(\frac{\partial v}{\partial y}+\frac{\partial v}{\partial y}\right)\right)^2 + \left(\frac{1}{2}\left(\frac{\partial w}{\partial z}+\frac{\partial w}{\partial z}\right)\right)^2 + 2\left(\frac{1}{2}\left(\frac{\partial u}{\partial y}+\frac{\partial v}{\partial x}\right)\right)^2 + 2\left(\frac{1}{2}\left(\frac{\partial u}{\partial z}+\frac{\partial w}{\partial x}\right)\right)^2 + 2\left(\frac{1}{2}\left(\frac{\partial v}{\partial z}+\frac{\partial w}{\partial y}\right)\right)^2 \qquad \textbf{(A. 10)}$$

Each one of these terms then needs to be transformed from the irregular physical domain to the regular computational grid. This is demonstrated for just the *x*-direction velocity component in the following expressions.

$$\frac{\partial u}{\partial x} = \frac{\partial \xi}{\partial x}\frac{\partial u}{\partial \xi} + \frac{\partial \eta}{\partial x}\frac{\partial u}{\partial \eta} + \frac{\partial \zeta}{\partial x}\frac{\partial u}{\partial \zeta} \qquad \textbf{(A. 11)}$$

$$\frac{\partial u}{\partial y} = \frac{\partial \xi}{\partial y}\frac{\partial u}{\partial \xi} + \frac{\partial \eta}{\partial y}\frac{\partial u}{\partial \eta} + \frac{\partial \zeta}{\partial y}\frac{\partial u}{\partial \zeta} \qquad \textbf{(A. 12)}$$

$$\frac{\partial u}{\partial z} = \frac{\partial \xi}{\partial z}\frac{\partial u}{\partial \xi} + \frac{\partial \eta}{\partial z}\frac{\partial u}{\partial \eta} + \frac{\partial \zeta}{\partial z}\frac{\partial u}{\partial \zeta} \qquad \textbf{(A. 13)}$$

The same approach is used for the terms in the other two directions. This is also the approach that is used for the derivative of the apparent viscosity in the Navier Stokes equations.

The discretization of the second invariant of the rate of strain tensor then appears as follows.

$$\psi_{ux} = \frac{\partial \xi}{\partial x}\frac{u_{i+1,j,k}-u_{i-1,j,k}}{2\Delta\xi} + \frac{\partial \eta}{\partial x}\frac{u_{i,j+1,k}-u_{i,j-1,k}}{2\Delta\eta} + \frac{\partial \zeta}{\partial x}\frac{u_{i,j,k+1}-u_{i,j,k-1}}{2\Delta\zeta} \qquad \textbf{(A. 14)}$$

$$\psi_{uy} = \frac{\partial \xi}{\partial y}\frac{u_{i+1,j,k}-u_{i-1,j,k}}{2\Delta\xi} + \frac{\partial \eta}{\partial y}\frac{u_{i,j+1,k}-u_{i,j-1,k}}{2\Delta\eta} + \frac{\partial \zeta}{\partial y}\frac{u_{i,j,k+1}-u_{i,j,k-1}}{2\Delta\zeta} \qquad \textbf{(A. 15)}$$

$$\psi_{uz} = \frac{\partial \xi}{\partial z}\frac{u_{i+1,j,k}-u_{i-1,j,k}}{2\Delta\xi} + \frac{\partial \eta}{\partial z}\frac{u_{i,j+1,k}-u_{i,j-1,k}}{2\Delta\eta} + \frac{\partial \zeta}{\partial z}\frac{u_{i,j,k+1}-u_{i,j,k-1}}{2\Delta\zeta} \qquad \textbf{(A. 16)}$$

$$\psi_{vx} = \frac{\partial\xi}{\partial x}\frac{v_{i+1,j,k} - v_{i-1,j,k}}{2\Delta\xi} + \frac{\partial\eta}{\partial x}\frac{v_{i,j+1,k} - v_{i,j-1,k}}{2\Delta\eta} + \frac{\partial\zeta}{\partial x}\frac{v_{i,j,k+1} - v_{i,j,k-1}}{2\Delta\zeta} \quad \ldots\ldots\ldots\ldots\ldots\ldots \textbf{(A. 17)}$$

$$\psi_{vy} = \frac{\partial\xi}{\partial y}\frac{v_{i+1,j,k} - v_{i-1,j,k}}{2\Delta\xi} + \frac{\partial\eta}{\partial y}\frac{v_{i,j+1,k} - v_{i,j-1,k}}{2\Delta\eta} + \frac{\partial\zeta}{\partial y}\frac{v_{i,j,k+1} - v_{i,j,k-1}}{2\Delta\zeta} \quad \ldots\ldots\ldots\ldots\ldots\ldots \textbf{(A. 18)}$$

$$\psi_{vz} = \frac{\partial\xi}{\partial z}\frac{v_{i+1,j,k} - v_{i-1,j,k}}{2\Delta\xi} + \frac{\partial\eta}{\partial z}\frac{v_{i,j+1,k} - v_{i,j-1,k}}{2\Delta\eta} + \frac{\partial\zeta}{\partial z}\frac{v_{i,j,k+1} - v_{i,j,k-1}}{2\Delta\zeta} \quad \ldots\ldots\ldots\ldots\ldots\ldots \textbf{(A. 19)}$$

$$\psi_{wx} = \frac{\partial\xi}{\partial x}\frac{w_{i+1,j,k} - w_{i-1,j,k}}{2\Delta\xi} + \frac{\partial\eta}{\partial x}\frac{w_{i,j+1,k} - w_{i,j-1,k}}{2\Delta\eta} + \frac{\partial\zeta}{\partial x}\frac{w_{i,j,k+1} - w_{i,j,k-1}}{2\Delta\zeta} \quad \ldots\ldots\ldots\ldots \textbf{(A. 20)}$$

$$\psi_{wy} = \frac{\partial\xi}{\partial y}\frac{w_{i+1,j,k} - w_{i-1,j,k}}{2\Delta\xi} + \frac{\partial\eta}{\partial y}\frac{w_{i,j+1,k} - w_{i,j-1,k}}{2\Delta\eta} + \frac{\partial\zeta}{\partial y}\frac{w_{i,j,k+1} - w_{i,j,k-1}}{2\Delta\zeta} \quad \ldots\ldots\ldots\ldots \textbf{(A. 21)}$$

$$\psi_{wz} = \frac{\partial\xi}{\partial z}\frac{w_{i+1,j,k} - w_{i-1,j,k}}{2\Delta\xi} + \frac{\partial\eta}{\partial z}\frac{w_{i,j+1,k} - w_{i,j-1,k}}{2\Delta\eta} + \frac{\partial\zeta}{\partial z}\frac{w_{i,j,k+1} - w_{i,j,k-1}}{2\Delta\zeta} \quad \ldots\ldots\ldots\ldots \textbf{(A. 22)}$$

The final equation for the second invariant of the rate of strain tensor is presented with the above terms.

$$\begin{aligned} II_d &= (\psi_{ux})^2 + (\psi_{vy})^2 + (\psi_{wz})^2 + \frac{1}{2}(\psi_{uy} + \psi_{vx})^2 + \\ &\qquad \frac{1}{2}(\psi_{uz} + \psi_{wx})^2 + \frac{1}{2}(\psi_{vz} + \psi_{wy}) \quad \ldots\ldots\ldots\ldots\ldots\ldots\ldots\ldots\ldots\ldots \textbf{(A. 23)} \end{aligned}$$

APPENDIX B

MODEL INPUT DATA AND RUNNING THE SIMULATOR

The input.dat data file accepts a range of fluid and treatment parameters to simulate an acid fracture treatment. Below is a list of the input data required by this file in the order it appears.

Table B.1–Sample data to be entered to "input.dat"

Newtonian fluid viscosity, cp	1
Filtrate viscosity, cp	1
Acid fluid density, kg/m^3	1070
Formation porosity, fraction	0.15
Total reservoir compressibility, 1/psi	0.00015
Reservoir fluid viscosity, cp	0.9
Filter cake wall-building leakoff coefficient, ft/$min^{0.5}$	0.005, 0.0
Acid concentration, % by weight	15
Effective diffusion, m^2/s	0.000000008
Limestone density, kg/m^3	2710
Dolomite density, kg/m^3	2870
Temperature, ˚F	100
Fraction to react on surface before leaking off, dimensionless	0.3
Pump rate to one half fracture during acid fluid injection, BPM	10

Injection time for acid fluid, minutes	20
Pore volumes to breakthrough for limestone, dimensionless	1.5
Pore volumes to breakthrough for dolomite, dimensionless	20
Name of mineralogy input file	mineralogy.dat
Name of permeability input file	permeability.dat
Name of geometry input file	geometry.dat
Power law fluid indicator, 0=Newtonian and 1=Power law	0
Power law fluid exponent, dimensionless	0.7
Power law consistency index, kg/m-s^{2-n}	0.1
Dimensionless horizontal correlation length	1.0
Dimensionless vertical correlation length	0.1
Dimensionless standard deviation of permeability	0.3
Young's modulus, 10^6 psi	4.5
Closure stress on fracture, psi	2000
Time of pumping pad, minutes	10
Efficiency of pad fluid, dimensionless	0.5
Flush volume, bbl	5.2

The parameters used to calculate the fluid leakoff are used indirectly, since the fluid efficiency is used to determine what portion of the influent flow leaks out of the fracture walls. These terms include the filtrate viscosity, total reservoir compressibility, reservoir fluid viscosity, and the wall-building leakoff coefficient (this can be zero to calculate the leakoff without its inclusion or it may be some actual number). The mineralogical parameters are used only if the mineralogy defined in the next input file, mineralogy.dat, includes that mineralogy. This next input file simply contains the number 0 to indicate dolomite, 1 to indicate limestone, and any other number to indicate a nonreactive layer.

Table B.2–Sample data to be entered to "mineralogy.dat"

Nonreactive layer	3
Dolomite layer	0
Limestone layer	1
Limestone layer	1
Dolomite layer	0
Limestone layer	1

The third input data file, permeability.dat, has the same number of layers as in the mineralogy.dat file and indicates the ratio of the permeability of the layers. The leakoff is calculated based on the input fluid efficiency, but the next input file is used to allocate portions of the leakoff to each layer.

Table B.3–Sample data to be entered to "permeability.dat"

Nonreactive layer, lower leakoff	0.5
Dolomite layer, moderate leakoff	1.0

Limestone layer, highest leakoff	2.0
Limestone layer, highest leakoff	2.0
Dolomite layer, moderate leakoff	1.0
Limestone layer, highest leakoff	2.0

The last input data file, geometry.dat, specifies the physical domain of the simulation. This file contains the fracture efficiency, the number of grid blocks in the *x*-direction, the number of grid blocks in the *z*-direction, the size of each (not necessarily the same in each direction but constant across the fracture height and length), and the fracture width arrays. There must be the same number of fracture width arrays in the vertical direction as layers specified in the mineralogy.dat and permeability.dat input files. Sample data for this input file is listed below.

Table B.4–Sample data to be entered to "geometry.dat"

Fracture efficiency	0.0
Number of grid blocks in *x*-direction	5
Number of grid blocks in *z*-direction	6
Size of grid block in *x*-direction, feet	20
Size of grid block in *z*-direction, feet	10

Fracture width arrays, inches:

0.080392	0.078210	0.067946	0.040032	0.000000
0.158875	0.153441	0.138664	0.099214	0.049226
0.235310	0.191121	0.152956	0.125392	0.066325

```
0.202094    0.192828    0.182764    0.148328    0.076744
0.104484    0.090212    0.071687    0.063251    0.023219
0.021342    0.020793    0.020154    0.000000    0.000000
```

The four files with model input data must be in the same folder as the source code. The source code may be executed one of two ways: use a compiler to create a .exe application file or use an integrated development environment (e.g., Microsoft Visual Studio) to run the code. The code runs fastest if it is saved in a folder on one of the computer's local drives. When the code runs, the command window displays the following output (Fig. C.1).

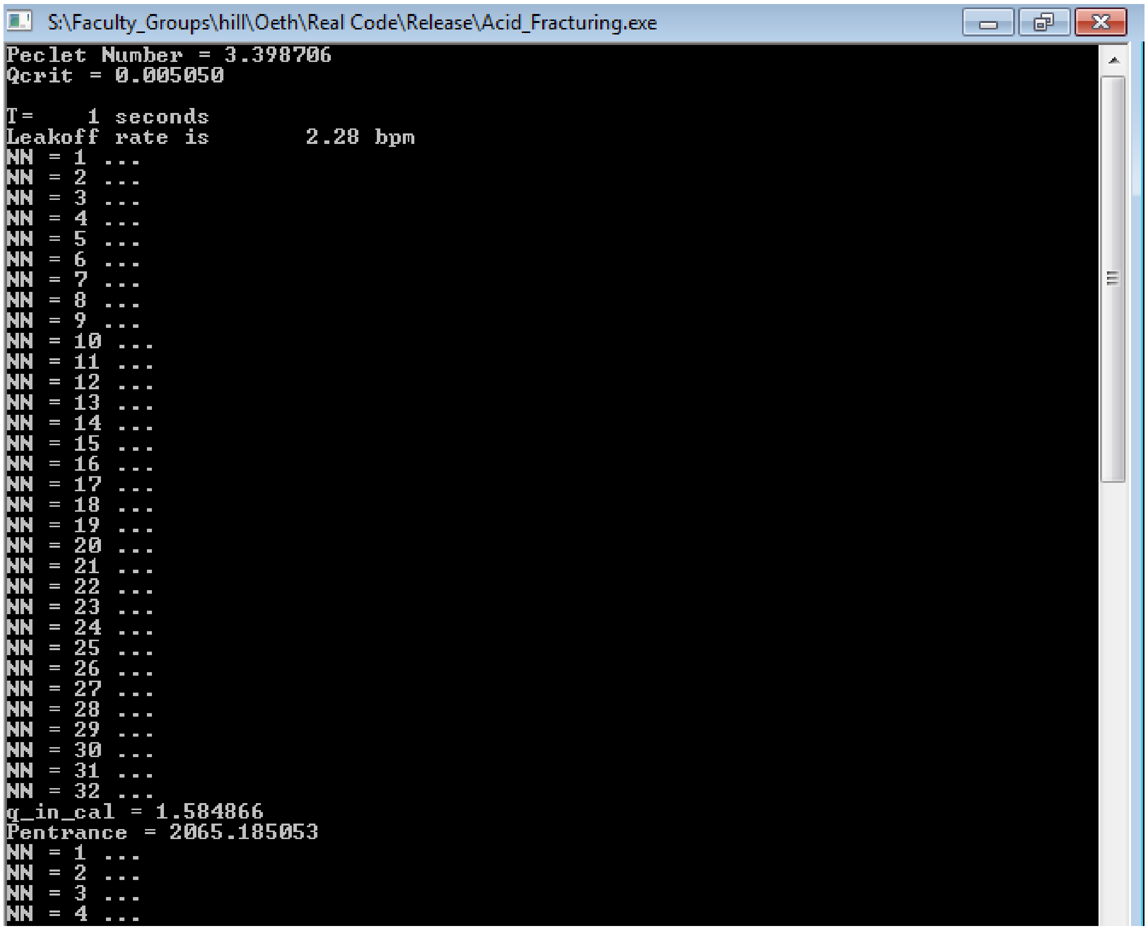

```
Peclet Number = 3.398706
Qcrit = 0.005050

T=     1 seconds
Leakoff rate is        2.28 bpm
NN = 1 ...
NN = 2 ...
NN = 3 ...
NN = 4 ...
NN = 5 ...
NN = 6 ...
NN = 7 ...
NN = 8 ...
NN = 9 ...
NN = 10 ...
NN = 11 ...
NN = 12 ...
NN = 13 ...
NN = 14 ...
NN = 15 ...
NN = 16 ...
NN = 17 ...
NN = 18 ...
NN = 19 ...
NN = 20 ...
NN = 21 ...
NN = 22 ...
NN = 23 ...
NN = 24 ...
NN = 25 ...
NN = 26 ...
NN = 27 ...
NN = 28 ...
NN = 29 ...
NN = 30 ...
NN = 31 ...
NN = 32 ...
q_in_cal = 1.584866
Pentrance = 2065.185053
NN = 1 ...
NN = 2 ...
NN = 3 ...
NN = 4 ...
```

Fig. C.1—Screenshot of command window running Acid_Fracturing.exe.

Most of the input data is read automatically from the input files, but some special conditions must be entered manually. The boundary condition for weak acids must be entered manually, since HCl is so commonly pumped for acid fracture treatments. The limited entrance condition meant to model perforation clusters affects how the inlet boundary condition, calculated entrance flow, and acid-etched width at the inlet are determined. The relaxation factor or maximum number of iterative steps to encourage convergence of the velocity and pressure fields may also need to be changed based on the complexity of the initial fracture geometry.

Output files are automatically generated during the simulation for every simulated minute. There are three types of output files. The result file contains the bulk of the calculated model output. This includes the three-dimensional velocity, apparent viscosity if a power law fluid is specified, pressure, acid concentration, and the calculated reaction coefficient for identification of layer geology. The contents of any result file may be readily viewed with Tecplot and the Tecplot Data Loader import format with 3D Cartesian plot type. The other two types of output include the acid-etched width and conductivity. There are two files for each of these output data. One file has the correct format to be read into Tecplot with the Tecplot Data Loader import format and 2D Cartesian plot type. The other file output is simply the acid-etched width or conductivity across the fracture, beginning at the top portion of the fracture at the wellbore (same format as the input initial width arrays in geometry.dat). These output files are generated for every minute of the simulated treatment and at the end of the total input treatment time (includes the flush volume). The two numbers after the file name indicate the time in minutes during which the output was captured.